

Electronic and Magnetic Structure of Epitaxial Nickel Cobaltite Ultrathin Films on $\text{MgAl}_2\text{O}_4(001)$

MASTERARBEIT

vorgelegt von

Florian Donder

im Rahmen der Prüfung für den Studiengang Master Physik
in der Arbeitsgruppe von Joachim Wollschläger
am Fachbereich Physik der Universität Osnabrück

Matrikelnummer: 965733

Erstprüfer: Prof. Dr. Joachim Wollschläger
Zweitprüfer: Dr. Karsten Küpper

Osnabrück, 10.10.2022

Contents

1	Introduction	1
2	Theoretical Basics	3
2.1	Crystal structure	3
2.1.1	Crystal lattices	3
2.1.2	Miller indices	4
2.1.3	Reciprocal lattice	4
2.1.4	Crystal surface	5
2.1.5	Epitaxial growth of thin films	6
2.1.6	Reactive molecular beam epitaxy	7
2.2	Low-energy electron diffraction	8
2.3	X-ray reflectometry	9
2.4	Magnetism	13
2.4.1	Basic effects	13
2.4.2	Origins of collective magnetism	16
2.4.3	Anisotropy and domains	19
2.4.4	Magnetisation curves	21
2.4.5	Superconducting quantum interference device magnetometry	24
2.5	Core-level spectroscopy	26
2.5.1	Photoexcitations in core-level spectroscopy	26
2.5.2	Principle of X-ray photoelectron spectroscopy	27
2.5.3	Quantitative analysis of XPS features	28
2.5.4	X-ray absorption spectroscopy	32
2.5.5	X-ray magnetic circular dichroism	35
2.5.6	Multiplet calculations	37
2.6	Transmission electron microscopy	41
3	Relevant Materials	45
3.1	Nickel(II)- and cobalt(II)-monoxide (NiO & CoO)	45
3.2	Magnesium aluminium oxide (MgAl_2O_4)	46
3.3	Nickel cobaltite (NiCo_2O_4)	47

4	Experimental Setup and Sample Preparation	49
4.1	Sample preparation in an ultra-high vacuum system	49
4.1.1	Plasma source	51
4.2	Low-energy electron diffraction setup	51
4.3	X-ray photoelectron spectrometer	52
4.4	X-ray reflectrometer	54
4.5	SQUID-setup	54
4.5.1	Data processing	56
4.6	XAS & XMCD	56
4.6.1	Processing of absorption data	57
4.7	TEM	58
5	Results and Discussion	59
5.1	LEED	59
5.2	XRR	60
5.3	XPS	62
5.3.1	2p spectra	63
5.3.2	3p spectra	66
5.3.3	Valence band spectra	69
5.4	Transmission electron microscopy	71
5.5	X-ray absorption	73
5.6	SQUID magnetometry	76
5.6.1	Temperature dependence	76
5.6.2	Field dependence	79
5.6.3	Discussion	84
6	Summary & Outlook	89
A	NiO reference fit	93
B	CoO reference fit	95
C	XAS magnetisation calculations	97
	Literature	99

1 | Introduction

Transition metal spinel oxides comprise a category of materials that exhibit a large variety in magnetic, electronic and optical properties, which vary depending on the cation composition and coordination in the materials. One such material is nickel cobaltite (NiCo_2O_4), an inverse transition metal oxide spinel generally described as a ferrimagnet with a transition temperature of over 400 K [1], with promising properties for use in a multitude of applications. Among these properties are an extraordinary electronic conductivity compared to other transition metal oxides [2], ferrimagnetism [3], a high electrochemical activity with rich redox reactions [4] and low cost due to easy availability. Due to these unique properties, nickel cobaltite has been extensively used in electrocatalysis [5], as well as in technological applications such as in supercapacitors [6] and photo-detectors. The electric and magnetic properties of nickel cobaltite are tunable by adjusting the cation composition [4], which makes it a promising candidate for use in spintronics devices such as spin-valves or magnetic tunnel junctions [3, 2, 7].

The cation composition of nickel cobaltite films sensitively depends on the manufacturing process used, as well as external parameters such as oxygen partial pressure, growth temperature, annealing temperature and time, and the potential inclusion of capping layers [2, 8]. In order to get a clear picture of the useful property range that nickel cobaltite can exhibit, it is thus necessary to compare the results of different manufacturing processes, especially since the viability of the processes in potential industry applications differs immensely. Many previous investigations of the NiCo_2O_4 cation composition used methods such as pulsed laser deposition [3, 9], thermal decomposition [8] and chemical spray pyrolysis [6].

However, few studies concentrate on nickel cobaltite films prepared using reactive molecular beam epitaxy (RMBE) (e.g. [2]), which is a method of preparing ultra-thin films of high crystalline quality and purity under ultra-high vacuum conditions [10]. For this reason, the focus of this work is the preparation and characterisation of NiCo_2O_4 films on MgAl_2O_4 using RMBE. Ideally, a full phase diagram relating the film structure to growth temperature and oxygen partial pressure under RMBE conditions could be produced, as has previously been reported using other methods [4]. To this end, a series of nickel cobaltite films, prepared at varying temperatures but otherwise similar conditions, is investigated in this work.

An array of measurement techniques was performed on the series of films, which is

used to characterise their crystal structure, as well as their cation coordinations and valencies using microscopy and X-ray spectroscopy techniques. The film composition apparent from these investigations is then related to the magnetic behaviour of the films measured using a superconducting quantum interference magnetometer.

In chapter 2, the theoretical background necessary to understand the the relevant measurement methods is presented. The structure and properties of the investigated materials are shown in chapter 3. Details on the experimental setups used in this work as well as the analysis of the experiment results follow in chapter 4. In chapter 5, the experimental results are presented and discussed. Finally, chapter 6 contains a summary of the results and an outlook for possible future investigations.

2 | Theoretical Basics

In this chapter, an overview of the theoretical background necessary to understand the experiments and discussion thereof presented in this work is given. General information about the structure of crystal systems is discussed first. Then, the theory behind Low-energy electron diffraction as well as X-ray reflectometry is introduced. The different kinds of magnetism and their origins as well as the theory behind measurements of magnetic moments using a quantum interference device are discussed in detail. In order to understand the cation composition analysis, the principles of X-ray photoelectron- and X-ray absorption spectroscopy are shown, including the quantitative interpretation using intensity yields and multiplet calculations. Finally, a short overview of the measurement principle of transmission electron microscopy is given.

2.1 Crystal structure

In this section, the structure of crystals is introduced. First, a general description of crystal lattices using translation vectors and miller indices is given. Then, the reciprocal lattice is introduced. The special case of a two dimensional lattice in crystal surfaces is described next, followed by an overview over the epitaxial growth process in thin films. The information in this chapter is compiled from [11, 12, 13, 14].

2.1.1 Crystal lattices

An ideal crystal is defined as an infinite, periodic arrangement of a basis in three dimensional space. The basis can consist of one or multiple atoms, which are placed identically relative to each point in the mathematically abstract lattice. The periodic structure of the lattice can be described in terms of a unit cell, which is defined by three linearly independent basis vectors \vec{a}_i , $i = 1, 2, 3$, as depicted in figure 2.1.

The crystal lattice can be constructed in its entirety by performing the translation operation given by a translation vector

$$\vec{T} = \sum_i n_i \vec{a}_i, n_i \in \mathbb{Z} \quad (2.1)$$

on the unit cell. Similarly, when starting from an arbitrary point \vec{r}_j in the lattice, an identical point can be reached by a translation

$$\vec{r} = \vec{r}_j + \vec{T}. \quad (2.2)$$

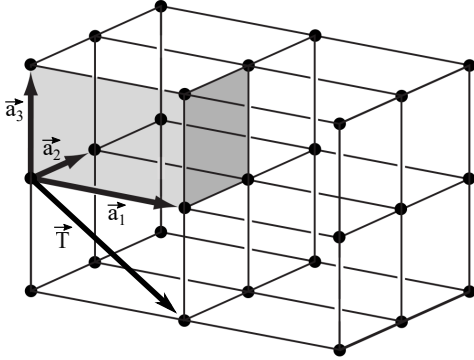


Figure 2.1: Space lattice of an ideal crystal. A possible set of basis vectors \vec{a}_i and the corresponding unit cell as well as a translation vector $\vec{T} = \vec{a}_1 - \vec{a}_3$ are shown. Adapted from [11].

If every identical point in the lattice can be reached by this operation, the basis vectors \vec{a}_i are called primitive. Correspondingly, the unit cell that is defined by primitive basis vectors is called a primitive unit cell. It has the smallest possible volume and contains only one lattice point. In general, there are multiple possible choices for the basis vectors and the unit cell of a given crystal structure.

The relative lengths of the basis vectors and the angles between them serve to classify a crystal lattice into one of seven possible lattice systems. Depending on their symmetry, the classification can be further specified, resulting in 14 possible Bravais lattices in three dimensional space.

2.1.2 Miller indices

Miller indices are used in order to specify directions and planes in the crystal. They describe the orientation of a plane group in relation to the lattice origin that is defined by treating the basis vectors \vec{a}_i as coordinate axes. The orientation of a crystal plane is in this way defined by the intersection of the plane with the axes in units of the lattice constants a_i . The reciprocals of the intersection coordinates are multiplied by a common factor so as to result in the smallest possible integer values for the set. The triplet of values hkl acquired in this way are the Miller indices. A negative index is indicated by a dash above the corresponding index (e.g. $h\bar{k}l$), whereas an intersection at infinity means the corresponding index is zero. There are multiple possible notations for a given set of Miller indices. They are shown in Table 2.1.

2.1.3 Reciprocal lattice

In order to investigate the crystal structure based on diffraction methods, it has proven useful to define a reciprocal lattice. The basis vectors of the reciprocal lattice are defined

Notation	Meaning
(hkl)	crystal plane
$\{hkl\}$	equivalent crystal plane group
$[hkl]$	crystal lattice direction
$\langle hkl \rangle$	equivalent lattice direction group

Table 2.1: Conventional notation of Miller-indices.

as

$$\vec{b}_1 = 2\pi \frac{\vec{a}_2 \times \vec{a}_3}{V_u}, \quad \vec{b}_2 = 2\pi \frac{\vec{a}_3 \times \vec{a}_1}{V_u}, \quad \vec{b}_3 = 2\pi \frac{\vec{a}_1 \times \vec{a}_2}{V_u}, \quad (2.3)$$

with $V_u = \vec{a}_1 \cdot \vec{a}_2 \times \vec{a}_3$ being the volume of the unit cell. Since every reciprocal basis vector is orthogonal to the area defined by the other two real basis vectors, it follows that the reciprocal lattice vector

$$\vec{G} = \sum_i n_i \vec{b}_i \quad (2.4)$$

is orthogonal to the plane group defined by the Miller indices (hkl) . The length of the lattice vector \vec{G} is related to the lattice plane distance d by

$$|\vec{G}| = \frac{2\pi}{d}. \quad (2.5)$$

2.1.4 Crystal surface

The structure of crystalline surfaces can be described similarly to the bulk of a crystal. Since the surface structure is periodic only in two dimensions, its lattice can be described by just two basis vectors. In two dimensions, the number of Bravais lattices is reduced to five.

Along the surface plane, the surface structure can differ from the structure of the bulk material due to superstructures that form through relaxations and reconstructions that are caused by missing binding partners of the surface atoms or by adsorbate atoms that bind to the surface atoms. These superstructures are described by a new unit cell with the basis vectors \vec{a}'_1 and \vec{a}'_2 and a corresponding translation operator \vec{T}' . The basis vectors of a superstructure are defined in relation to the basis vectors of the bulk material surface plane. Different notations exist to express this relation. If the angles between the basis vectors of the superstructure and the bulk structure are identical, the Wood notation [15] can be used, where

$$X(hkl) \left(\frac{|\vec{a}'_1|}{|\vec{a}_1|} \times \frac{|\vec{a}'_2|}{|\vec{a}_2|} \right) R\varphi \quad (2.6)$$

describes the surface basis vectors of material X parallel to the (hkl) plane and rotated by φ relative to the orientation of the bulk basis vectors. Additionally, the thus defined

surface unit cell can be denoted with p or c , indicating either a primitive unit cell or one that contains an additional lattice point in its center.

In cases where the Wood notation is not applicable, the relation between the basis vectors of the superstructure and those of the volume structure can be described in matrix form as

$$\begin{pmatrix} \vec{a}'_1 \\ \vec{a}'_2 \end{pmatrix} = \begin{pmatrix} m_{11} & m_{12} \\ m_{21} & m_{22} \end{pmatrix} \begin{pmatrix} \vec{a}_1 \\ \vec{a}_2 \end{pmatrix}, \quad m_{ij} \in \mathbb{R}. \quad (2.7)$$

A reciprocal lattice can be constructed for a given surface structure in a similar way to the three dimensional crystal structure. Since there is no periodicity along the surface plane normal, the reciprocal basis vectors are defined as

$$\vec{b}_1 = 2\pi \frac{\vec{a}_2 \times \vec{n}}{|\vec{a}_1 \times \vec{a}_2|} \quad \vec{b}_2 = 2\pi \frac{\vec{a}_1 \times \vec{n}}{|\vec{a}_1 \times \vec{a}_2|} \quad (2.8)$$

with \vec{n} being the normal vector of the surface plane. The reciprocal lattice vectors can take continuous values perpendicular to the surface plane. In diffraction experiments, this results in diffraction rods along the plane normal.

2.1.5 Epitaxial growth of thin films

Epitaxy refers to the deposition of crystalline layers on top of a crystalline substrate with a uniform orientation that is governed by the structure and orientation of the substrate.

There are three types of epitaxial growth patterns. If the interactions between the atoms of the surface layer are stronger than the interactions between the surface atoms and the substrate atoms, the surface layers grow in islands that extend both in height and width until a layer is closed. This growth pattern is called Volmer-Weber growth. In the opposite case, when the interactions between the surface layer atoms and the substrate atoms dominate, layers grow sequentially, with the growth of a new layer not starting before the previous layer is closed. This growth pattern is called Frank-van-der-Merwe growth. A combination of both types is possible and results in sequential growth of complete layers up to a specific thickness of the film, after which the film grows in islands. This growth type is called Stranski-Krastanov growth.

Depending on whether the material of the surface film and the substrate are the same, a distinction between heteroepitaxy and homoepitaxy can be made. When a film is deposited in the process of heteroepitaxy, its lattice constant is generally not identical to the substrate lattice constant. A measure of this difference is given by the lattice mismatch

$$\epsilon = \frac{a_f - a_s}{a_s} \quad (2.9)$$

with the lattice constants a_f of the film and a_s of the substrate. The lattice mismatch influences how the film is structured relative to the substrate. If the lattice mismatch

is small, the film takes on the periodic structure of the substrate in the surface plane, which leads to elastic strain. In order to minimize the energetic strain effect, the film is distorted perpendicularly to the surface, as seen in figure 2.2(a). This behaviour is known as pseudomorphic growth. At high lattice mismatches the elastic strain becomes too large to facilitate pseudomorphic growth. Instead the film grows with dislocations in direction of the surface plane at the interface between the substrate and the film (figure 2.2(b)). Additionally, misfit dislocations become energetically favourable at higher film thicknesses.

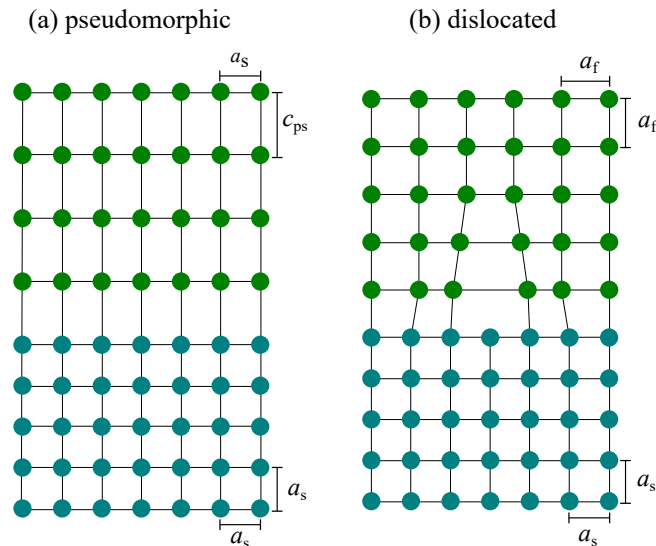


Figure 2.2: Heteroepitaxial growth modes: (a) pseudomorphic growth; (b) dislocated growth. Adapted from [12].

2.1.6 Reactive molecular beam epitaxy

Molecular beam epitaxy describes the deposition of crystalline thin films by means of the (combined) evaporation of elements onto a sample substrate. The term 'molecular beam' is used because the procedure is performed under high vacuum conditions, where the inelastic mean free paths of the evaporated atoms are larger than the paths to the substrate surface and the atoms consequently do not interact with each other on the way to the surface. The rate of adsorption can be influenced by controlling the substrate temperature.

The material is evaporated by accelerating electrons from a current carrying filament onto a solid target consisting of the material in question with an applied high voltage. The target is heated by the electrons and the target atoms subsequently start sublimating. The material atoms are focused onto the substrate surface with an aperture, while the cation current passing through it is measured in order to gauge the flow of atoms. This also enables the possibility of predicting the evaporated film thickness. The distinction between regular molecular beam epitaxy and reactive-MBE is the evaporation

under an atmosphere of oxygen or another reactive gas [16]. Under these conditions, the atoms of the evaporated materials react with the gas while adsorbing on the heated substrate surface.

2.2 Low-energy electron diffraction

Low-energy electron diffraction (LEED) is an experimental method that allows for the determination of surface crystal structures by visualising the reciprocal lattice on a fluorescent screen via the diffraction pattern of electrons that are accelerated onto the sample. Typical electron energies in LEED are in the range of 20 - 500 eV, which leads to electron de-Broglie wavelengths

$$\lambda = \frac{h}{2m_e E_{\text{kin}}} \quad (2.10)$$

in the range of 0.5 - 3 Å [13]. In equation 2.10, h refers to the Planck constant, m_e to the electron mass and E_{kin} to its kinetic energy. This makes electrons in this energy range suitable for diffraction by atoms in a solid because their wavelength is in the same order of magnitude as the inter-atomic distances. The surface sensitivity of LEED is given by the inelastic mean free paths (IMFPs) of electrons, i.e. the average distance an electron will travel in the material without an inelastic scattering event occurring. IMFPs can be calculated by use of the TPP-2M equation [17] and differ only slightly between different materials, resulting in a so-called universal curve [18]. Most elastic interactions of electrons will occur in the first few top layers of the surface, which means that they probe the nearly two-dimensional surface structure.

In order for electrons to be diffracted by the surface and for the reflexes to be visible due to constructive interference, two conditions must hold in order to satisfy the conservation of moment and energy:

$$\vec{q}_{\parallel} = \vec{k}_{f,\parallel} - \vec{k}_{i,\parallel} = \vec{G}_{hk}, \quad (2.11)$$

which is also known as the (two-dimensional) Laue-condition, where \vec{q}_{\parallel} is the diffraction vector component parallel to the surface, $\vec{k}_{f,\parallel}$ and $\vec{k}_{i,\parallel}$ are the parallel components of the incident and diffracted electron wave vectors, and \vec{G}_{hk} is a reciprocal lattice vector of the 2D-surface lattice, as well as

$$|\vec{k}_i| = |\vec{k}_f|. \quad (2.12)$$

Both conditions can be visualised using the Ewald construction (see figure 2.3). The incidence wave vector \vec{k}_i is drawn into the reciprocal lattice, so that it terminates at a lattice point or at a continuous lattice rod in the case of a two-dimensional surface lattice. The incidence angle in conventional LEED is 90° relative to the surface plane. A sphere with radius $|\vec{k}_i|$ can be constructed around the origin of \vec{k}_i , called Ewald-sphere. The intersections of the sphere surface with lattice rods indicate valid

diffraction vectors. The vectors \vec{k}_f constructed in this manner satisfy the equations 2.11 and 2.12 and the resulting image on the screen directly pictures the cross-sections of the diffraction rods [13]. An increase in electron energy scales the Ewald sphere up and in turn results in lower diffraction angles. This leads to the diffraction spots moving closer to the (00)-reflex.

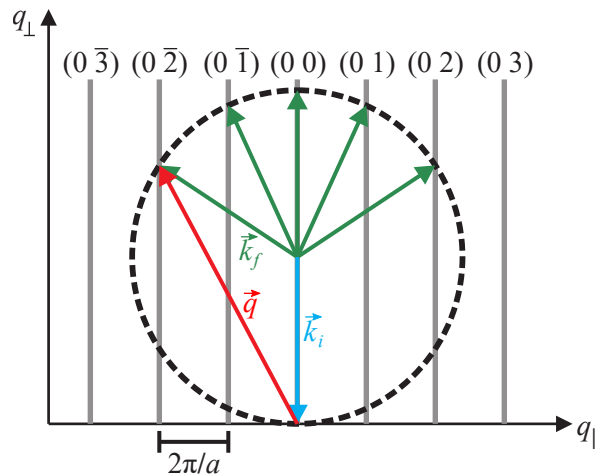


Figure 2.3: Ewald construction cross-section for diffraction at a two-dimensional lattice, with the x axis parallel to one of the basis vectors of the lattice plane. The incoming wave vector \vec{k}_i at normal incidence is depicted, along with the resulting backscattered wave vectors \vec{k}_f . The magnitude of both vectors defines the radius of the sphere. Diffraction spots occur where the sphere and the lattice rods intersect. The parallel part of \vec{q} can be expressed in multiples of $\frac{2\pi}{a}$ and as such in terms of reciprocal lattice vectors \vec{G}_{hk} . Adapted from [19].

The structure and symmetry of the diffraction spots of a given sample provide information about the two-dimensional surface crystal lattice structure. The intensity and width of the reflexes makes it possible to determine the crystalline quality of the surface under investigation, and under certain conditions the atomic arrangement in the unit cell. Structural point defects and impurities result in a higher background intensity and a broadening of reflex spots characteristic of the type of defect. In amorphous samples, this results in no discrete spots being visible at all [12]. The minimal spot size is determined by instrumental limitations and the coherence length of the electron beam. When investigating the arrangement of atoms or type of defects in the sample surface via intensity profile fits, it is often necessary to include dynamic scattering effects in the diffraction model as well as instrumental effects on the spot size or the coherence length. Since this work mostly uses LEED as a qualitative means of determining the crystal structure, these effects, as well as details on the effects of reconstructions, terraces and defect structures will not be considered in detail. Instead, refer to [12] and [13].

2.3 X-ray reflectometry

X-ray reflectometry (XRR) is a non-destructive method for determining the thickness of thin films and the roughness of thin film interfaces. It utilises the fact that X-rays are partly reflected at interfaces of materials with different optical constants and that beams reflected from different interfaces can interfere with each other. The general information in this section was compiled from [20, 21, 22].

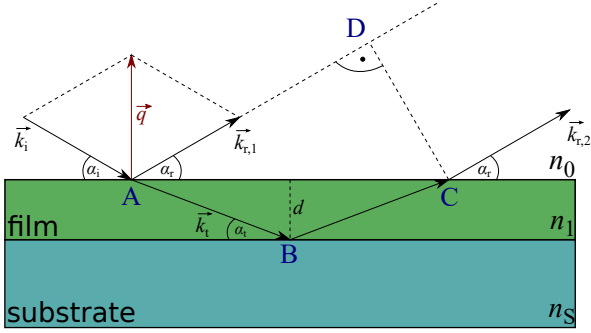


Figure 2.4: Principle of XRR for a system containing a film of thickness d and a substrate. The X-ray beam with wave vector \vec{k}_i illuminates the film at an angle α_i and is partly reflected into $\vec{k}_{r,1}$ and partly transmitted. The same process at the film-substrate interface produces a second reflected beam $\vec{k}_{r,2}$ that interferes with the reflected beam from the vacuum-film interface. This interference is characteristic of the multilayer system under investigation.

The principle of XRR is depicted in figure 2.4. Samples are modelled as layered slabs with homogeneous electron density profiles and refractive indices along their thicknesses d_j . An incidental wave \vec{k}_i arriving at the film surface is partially reflected into $\vec{k}_{r,1}$ and partially transmitted into \vec{k}_t . The angle of incidence is given relative to the surface plane and is equal to the reflection angle, i.e. $\alpha_i = \alpha_r$, which also means that the scattering vector \vec{q} with

$$|\vec{q}| = q_z = 2k \sin(\alpha_i) = \frac{4\pi}{\lambda} \sin(\alpha_i) \quad (2.13)$$

is parallel to the interface normal. In XRR, the wavelength is kept constant, whereas $\alpha_i = \alpha_r$ is varied in the region $\alpha_i < 5^\circ$ while measuring the reflected intensity from the sample. The reflectivity of the material is dependent on the index of refraction

$$n = 1 - \delta + i\beta, \quad (2.14)$$

where δ and β are constants of dispersion and absorption, respectively. Equation 2.14 holds for photon energies far from the film material's absorption edges. Typical material values for δ in the case of X-rays are in the range of 10^{-5} to 10^{-6} , while β is a few orders of magnitude lower. The corresponding refractive index has a real part slightly below one. This results in total reflection at the interface between the sample and vacuum below a critical angle α_c , which, according to Snell's law, can be approximated as $\alpha_c \approx \sqrt{2\delta}$.

At angles below α_c , the reflected intensity increases nearly linearly with q . This effect is called a footprint and results from the incident beam only irradiating parts of the finite sample until an angle of α_{fp} is reached, at which point the film surface along the beam direction is completely illuminated. For a rectangular beam with height b and a sample length l , the angle is $\alpha_{fp} = \arcsin(b/l)$. Above α_c , the reflected intensity of a single layer follows a q^{-4} dependence. For a film on a substrate, the transmitted wave is itself reflected at the interface between the film and the substrate into $\vec{k}_{r,2}$. $\vec{k}_{r,1}$ and $\vec{k}_{r,2}$ are parallel, and subsequently interfere due to the optical path difference (compare figure 2.4)

$$\Delta s = n_1 \cdot (\overline{AB} + \overline{BC}) - n_0 \cdot \overline{AD}. \quad (2.15)$$

Depending on α_i , the waves interfere constructively or destructively, resulting in oscillations in the resulting reflected intensity that are superimposed onto the q^{-4} dependence. These oscillations are known as Kiessig fringes. In the simple case of a single film on a substrate, the difference in scattering vectors between two oscillation peaks can be used to approximate the film thickness.

In the general case, the influence of multiple interfaces has to be taken into account, which result in superimposed oscillations of different periodicities that complicate the determination of the layer thickness. One method of calculating the reflectivity of multiple films and their oscillations is the transfer-matrix method developed by Abéles [23]. It is based on the superposition of the upwards and downwards moving electromagnetic X-ray waves in the medium. The electric field E_j of the superimposing waves at the interfaces of the layers j and $j + 1$ at an depth z_j from the vacuum interface is given by a solution of the Helmholtz equation:

$$E_j = [A_j^+ e^{ik_{j,z}z_j} + A_j^- e^{-ik_{j,z}z_j}] \cdot e^{-i(\omega t - k_{j,y}y)}, \quad (2.16)$$

where A_j is the amplitude of the electric field in medium j , $k_{j,z}$ and $k_{j,y}$ are the z and y components of the wave vector in layer j and ω is the pulsation of the field with time. The superscript in A_j^+ and A_j^- denotes the direction of the wave propagation. The y component of k_j is conserved at each interface due to Snell's law and so the magnitude of the spatial part of the electric field in both z -directions can be simplified to

$$u_j^\pm(z_j) = A_j^\pm e^{\pm ik_{j,z}z_j}. \quad (2.17)$$

Adding the boundary condition that the tangential part of the electric field is continuous and that its first derivative is conserved, it follows that

$$\begin{pmatrix} u_0^+(z_1) \\ u_0^-(z_1) \end{pmatrix} = \mathbf{M} \begin{pmatrix} u_S^+(z_S) \\ u_S^-(z_S) \end{pmatrix} = \begin{pmatrix} M_{11} & M_{12} \\ M_{21} & M_{22} \end{pmatrix} \begin{pmatrix} u_S^+(z_S) \\ u_S^-(z_S) \end{pmatrix}, \quad (2.18)$$

where z_1 and z_S refer to the interfaces to vacuum and to the substrate, respectively. Matrix \mathbf{M} is a product

$$\mathbf{M} = R_{0,1} T_1 R_{1,2} \dots T_N R_{N,S}, \quad (2.19)$$

with the refraction and translation matrixes R and T

$$R_{j,j+1} = \begin{pmatrix} p_{j,j+1} & m_{j,j+1} \\ m_{j,j+1} & p_{j,j+1} \end{pmatrix} \quad (2.20)$$

$$T_j = \begin{pmatrix} e^{-ik_{j,z}d_j} & 0 \\ 0 & e^{ik_{j,z}d_j} \end{pmatrix} \quad (2.21)$$

that define the refraction at the interface between layers j and $j + 1$ and the translation through the layer j with a thickness of d_j , respectively. In equation 2.20, $m_{j,j+1}$ and

$p_{j,j+1}$ are given by

$$\begin{aligned} p_{j,j+1} &= \frac{k_{j,z} + k_{j+1,z}}{2k_{j,z}} \\ m_{j,j+1} &= \frac{k_{j,z} - k_{j+1,z}}{2k_{j,z}}, \end{aligned} \quad (2.22)$$

and are related to the Fresnel coefficient of the interface as $r_{j,j+1} = \frac{m_{j,j+1}}{p_{j,j+1}}$. Note that these Fresnel coefficients are abstract parameters in the context of the multilayer structure, as they neglect backscattering from interfaces further below and thus do not represent the total reflection coefficient at the respective interface.

The total reflection coefficient in amplitude of the multilayer structure - including backscattering effects - is defined as the ratio of reflected and incident electric field at the surface and can be calculated as

$$r = \frac{u_0^+(z_1)}{u_0^-(z_1)} = \frac{M_{11}u_S^+(z_S) + M_{12}u_S^-(z_S)}{M_{21}u_S^+(z_S) + M_{22}u_S^-(z_S)}. \quad (2.23)$$

It is usually reasonable to assume that the substrate has an infinite thickness because the X-rays only penetrate a few μm into the sample. This means that there is no wave returning from the substrate, i.e. $u_S^+(z_S) = 0$. Equation 2.23 then turns into

$$r = \frac{M_{12}}{M_{22}}. \quad (2.24)$$

In the transfer-matrix method, squaring equation 2.24 results in the intensity values that are compared to the experiment for fitting purposes.

The parameters defined in equation 2.22 hold for s-polarised X-rays. In the case of plane (p) polarisation, the coefficients are modified:

$$\begin{aligned} p_{j,j+1}^{(p)} &= \frac{n_{j+1}^2 k_{j,z} + n_j^2 k_{j+1,z}}{2n_{j+1}^2 k_{j,z}} \\ m_{j,j+1}^{(p)} &= \frac{n_{j+1}^2 k_{j,z} - n_j^2 k_{j+1,z}}{2n_{j+1}^2 k_{j,z}}, \end{aligned} \quad (2.25)$$

although this distinction is only relevant in the soft X-ray regime, where the refractive indices differ more substantially from unity.

The z components of the wave vectors are related to the refractive index and incidence angle by $k_{j,z} = -n_j k_0 \sin(\alpha_{t,j}) = -k_0 \sqrt{n_j^2 - n_0^2 \cos^2(a_i)}$, where k_0 is the magnitude of the incidence wave vector. If the experiment is performed in air instead of in a vacuum, $n_0 \approx 1$ can still be assumed to hold in the X-ray range [24].

The above discussion holds only for perfectly sharp interfaces, ignoring effects of structural defects, which result in a continuous change of the electron density and refractive index along the interface, modeled by a mean vertical coordinate and a roughness parameter given by the standard deviation σ_j . For $\sigma \ll d$, a good approximation is

achieved by modelling the vertical interface fluctuations by an error function, resulting in an additional roughness parameter in the Fresnel coefficient:

$$r'_{j,j+1} = r_{j,j+1} e^{-2k_{j,z}k_{j+1,z}\sigma_j^2}. \quad (2.26)$$

The exponential term is known as the Névot-Croce factor [25]. Larger values of σ generally result in a stronger reflectivity decay or an additional damping of the Kiessig-fringe intensities with q . For very rough films, the roughness profile has to be modelled by a series of thin and flat layers.

From equations 2.24 and 2.26 it is possible to approximate measured reflectivity data with a simulated curve, where the layer thicknesses and interfacial roughnesses are typically the free parameters, while the indices of refraction are given by literature values.

2.4 Magnetism

In the following chapter, an overview over the essential effects and parameters required to describe and interpret the magnetic response of materials is given. Additionally, the principle of SQUID measurements is described. The majority of this chapter is compiled from [12, 26, 27, 28, 29].

2.4.1 Basic effects

Materials inside an external magnetic field \vec{H} exhibit a macroscopic magnetisation \vec{M} that can either weaken or strengthen the external field inside the material. The material magnetisation is a volume effect and given by the averaged magnetic moments \vec{m} of the atoms in the material volume:

$$\vec{M} = \frac{1}{V} \sum_V \vec{m} \quad (2.27)$$

The atomic magnetic moments either exist intrinsically as orbital and spin moments of the electrons within the atoms, which can be aligned by an external field, or they can be induced by external fields in materials without intrinsic magnetic moments.

For weak external fields, the relationship between magnetisation and field is

$$\vec{M} = \chi \vec{H}, \quad (2.28)$$

where χ is called the magnetic susceptibility and depends on material properties as well as the temperature. In the general case, χ is a second-order tensor because of anisotropies of the material.

When magnetic materials are investigated, the magnetic flux density is often of relevance. It is defined as

$$\vec{B} = \mu\mu_0\vec{H}, \quad (2.29)$$

where μ_0 is the vacuum permeability with the value $\mu_0 = 4\pi \times 10^{-7} \text{ Vs/Am}$ and μ is the relative permeability of the material, which can also be written as

$$\mu = 1 + \chi. \quad (2.30)$$

Combining equations 2.29 and 2.30 relates the magnetic flux \vec{B} to the magnetisation \vec{M} :

$$\vec{B} = \mu_0(\vec{H} + \vec{M}). \quad (2.31)$$

Materials can be classified according to the presence and type of long-range magnetic ordering and depending on the magnitude of individual atomic moments. The different types of magnetic long-range ordering are shown schematically in figure 2.5. In the following paragraphs, the individual types of magnetism are explained.

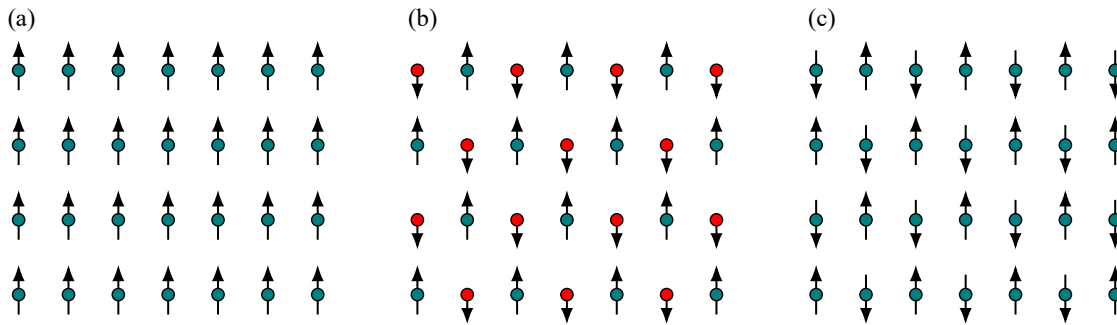


Figure 2.5: Illustration of the magnetic ordering in (a) ferromagnets, (b) antiferromagnets and (c) ferrimagnets.

Ferromagnetism

Ferromagnetic materials exhibit magnetic ordering of intrinsic atomic moments in a preferred direction, even without the presence of an external field. The presence of a sufficiently large external field can rearrange the moments into the field direction, meaning that $\chi > 0$. Out of all types of magnetism, ferromagnetism is characterised by the largest susceptibilities $|\chi| \gg 1$. An important characteristic of a ferromagnetic material is its Curie temperature T_C . It marks the temperature at which the magnetic ordering inside the material is disrupted as thermal fluctuations dominate the ordering interaction between individual moments. In temperature plots, a substantial drop in magnetisation is characteristic of the region just below T_C . Above T_C , ferromagnets behave like paramagnets. For temperature ranges $T \gg T_C$, the Curie-Weiss-law

$$\chi = \frac{T}{(C - T_C)\gamma} \quad (2.32)$$

predicts the susceptibility, where $\gamma \approx 1 - 1.5$ is a material constant that is related to the exchange interaction described in more detail in section 2.4.2. In equation 2.32, C is known as the Curie-constant. A large T_C -value implies strong ferromagnetic ordering.

Ferrimagnetism

Ferrimagnetism occurs when a material contains two sublattices, which in themselves show ferromagnetic ordering of different strengths and with different magnetisation values, but which are also aligned in opposition to each other. As a result, ferrimagnets - like ferromagnets - can show a magnetisation without an applied external field. The susceptibility of a ferrimagnet at high temperatures is reasonably described by a curve similar to equation 2.32, although additional terms describing abstract molecular fields of both sublattices have to be considered close to the critical temperature T_C [28].

Antiferromagnetism

Antiferromagnetism is in principle similar to ferrimagnetism, insofar that two sublattices with oppositely aligned magnetisations exist in the material. In antiferromagnetic materials, the magnetisation in both sublattices has the same magnitude, which results in the total magnetisation being cancelled out. The susceptibility of antiferromagnetic materials usually takes values

$$0 < |\chi| < 100. \quad (2.33)$$

Since antiferromagnetism results from the interaction of two ferromagnetic sublattices, antiferromagnetic materials behave similarly to ferromagnetic materials at high temperatures $T \gg T_N$, where the susceptibility can be described by

$$\chi = \frac{C}{T + \Theta_N}. \quad (2.34)$$

T_N and Θ_N are known as antiferromagnetic and paramagnetic Néel temperatures, respectively. They can be expressed as

$$T_N = \frac{C}{2}(\gamma_B - \gamma_A) \quad (2.35)$$

$$\Theta_N = \frac{C}{2}(\gamma_B + \gamma_A), \quad (2.36)$$

where both sublattices have the same Curie-constant C , and γ_B and γ_A are parameters related to the (abstract) molecular fields inside the sublattices. Below T_N , the susceptibility of antiferromagnets depends on the orientation of the spontaneous magnetisation of the sublattices relative to the external field. The perpendicular susceptibility is constant below T_N , whereas the parallel part tends to zero at 0 K. This, paired with the behaviour above T_N , leads to the susceptibility of antiferromagnets usually exhibiting a maximum at T_N . Additionally, an anomaly in the specific heat capacity is usually visible close to the Néel temperature. In general, the Néel temperatures of antiferromagnets are lower than the Curie temperatures of ferromagnets since the interactions between neighbouring moments are stronger in ferromagnets.

Paramagnetism

Paramagnetic materials contain intrinsic permanent magnetic moments, which result from uncompensated electronic spin and orbital moments. These moments are not aligned without an external field, but rather oriented randomly due to the lack of ordering interaction. This means that the magnetisation is $\vec{M} = \vec{0}$, unless an external field is applied. If an external field is introduced, the moments start to align in direction of the field, because the atomic states with moments parallel to the field are at lower energy. This alignment increases the magnetic flux density inside the material. The extent to which the moments align depends on the strength of thermal fluctuations and the potential energy of the magnetic moments in the field. The susceptibility of a paramagnet is positive and given by

$$\chi = \mu_0 \frac{M}{B} = \frac{\mu_0 N m^2}{3k_b T}, \quad (2.37)$$

in which N magnetic dipoles each contribute the magnetic moment m and where $k_b = 1.381 \times 10^{-23}$ J/K is the Boltzmann-constant. Multiple effects can contribute to paramagnetic behaviour in materials, the strongest of which is the Langevin-paramagnetism described by equation 2.37, which results from partially filled shells in the ground state in materials with fully localised electrons. Additional contributions, namely Pauli- and Van Vleck-paramagnetism, are much weaker in effect and can potentially be compensated for by diamagnetic effects.

Diamagnetism

Atoms in diamagnetic materials have no intrinsic magnetic moment that could be aligned by a field. When an external field is applied, however, magnetic dipoles are induced in the material. According to Lenz's law, the induced moments are aligned antiparallel to the external field. This means that the resulting field inside the material is smaller than the externally applied field and that the susceptibility of the material is negative. Since the moments are induced by the external field and not intrinsic, every material exhibits diamagnetic properties. However, the effect is negligible compared to the other forms of magnetism. As with paramagnetism, there are multiple diamagnetic contributions, namely the Langevin-diamagnetism from localised electrons, as well as the Landau-diamagnetism induced by delocalised electrons in metals. Diamagnetic effects are generally thought to be nearly independent of temperature, although weak linear temperature dependencies are known to exist in some materials [30].

2.4.2 Origins of collective magnetism

Magnetic order as it is seen in (anti-)ferromagnets and ferrimagnets is also known as collective magnetism. It was first described via the molecular field theory and the Stoner criterion in the case of metals, where a strong, internal field inside the material is responsible for the large magnetisations and preferred orientations of ferromagnets. Such a field does not exist, but it acts as an approximation of the effects known as

exchange interactions. They arise from the combined effects of the Pauli principle and the Coulomb repulsion of electrons. The Pauli principle prohibits two electrons from existing in the same quantum state. Since electrons are indistinguishable, this results in the requirement that the total wave function of a system of two localised electrons is antisymmetric, i.e.

$$\Psi(\mathbf{x}_1, \mathbf{x}_2) = -\Psi(\mathbf{x}_2, \mathbf{x}_1), \quad (2.38)$$

with $x_i = (\mathbf{r}_i, s_i)$, where \mathbf{r}_i and s_i denote positions and spins of electron i , and where the total wave functions $\Psi = \phi(\mathbf{r}_1, \mathbf{r}_2)\chi(s_1, s_2)$ can be written as products of space and spin functions ϕ and χ . When one of these two functions is symmetric, the other has to be antisymmetric and vice versa.

When the Coulomb repulsion is applied to Ψ , the state in which the electron spins are parallel becomes energetically favoured, because it allows the electrons to be farther apart spatially due to the antisymmetric spatial wave function. This indirect interaction between the spins due to Coulomb and Pauli effects can be modelled by a direct interaction between the spins and generalised to many-electron spins of atoms. The Heisenberg model [31] gives the Hamiltonian for the spin-spin coupling between atom pairs ij as

$$\mathcal{H} = -2 \sum_{i>j} J_{ij} \mathbf{S}_i \cdot \mathbf{S}_j, \quad (2.39)$$

where $\mathbf{S}_{i,j}$ are the dimensionless many-electron spin operators of the two atoms and J_{ij} is the exchange integral, which describes the type and strength of the exchange interaction. It can be positive or negative, corresponding to ferromagnetic or antiferromagnetic behaviour, and its value depends on the overlap of the atomic electron wave functions. The sum reduces to a sum over a single constant J if only nearest-neighbour interactions are considered. In cases where the spin is not a good quantum number, \mathbf{S} must be projected onto the generalised spin \mathbf{J} , if the Heisenberg model is to be used.

The exchange interaction can be described another way, using Slater-Condon integrals. Using this description, applying the Coulomb repulsion operator to the many-electron wave function of an atom yields [26]

$$\langle \Psi | \frac{e^2}{r_{12}} | \Psi \rangle = F + G, \quad (2.40)$$

where F and G known as the Slater-Condon integrals or Slater parameters. In this view, F is a Coulomb term that describes the classical Coulomb repulsion between the electrons, while G is an exchange term that corresponds to the exchange transition probability of the two indistinguishable electron positions. This exchange term is influenced by the overlap of the involved orbitals, which depends on the spin orientation of the electrons. In this way, the exchange term indirectly couples the electron spins in the atom. The exchange interaction favours spin alignments that maximise the delocalisation of electrons, which can result in a type of magnetic order being favourable energetically when equation 2.40 is generalised to inter-atomic interaction.

Exchange interactions

The nature of the exchange interaction described by the J or G -terms varies depending on material composition and geometry. In metals, direct exchange mechanisms can couple partly localised atom orbitals in a tight-binding approach. Other mechanisms couple delocalised electrons with each other and with localised core electrons. In transition metal oxides like NiCo_2O_4 , super exchange and double exchange are more relevant mechanisms.

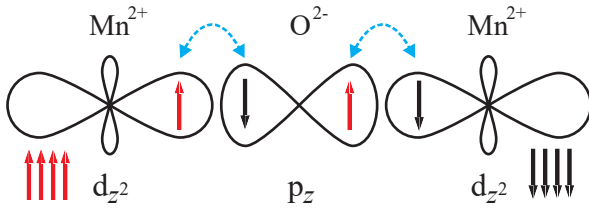


Figure 2.6: Super exchange interaction between two Mn^{2+} cations in MnO , mediated by O^{2-} . The exchange interaction between the electrons in the $\text{O } 2p_z$ and $\text{Mn } 3d_{z^2}$ orbitals couples the cations indirectly, resulting in an antiparallel spin alignment of the cations and consequently an antiferromagnetic ordering inside the material. Adapted from [19, 27].

Localised electron orbitals in transition metal oxides experience little direct overlap with neighbouring atoms, but the exchange interaction can be mediated via hybridisation with ligands - usually with the $2p$ orbitals of O^{2-} ions. This indirect interaction between identical metal cations is called super exchange.

Figure 2.6 depicts the example case of super exchange between Mn^{2+} cations mediated by O^{2-} anions in MnO . The $3d$ shells of the Mn^{2+} ions are half-filled with electrons of the same spin due to Hund's first rule and they overlap with the $\text{O } 2p$ orbitals, resulting in exchange interaction between them. The exchange is maximised if the $\text{O } 2p$ electrons can be delocalised over both adjacent Mn^{2+} cations. As discussed before, the Pauli exclusion results in the anti-parallel spin alignment of the interacting $\text{O } 2p$ and $\text{Mn } 3d$ electrons being favourable in order to maximise the exchange interaction. This, in turn, leads to an anti-parallel spin alignment of neighbouring cations and thus to antiferromagnetic coupling.

The nature and strength of the super exchange interaction depends strongly on the geometry of the atom bonds. The empirical Goodenough-Kanamori rules [32] can be used to predict the nature of exchange interactions in transition metal oxides:

1. Singly occupied $3d$ orbitals with large overlap, as found in materials with 120° - 180° bonds, interact strongly antiferromagnetically.
2. If the overlap integral between singly occupied $3d$ orbitals is zero, as with 90° metal-oxide-metal arrangements, the super exchange interaction is weakly ferromagnetic.
3. Singly occupied $3d$ orbitals that overlap with empty or doubly occupied orbitals of the same type exhibit a weak ferromagnetic exchange interaction.

Double exchange interactions are similar to super exchange interactions, with different

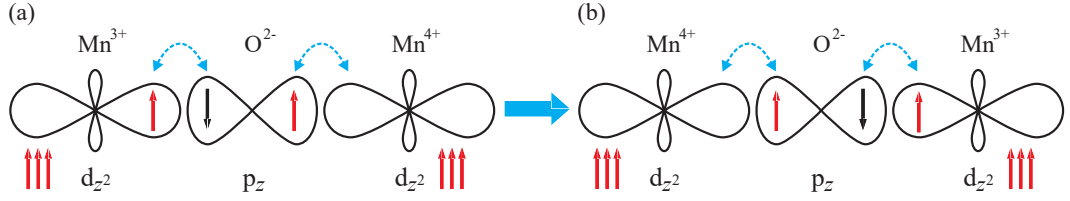


Figure 2.7: Double exchange interaction between Mn^{3+} and Mn^{4+} cations, mediated by O^{2-} . An electron can be delocalised between the two cations, but only if the spins of both cations are aligned parallel to each other. Both configurations (a) and (b) are degenerate, resulting in effective $\text{Mn}^{3.5+}$ cations. Adapted from [19].

valencies in the involved cations, as depicted for the example of Mn^{3+} and Mn^{4+} in figure 2.7. An electron from the Mn^{3+} cation can effectively be delocalised across the Mn^{4+} cation, but only if both cations are aligned parallel to each other with respect to their spins. The two possible configurations, with the electron localised at either atom, are degenerate, meaning that the cations are effectively identical $\text{Mn}^{3.5+}$ ions. The exchange is mediated by hybridisation between the Mn 3d and O 2p orbitals, similar to super exchange interaction. Double exchange is always ferromagnetic in nature because an anti-parallel alignment of the cations would prohibit electron transfer between the cations due to violation of Hund's rules.

2.4.3 Anisotropy and domains

Ferrimagnets and (anti-)ferromagnets below the Curie/Néel temperature are characterised by interactions of nearby spins. If this exchange interaction was the only relevant effect, all effective magnetic moments in a ferro(i)magnet would be aligned parallel to each other. Experiments show that this is not the case and that magnetisations in these materials are usually smaller than expected when only considering exchange interactions. An explanation for this behaviour can be found in the formation of magnetic domains inside materials that exhibit collective magnetism. The alignment of the moments inside a domain is largely determined by exchange interaction, while both the size and the orientation of the domains relative to each other are variable. In ferro- and ferrimagnets, the moments of the individual domains can compensate each other when not aligned in parallel. Only at high fields do all domains align, which results in the saturation magnetization of the material.

In a material exhibiting collective magnetism, domains are formed depending on multiple competing energy factors that contribute to the total free energy

$$F_{\text{tot}} = \int e_{\text{shape}} + e_{\text{ani}} + e_{\text{Zeeman}} + e_{\text{wall}} dV, \quad (2.41)$$

with the energy e_{shape} due to shape anisotropy, also known as magnetostatic self-energy, the magnetocrystalline anisotropy energy e_{ani} , the Zeeman energy $e_{\text{Zeeman}} = -\vec{H} \cdot \vec{M}$ and the energy e_{wall} needed to form domain walls. Other contributions, e.g. due to

strain and magnetostriction are usually negligible. The structure of the domains results from the minimisation of equation 2.41.

The Zeeman energy is caused by the interaction of the magnetic material with magnetisation \vec{M} with an externally applied magnetic field \vec{H} . It is minimised when \vec{M} and \vec{H} are aligned parallel to each other.

Magnetocrystalline anisotropy is an effect that results from the fixed crystal structure, which stabilises specific orbital alignments and from spin-orbit coupling, which couples the spin magnetic moments to these alignments. The resulting preferred directions of magnetisation are called easy axes. The magnetocrystalline anisotropy energy is minimised when the magnetisation is aligned with an easy axis.

Shape anisotropy is an effect that depends on the macroscopic geometric shape of the sample, which can lead to preferred magnetisation directions similar to magnetocrystalline anisotropy. Shape anisotropy results from uncompensated magnetic moments at the surface of the material. These induce a field

$$\vec{H}_d = -\mathcal{N}\vec{M} \quad (2.42)$$

inside the material, which is oppositely aligned to \vec{M} . \vec{H}_d is called the demagnetising field. \mathcal{N} is the demagnetisation tensor and characterises the direction and strength of anisotropy due to the sample shape. The energy term e_{shape} in equation 2.41 is related to the demagnetisation tensor by

$$e_{\text{shape}} = -\frac{\mu_0}{2} \int_V \vec{H}_d \cdot \vec{M} dV = \frac{\mu_0}{2} \int_V (\mathcal{N} \cdot \vec{M}) \cdot \vec{M} dV. \quad (2.43)$$

The energy contribution e_{shape} is minimised when \vec{M} is aligned parallel to an easy axis given by \mathcal{N} . The uncompensated magnetic moments at the surface also induce a field outside the material, called the stray field \vec{H}_s . The effect of these stray fields is essential for the formation of magnetic domains.

The formation of ferromagnetic domains without consideration of external fields is depicted schematically in figure 2.8. Figure 2.8(a) depicts a ferromagnet with a single domain, the direction of which is determined by the magnetocrystalline anisotropy. In this case, the shape anisotropy due to stray fields is at a maximum, leading to a large shape anisotropy contribution to F_{tot} . In (b) and (c) there is less contribution from stray fields due to the formation of oppositely aligned domains. The magnetostatic self-energy is minimised when domains of closure are formed, as seen in (d). In this case, all domain walls form at an angle of 45° with each other and the stray fields vanish completely. However, the formation of domain walls contributes positively to F_{tot} as e_{wall} because spins at both sides of a wall are not aligned in parallel, reducing the exchange interaction. In general, the minimisation of the competing energy contributions in F_{tot} determines the domain structure of a material.

In ideal antiferromagnets, a single domain structure is often energetically favoured because no stray fields exist that could contribute to F_{tot} . However, even in antiferromagnetic materials, the free energy contribution due to the formation of domain walls

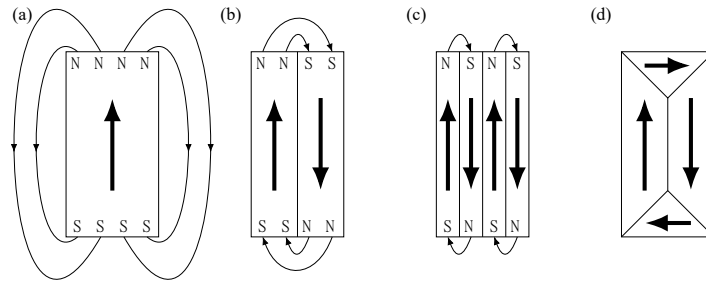


Figure 2.8: Domain formation in a ferromagnetic material because of the uncompensated stray field. The shape anisotropy sinks from (a) to (d) as domain walls are formed. Adapted from [11].

can be compensated for, resulting in multidomain structures. This can occur due to crystal defects, which inhibit the long range ordering of spins in the material.

In order to minimise the unfavourable effect on the exchange interaction of differently orientated domains, the change in spin direction occurs gradually over an area which defines the domain walls. There are two types of domain walls, inside which the spin direction changes along different planes. In Bloch-walls the spin flip takes place parallel to the domain wall plane, whereas in Néel-walls it takes place orthogonally to it. The width of a Bloch wall is determined by the combination of anisotropy energy contributions and the exchange interaction. Typical widths are in the range of multiple tens of nm. In thin films, Néel-walls are generally preferred, as the spin flips in Bloch-walls orthogonally to the surface would cause large stray fields.

2.4.4 Magnetisation curves

In order to characterise magnetic materials, field-dependent magnetisation curves can be taken. An external field \vec{H}_{ext} is applied and varied, while the material magnetisation in direction of \vec{H}_{ext} is measured. If the material is ferro-/ferrimagnetic, the result is a curve that shows hysteresis, as visible in figure 2.9.

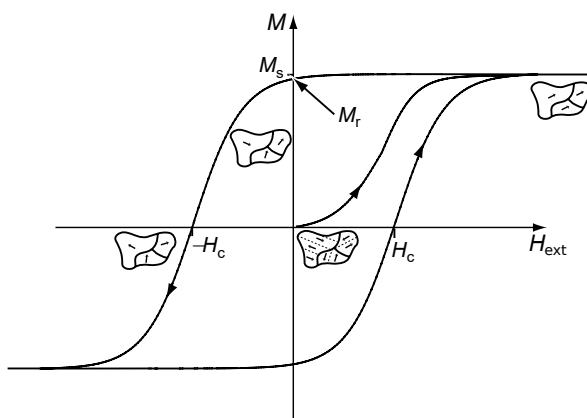


Figure 2.9: Typical magnetisation curve of a ferromagnet. The initial state is irreversibly altered by applying an external field \vec{H}_{ext} . The characteristic parameters M_S , H_c and M_r are annotated. The effect of the applied field on the domain structure is shown. Adapted from [27].

The introduction of \vec{H}_{ext} results in a non-zero Zeeman contribution to the total free

energy, which tends to align the material magnetisation parallel to the external field. This additional energy factor modifies the existing domain structure depending on the strength and direction of the external field relative to the magnetic axes in the material. Changes in the domain structure as response to the external field result in magnetisation curves that are characteristic of the material under investigation. At low fields, this effect is largely reversible, and the magnetic moments inside the domains are aligned parallel to the easy axes of the material. At high fields, the domain distribution shifts in an irreversible way and domains that align with \vec{H}_{ext} grow at the expense of domains oriented in unfavourable directions. At sufficiently high external fields, the material enters a monodomain state, which is gradually rotated in the direction of \vec{H}_{ext} until it reaches a saturation magnetisation M_S , if the latter is not oriented in the direction of an easy axis.

A ferromagnetic magnetisation curve exhibits multiple characteristic points. At high fields, the magnetisation \vec{M} approaches M_S , as already mentioned. If, from this point, the external field is lowered to zero, the magnetisation retains a remanence value M_r . The field H_c in the opposite direction that is needed to lower the magnetisation to zero is called coercivity. Barring effects like exchange bias interactions between antiferromagnetic and ferromagnetic phases or relaxation of the system at high temperature, magnetisation curves are symmetric about the origin of \vec{H}_{ext} once M_S has been reached at least once. Ferromagnetic materials can be roughly categorised into hard and soft magnets. Hard magnets usually exhibit high coercivities and remanence, while for soft magnets both values are lower. The coercivity of a material can also be raised due to impurities or influenced by strain and depends strongly on the orientation of \vec{H}_{ext} relative to the easy axes.

Antiferromagnetic materials exhibit magnetisation behaviour similar to that presented in figure 2.10. At sufficiently high external fields, antiferromagnets either show a metamagnetic transition into the saturated ferromagnetic state or a spin-flop transition with an intermediate canted state.

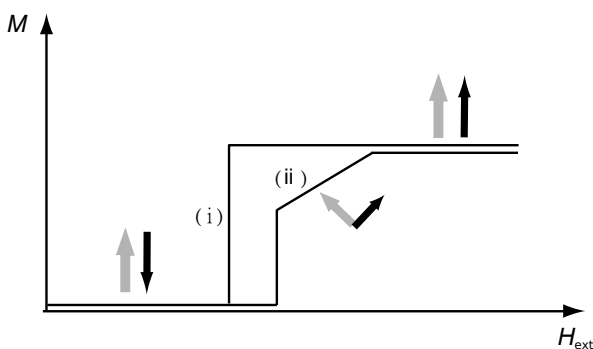


Figure 2.10: Field-dependent magnetisation of an antiferromagnet, with (i) a metamagnetic transition and (ii) a spin-flop transition. Adapted from [27].

Magnetisation curves of paramagnetic materials show no hysteresis opening and are linear around the origin. At very high fields ($H > 100$ T), all magnetic moments are aligned parallel to the external field, despite thermal fluctuations, which leads to saturation. The saturation fields are usually much higher than those of ferromagnets, because the individual moments do not interact [27]. Diamagnetic materials behave

similarly, with a purely linear response to the externally applied field.

Nanoparticle effects

There are more types of collective magnetic behaviour than the relative simple ones discussed in the previous sections. A magnetic effect related to the ferromagnetism of nanoparticles is known as superparamagnetism. At small particle sizes (below 15 to 100 nm), ferromagnets tend not to form domain walls, and instead exist in a single domain state [12]. The behaviour of the field-dependent magnetic moment of such a nanoparticle sensitively depends on the orientation of the externally applied field relative to the easy axes of the particle. If, however, the anisotropy energy - including magnetocrystalline, shape and surface contributions - is roughly equal to the thermal energy, the particle magnetisation starts to spontaneously reverse from one axis orientation to the other, even in the absence of an applied field [33, 28]. This results in the ensemble of nanoparticles exhibiting a magnetisation behaviour similar to that of paramagnets, with no remanence or coercivity (i.e. no hysteresis). The particles essentially behave like the local atomic moments inside a paramagnet. However, the individual magnetic moments are much larger than the paramagnetic atomic moments and the saturation magnetisation is reached at external fields that are a few orders of magnitude lower than in paramagnets [28]. For large particle sizes or low temperatures, the particles stop behaving superparamagnetically because the anisotropy energy starts dominating the thermal fluctuations, which restricts the particle orientation to the easy axes.

In a temperature curve of a nanoparticle ensemble cooled without an applied field (zero-field cooling, ZFC), the particles at low temperatures are aligned with the easy axes and are 'blocked' or frozen, and the magnetisation rises with temperature until the particles are maximally aligned with the external field and the superparamagnetic state is reached, at which point the magnetisation starts dropping with further temperature increase. This maximum in magnetisation is closely related to the average blocking temperature, at which the particles start to behave superparamagnetically because the time for a measurement exceeds the average particle relaxation time [34, 35]. In contrast, a field-cooling (FC) temperature curve, taken after cooling the system down while applying an external field, exhibits no blocking temperature maximum because the particles are already aligned with the external field, even at low temperatures. Consequently, a splitting of ZFC and FC curves is typical of superparamagnets [36]. At large temperatures above T_C of the particles, a transition from superparamagnetism to normal paramagnetism occurs [12]. Blocking temperatures can take values of up to multiple hundred K.

A similar temperature behaviour as in superparamagnets can be observed in so-called spin-glasses. These materials also show blocking or freezing at low temperatures, with an extremum in the ZFC curve. However, spin-glasses consist of ferromagnetic atom clusters, which are enclosed inside a material without collective magnetism. This results in interaction inside and between the clusters instead of the quasi-paramagnetic

behaviour in superparamagnets. The spin-glass freezing temperature depends on the cluster interactions and spin-glasses generally exhibit multiple complex magnetic transitions depending on the amount of ferromagnetic material and the temperature. Additionally, the transitions in spin-glasses are abrupt, in contrast to the gradual transition into the superparamagnetic phase. Experimentally, it can be difficult to differentiate between superparamagnets and spin-glasses. Typical freezing temperatures are in the range of up to 50 K [35].

2.4.5 Superconducting quantum interference device magnetometry

A superconducting quantum interference device (SQUID) is a highly sensitive magnetometer, based on the Josephson-effect between junctions of superconductors. In the following section, the underlying mechanisms of SQUID-magnetometry are briefly presented. More detailed information can be found in [37, 38, 39].

In a superconductor at low temperatures, electrons of opposite spin can enter pairwise coupled states because of their interaction with phonons, forming Cooper pairs [40], which are quasi-particles that can travel through the material without resistance and which behave like bosons. As such, they can enter the same quantum mechanical state, in which they can macroscopically be described by a single collective wave function $\Psi = \Psi_0 e^{i\theta}$, with Ψ_0 being the amplitude and θ being the phase of the system. Superconductivity can be described using the Bardeen–Cooper–Schrieffer (BCS) theory [41].

In a closed ring of a material in the superconducting state, the phase of the macroscopic wave function of the Cooper-pairs has to be coherent around the ring, that is, the phase has to be unaffected by tracing the wave contour around the whole ring. This results in only certain waves corresponding to certain macroscopic states being allowed for the Cooper-pairs inside the ring. If a magnetic flux Φ is introduced to the ring, it influences the phase according to the Aharonov-Bohm effect [42]. Since only certain states are allowed, only certain amounts of flux corresponding to transitions between these states are permitted into the ring. Additional flux is compensated for by an induced screening current in the conductor. This effect is called flux quantisation [43, 44]. It is found that magnetic flux inside superconductive rings can only exist in integer multiples of $\Phi_0 = h/2e$ (with the Planck constant h and the electron charge e), which is consequentially known as the flux quantum.

A Josephson junction denotes a thin, insulating or resistive - i.e. not superconducting - barrier between two superconductors. The Josephson effect describes the tunneling of Cooper pairs through a Josephson junction via coupling of the wave functions of both superconductors, the strength of which depends on the thickness of the junction [45]. The current I_j through the junction is given by

$$I_j = I_c \sin(\Delta\theta), \quad (2.44)$$

where $\Delta\theta = \theta_1 - \theta_2$ is the phase difference between the wave functions of both superconductors and I_c is known as the critical junction current. When a current is applied through the junction, the Cooper pairs tunnel through the barrier and the voltage across it remains zero until I_c is reached, at which point a voltage U across the junction results in a time-dependent shift of $\Delta\theta$ of the form

$$\frac{d\Delta\theta}{dt} = \frac{2\pi}{\Phi_0} U. \quad (2.45)$$

Principle of SQUID measurements

A SQUID sensor consists of a superconducting ring, with either one or two parallel Josephson junctions, depending on whether it is an RF (radio frequency) or DC (direct current)-SQUID. In this work, a DC-SQUID was used and consequently, only its function will be explained.

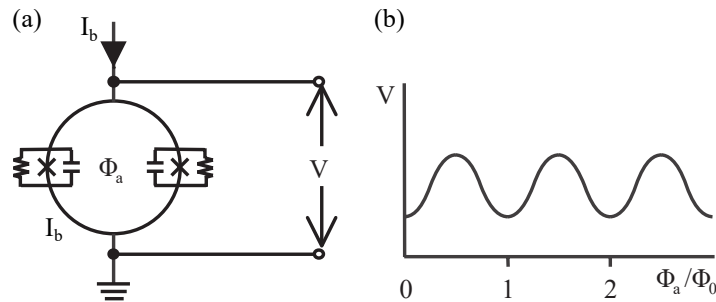


Figure 2.11: (a) Schematic of a dc SQUID sensor. Two superconductors encompass a ring, separated by two Josephson junctions. A constant bias current I_b is applied and the voltage across the ring is measured. An external magnetic flux ϕ_a induces a voltage change that oscillates with the magnetic flux (b). The junctions typically include shunt resistors, which counteract their self-capacitances, because they would otherwise result in hysteresis effects. Adapted from [37].

In a DC-SQUID (see figure 2.11), a constant bias current of $I_b > 2I_c$ is applied across the ring, which is distributed equally across both parallel junctions so that they conduct resistively, developing a small voltage U . If an external magnetic flux is introduced into the ring, it induces a screening current I_s inside the ring, as discussed previously. The screening current adds to the bias current in one junction, but is subtracted from the current in the other junction, because it tends to counteract the external magnetic field. This bias current leads to a change in U across the SQUID. The voltage changes periodically with the externally applied flux, with the period being Φ_0 . For integer multiples of Φ_0 , there exists no screening current and the voltage is at a minimum, while it reaches its maximum at half integer multiples. This makes it possible to detect magnetic fluxes even smaller than the flux quantum Φ_0 by measuring the voltage across the SQUID. Through the use of feedback electronics, the working point of the SQUID can be adjusted to be close to the maximum of the voltage period. In this region, a

small voltage change is approximately linearly proportional to a change in magnetic flux.

2.5 Core-level spectroscopy

In this chapter, three core-level spectroscopy techniques, namely X-ray photoelectron spectroscopy (XPS), X-ray absorption spectroscopy (XAS) and X-ray magnetic circular dichroism spectroscopy (XMCD), are introduced. First, an overview over photoexcitations is given. After that, each of the techniques is described. The information presented in this chapter is compiled from [26, 46, 47, 48, 49].

2.5.1 Photoexcitations in core-level spectroscopy

The spectroscopic techniques XPS, XAS and, by extension, XMCD can be classified as core-level spectroscopies, because they utilise the excitation of localised core-electrons by photons in the X-ray range to probe the density of states in various ways. The main difference between XPS and XAS is whether occupied core-levels or unoccupied states in the valence and conduction bands are probed by exciting the core-level electrons into the continuum (XPS) or into valence and conduction states (XAS). The mentioned techniques are optical processes of first order, i.e. only one photon and one electron are involved in the excitations. This is in contrast to techniques like fluorescence or Auger electron spectroscopy, which use second-order relaxation processes of the excited system.

Generally, photoexcitations of electrons in atoms or solids can be described in terms of the transition from an initial ground state with wave function Ψ_i into an excited final state Ψ_f , in which an electron is excited into an unoccupied state above the Fermi level, leaving behind a core-hole. The photon is considered a perturbation to the system and the transition probability is given by Fermi's golden rule:

$$W(f, i) = \frac{2\pi}{h} |\langle \Psi_f | \mathbf{T} | \Psi_i \rangle|^2 \cdot \delta(E_f - E_i - E_{\text{ph}}), \quad (2.46)$$

with the Planck constant h , the Dirac delta distribution $\delta()$, the transition operator \mathbf{T} between initial and final state, their respective energies E_i and E_f , and the energy E_{ph} of the involved photon, which has to be equal to the difference between final and initial state for a transition to be allowed.

In the soft X-ray region, the transition operator in equation 2.46 can approximately be described by the dipole operator \mathbf{p} , ignoring quadrupole transitions. This operator imposes certain selection rules on the allowed transitions, limiting the change in spin $\Delta S = 0$, in orbital angular momentum $\Delta L = \pm 1$ and total angular momentum $\Delta J = +1, 0, -1$.

2.5.2 Principle of X-ray photoelectron spectroscopy

In order to examine the electronic structure of occupied core-states in the surface region, X-ray photoelectron spectroscopy is used. The basis of XPS measurements is the external photoelectric effect induced in the sample by exposing it to photons of the energy

$$E_{\text{ph}} = h\nu, \quad (2.47)$$

where ν is the electromagnetic frequency of a photon and h is the Planck constant. If E_{ph} is sufficiently high, a single electron in an atomic state with the binding energy E_{B} can absorb a photon and be emitted from the sample surface with the kinetic energy

$$E_{\text{kin}} = E_{\text{ph}} - E_{\text{b}} - \Phi_{\text{S}} \quad (2.48)$$

where Φ_{S} is the work function of the sample, defined as the energy difference between the Fermi-level and the vacuum energy level at the sample interface, and E_{B} is the difference between the Fermi-level and the energy of the core-level of the excited electron, as shown in figure 2.12. The kinetic energy can be measured by an electron energy analyser, which is typically grounded to the same potential as the sample, equalising their Fermi levels. In this case the kinetic energy has to be corrected by the work function Φ_{A} of the analyser instead of the sample work function:

$$E'_{\text{kin}} = E_{\text{ph}} - E_{\text{b}} - \Phi_{\text{A}} \quad (2.49)$$

It is apparent that E_{b} can be determined from equation 2.49 if the values of both Φ_{A} and E_{ph} are known. However, the binding energy measured in XPS is not the energy E_i^N of the initial state with N electrons, because of the creation of a core-hole in the final state E_f^{N-1} , resulting in

$$E_{\text{b}} = E_f^{N-1} - E_i^N. \quad (2.50)$$

E_{b} in equation 2.50 generally depends on many-body effects between the electrons, which can be partially approximated using Koopmans' theorem [51]. However, this approximation neglects e.g. relaxation processes during the core-hole formation. In general, the measured binding energies are reasonably close to the atomistic one-electron values, so that deviations from them can be understood in terms of chemical shifts and satellite structures [26], discussed in more detail in the next section.

The binding energy of an electron depends on its interactions with the atom core as well as with other electrons and can take on discrete, element and orbital specific values. This allows for the elemental identification and characterisation of the sample material by measuring the number of (elastically scattered) electrons that reach the analyser for a range of kinetic energies. The orbital binding energies appear as local maxima in a plot of the electron counts versus E_{kin} (see figure 2.12). Comparison of the areas under the intensity peaks enables the quantitative analysis of the chemical composition of the sample.

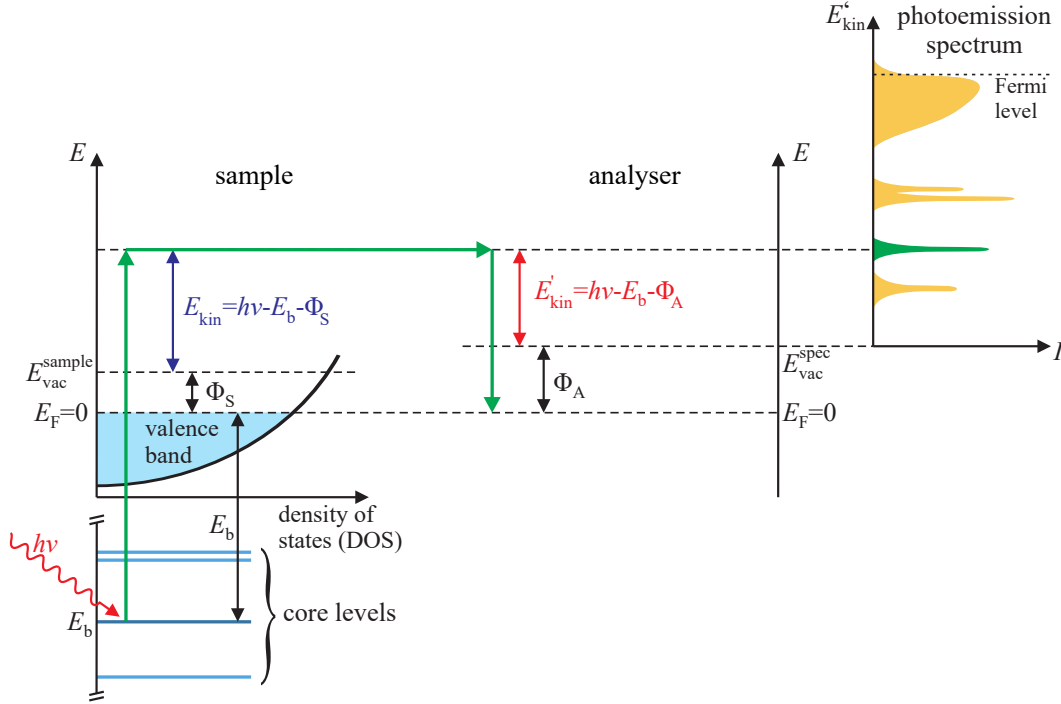


Figure 2.12: Principle of the X-ray photoemission process. A photon with energy $h\nu$ excites a core-electron with binding energy E_b and work function Φ_S into the continuum with a kinetic energy E_{kin} . At the spectrometer analyser with work function Φ_A , the photoelectron is detected with a kinetic energy $E'_{\text{kin}} = E_{\text{ph}} - E_b - \Phi_A$. On the upper right, the schematic of a photoelectron spectrum is depicted. Adapted from [19, 50].

2.5.3 Quantitative analysis of XPS features

The intensity of photoelectrons reaching the analyser can be described in a simplified form with the use of approximations concerning the photoemission process. In the straight-line approximation, elastic scattering is neglected and it is assumed that photoelectrons are emitted in a straight line from the sample. The intensity I^k of electrons emitted with the kinetic energy E_k from the orbital k of a specimen with the thickness t , that are measured by the analyser, is then given by [49]

$$I^k = J_0 \frac{d\sigma_k}{d\Omega} (h\nu) \Omega_0(E_k) A_0(E_k) D_0(E_k) N_t \Lambda_e(E_k) (1 - e^{-\frac{t}{\Lambda_e(E_k) \sin \theta}}) \cdot R(E_k, \theta), \quad (2.51)$$

where J_0 is the X-ray flux, which is taken as nearly constant as long as the experiment is not performed at a grazing incidence angle and without a focused, monochromatic source, $\frac{d\sigma_k}{d\Omega}$ is the differential photoelectric cross-section for the k -subshell, $\Omega_0(E_k)$ is the mean acceptance solid angle of the analyser that is approximately applicable over the part of the sample volume that is included in the projection of the effective aperture $A_0(E_k)$ of the analyser along the mean electron emission direction, given by the angle θ relative to the sample surface, $D_0(E_k)$ is the detection efficiency of the analyser, N_t is the number of atoms or molecules per unit volume in the specimen from which emission occurs, $\Lambda_e(E_k)$ is the attenuation length of the emitted electrons in the sample and

$R(E_k, \theta) \approx R(\theta)$ is the angle-dependent instrument response function of the analyser. The exponential term models the intensity drop-off due to inelastic scattering of the electrons on their way to the sample surface.

For most instrument geometries, Ω_0 and θ can be taken as nearly constant along the sample from which electrons are emitted. This means that the angle-dependency of the instrument response can usually be neglected. The attenuation length $\Lambda_e(E_k)$ usually equals the inelastic mean free path (IMFP), which was briefly discussed in section 2.2. Depending on the model, the attenuation length can be shortened to account for elastic scattering effects, which are otherwise neglected in equation 2.51. Since the IMFP of photoelectrons excited in the soft X-ray region is much shorter - in the range of 2 nm - than the penetration depth of X-rays in solids, it is the limiting factor in the probing depth of XPS [49, 12].

Utilising the simplifications of the measurement geometry described above, $\frac{d\sigma_k}{d\Omega}$ can be approximated with the total photoelectric cross-section $\sigma_k^t(h\nu)$, if unpolarised or circularly polarised soft X-rays are used and the spectrometer is set up with the 'magic angle' of $\alpha = 54.7^\circ$ between the X-ray source and the analyser [52, 49]. At higher energies, when the above simplifications do not hold, or when elastic scattering is considered, additional terms make this approximation inaccurate [53, 54].

Rearranging equation 2.51 and applying the approximations discussed above gives the atom density¹ of element A by measuring the orbital j :

$$N_A = \frac{I_A^j}{J_0 \sigma_{A,j}^t(h\nu) \Lambda_e(E_j) T_0(E_j, \theta, t)}, \quad (2.52)$$

where $T_0(E_j, \theta, t)$ is the combination of all instrument and geometry effects in equation 2.51 and the product of $T_0(E_j, \theta, t)$, $\sigma_j^t(h\nu)$ and $\Lambda_e(E_j)$ is often referred to as relative sensitivity factor [55]. It is assumed that there is no material composition gradient in relation to the sample depth.

With equation 2.52, the relative quantities of elements A and B , measured in the orbitals j and k , respectively, can be determined:

$$\frac{N_A}{N_A + N_B} = \frac{I_A^j / J_0 \sigma_{A,j}^t(h\nu) \Lambda_e(E_j) T_0(E_j)}{I_A^j / J_0 \sigma_{A,j}^t(h\nu) \Lambda_e(E_j) T_0(E_j) + I_B^k / J_0 \sigma_{B,k}^t(h\nu) \Lambda_e(E_k) T_0(E_k)}, \quad (2.53)$$

which can be approximately simplified to

$$\frac{N_A}{N_A + N_B} \approx \frac{I_A^j / \sigma_{A,j}^t(h\nu)}{I_A^j / \sigma_{A,j}^t(h\nu) + I_B^k / \sigma_{B,k}^t(h\nu)} \quad (2.54)$$

if the investigated orbitals of elements A and B are close in binding energy. Under the given approximations, only knowledge of the orbital intensities and cross sections of the relevant orbitals is required to determine the stoichiometry of the surface material.

¹More precisely, the number of atoms in the unit volume

Theoretically calculated cross-sections of most materials can be found in tabular works [56].

In order to determine the intensities used in equation 2.54, the XP-spectrum lines corresponding to the orbitals under investigation can be measured. However, the orbital lines are broadened by Lorentzian and Gaussian contributions because of the lifetime broadening of the excited states and instrumental effects, respectively. For this reason, the intensities are evaluated in terms of the area under the peaks of interest [57]. The broadened peaks of different transitions often overlap and so it is necessary to deconvolute the spectra by the use of curve fitting techniques. The measured data are approximated by use of Gaussian-, Lorentzian- and Voigt curves that are adjusted for an optimal fit with the data under parameter constraints specific to the elements and orbitals that are being investigated. Additionally, a background of photoelectrons that underwent inelastic scattering before arriving at the detector is subtracted from the data. Multiple algorithms for determining the inelastic scattering background exist, of which the Shirley-background was used in all quantitative analyses of XP-spectra in this work. A detailed description of this background can be found in [58].

Spectral features

Multiple spectral features present in XPS can be used to acquire information about the material under investigation. The dominant spectral features are core-level photoionisation peaks and peaks of Auger-emission electrons. They are accompanied by a multitude of satellite features. A short overview of the different features is given below.

Auger-electron peaks

During XPS, not only primary photoelectrons arrive at the detectors. The release of so-called Auger electrons is an auxiliary process that involves three electrons. A primary photoelectron exits the atom and leaves behind a vacant energy level. This vacancy can be filled by an electron from a higher energy level. The difference in energy between these two levels can be transmitted as a photon in the case of fluorescence or to a third electron in the atom. If the energy thus transmitted is larger than the electron's binding energy and work function, the electron can be detected much like a primary photoelectron.

Auger electron peaks differ from primary photoelectron peaks insofar that the kinetic energy of the Auger electron is independent of the photon source energy because it results from the difference in electron energy states in the atom. This means that the measured binding energy determined from equation 2.49 for Auger peaks depends on the photon source. Consequently, Auger peaks can be differentiated from photoelectron peaks by varying the photon source.

Auger electron peaks are element-specific and tabulated for common materials and photon sources [59]. The quantification of XP-spectra can be made difficult if an Auger peak superimposes on a photoelectron peak.

Satellite features

Shake-up satellites occur when photoelectrons excite longitudinal excitons or valence electrons to a higher energy level, either in the same atom or intra-atomic [26]. As such they present at discretely higher binding energies than the corresponding main peak in the case of transition metal oxides. If the excitation energy of the secondary electron is sufficient to ionize it into the vacuum, the process is called shake-off, with broad satellite features because the transitions are continuous. Shake-up satellites are mostly present in transition metals and aromatic structures.

Another kind of satellite feature is caused by charge-transfer effects, in which electrons are (partially) transferred from a ligand to a transition metal, typically from the O 2p orbitals of transition metal oxides to the M 3d orbitals. Such a charge-transfer can be induced by the photoexcitation, resulting in the kinetic energy of the photoelectrons being reduced by the charge-transfer energy Δ . For this reason, the satellites occur at higher binding energies than the main transition peak. A more detailed description of charge-transfer effects is given in 2.5.6.

Spin-orbit splitting

If the angular momentum quantum number l of an orbital is larger than zero, its energy states are split because of spin-orbit interactions of the available electron states, which make it necessary to define a total angular momentum j . In the single electron approximation that is often used for the core energy levels in XPS, this means that the electron (final) states split into two, where the energy depends on the spin of the electron. The split in binding energies can be seen in the XP-spectrum, although it can oftentimes not be resolved. The two states have different degeneracies $2j + 1$, the ratio of which determines the intensity ratio measured in XPS.

Multiplett splitting

Multiplet splitting arises from the Coulomb and exchange interactions of electrons in the core-levels and those in the valence states, both in the initial and final states. These interactions result in a multitude of additional states (the multiplets) and consequently in photoemission lines, when these are probed in XPS. For orbitals with $l > 0$, these lines overlap close to the main line, forming its lineshape. Multiplet effects are discussed in more detail in section 2.5.6.

Charging effects

If the surface material of a sample is isolating, a positive charge will accumulate in the atoms during an XPS measurement because the holes left by the photoelectrons cannot be filled [60]. This means that the electrons in the atoms are subject to Coulomb forces in addition to their binding energy, which results in a higher binding energy being measured at the detector. This shift of E_b has to be corrected for by comparison with expected binding energy values from literature. Additionally, a small part of the

electrons will arrive at the detector without being influenced by the built up charges, which can lead to small additional peaks at the expected E_b values.

Chemical shift

Similar to charging effects, chemical shift refers to a difference in measured binding energies of photoelectrons due to electrostatic effects. In the case of chemical shifts, these effects are caused by the difference in formal charges in different oxidation states of the same species [61]. The binding energy rises with higher oxidation states because the remaining electrons experience less screening from the core potential. If an element is present in different valencies, the peaks may overlap and appear as one broadened peak if the measurement resolution is insufficient.

2.5.4 X-ray absorption spectroscopy

The underlying principle of X-ray absorption spectroscopy is presented in figure 2.13. Photons with variable energy are projected onto the sample surface, where they interact with the electrons in the material and are absorbed, similar to XPS. The absorption process can be quantified by the absorption coefficient $\mu(h\nu)$. At element- and orbital-specific photon energies, peaks of the absorption coefficient occur, called absorption thresholds or absorption edges. They can be related to excitations of core electrons into higher, unfilled core- or valence states, in contrast to the excitations into the vacuum in XPS. In this way, the absorption coefficient is a probe for the density of unfilled states in a given binding energy range, which makes it a useful tool for investigating chemical compositions, coordinations and valencies of the involved atoms. For 3d transition metal oxides, the investigated excitations are usually dipole transitions from the filled 2p orbitals into empty states of the partially filled 3d orbitals.

The energy dependent absorption coefficient μ can be indirectly measured in several modes, among them the measurement of the photon transmission, the measurement of the total electron yield (TEY) and the fluorescence yield (FY).

In the transition mode of XAS, the intensities I_0 and $I(z)$ of the photon beams before and after passing through the sample are measured and used to determine the absorption coefficient² using the Lambert-Beer law:

$$I(z, h\nu) = I_0(h\nu)e^{-\mu(h\nu)z}, \quad (2.55)$$

assuming a homogeneous material, with the effective sample thickness z being determined by the thickness of the sample as well as the angle of incidence. $I(z, h\nu)$ and $I_0(h\nu)$ are the transmitted and incident photon intensity, respectively. The effect of z can be compensated for by normalizing the intensity to the edge maximum, so that, ideally, $\mu(h\nu)$ is measured directly via equation 2.55. Transmission measurements can

²More precisely, the Lambert-Beer law describes the attenuation coefficient, which includes scattering effects. These are relevant e.g. in EXAFS fit models.

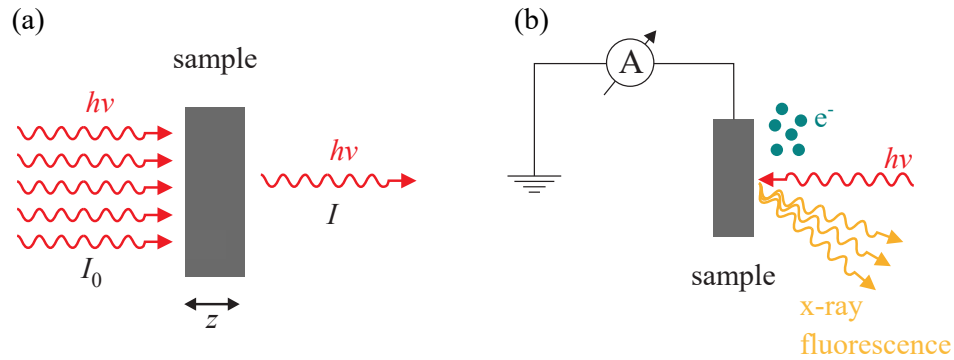


Figure 2.13: Principle of XAS using different spectroscopy methods. (a) Transmission measurements are the most direct way of measuring the absorption coefficient, but they depend strongly on the thickness z of the sample under investigation. Instead, core-hole relaxation processes (b) are usually used to approximately determine the absorption coefficient. Fluorescent yield measures the fluorescent photons with a photo-diode and is bulk-sensitive, while the total electron yield measures the current of electrons leaving the sample, resulting in a high surface sensitivity. Depicted is one possible way of measuring TEY, by detecting the compensation current from ground to the sample caused by the absorption process. Adapted from [19].

be used to gather bulk information, but samples have to be thin in order to transmit enough light to the detector because the X-ray attenuation length is in the μm -range far from the absorption edges and even lower at the edges. In thicker samples, the signal to noise ratio suffers as a result. Thickness effects resulting from inhomogeneous samples and pinholes can also distort the spectrum by introducing non-linear material responses, which can influence the quantitative analysis, especially in the soft X-ray range [62]. Absolute absorption coefficient values can generally only be directly measured by transmission measurements, although it is in principle possible to approximate them with the total yield methods described below [26].

When core electrons are excited in the process of absorbing a photon, the resulting core hole can be filled by electrons in higher energy states, consequently emitting either fluorescent photons or electrons in an Auger process. The emitted Auger electron likewise leaves a core hole, which can lead to a cascade of Auger processes triggered by the initial photon absorption. Any process, by which the hole is filled, is proportional to the absorption of a photon, and can therefore in principle be used as a measure of the absorption coefficient [26].

In the TEY mode of measurement, all electrons emitted from the sample are measured. This can be done either by measuring the drain current from a conductive wire (connected to ground) into a conductive sample, which serves to compensate for the electrons emitted by the absorption process, or by detecting the emitted electrons that are accelerated onto a channeltron detector, where they induce an amplified current. The electron yield of non-conductive samples can be measured as well, e.g. by using high collection voltages at the detector or by embedding the sample in a metallic grid [62]. The measured TEY current includes a continuously rising background of elec-

trons that were ionised directly by the photons from states with $E_B < E_{\text{ph}}$, as well as the electrons from Auger cascade processes and secondary electrons, all of which can experience additional inelastic scattering processes before leaving the sample. TEY is very surface sensitive compared to the other measurement modes because the information depth is generally limited by the inelastic mean free path of electrons inside the material, similar to XPS. The probing range of XAS consequently lies in the range of 2 - 10 nm [26, 63], although the probing range can in principle be extended to about 200 nm if electrons emitted by re-absorption of fluorescent photons are considered [64]. However, this contribution is usually negligible in the soft X-ray regime (< 3 keV), where Auger processes dominate the fluorescence process. At high photon energies and high atomic numbers, the fluorescence process becomes more relevant.

The measured TEY intensity depends both on the electron escape depth λ_e as well as the X-ray penetration depth λ_p [26]:

$$I_{\text{TEY}} \propto \frac{\lambda_e}{\lambda_e + \lambda_p \sin \alpha}, \quad (2.56)$$

with the angle of incidence α relative to the surface plane. From equation 2.56, it is apparent that the TEY-intensity is approximately proportional to $\mu = \frac{1}{\lambda_p}$ if $\lambda_e \ll \lambda_p \sin \alpha$. λ_e is related to the IMFP of electrons and λ_p depends on the photon energy. The approximation can break down close to absorption maxima, where λ_p can take on values below 20 nm, especially at grazing photon incidence. As a consequence, saturation effects appear in the form of compressed absorption peaks in the measured spectra. In principle, these can be compensated for either by relating the measured intensities to theoretically calculated absorption coefficient curves at energies far from the peak [65], by using empirical correction factors acquired by sum-rule analysis [66] or by measuring angle-dependent spectra [67]. Compared to the other methods of measuring XAS, TEY measurements display a good signal-to-noise ratio because of the electron cascades, which amplify the individual absorption processes.

The FY mode works similarly to TEY, with the intensity of emitted fluorescent photons (measured with a photo-diode) instead of emitted electrons being taken as a measure of the absorption coefficient. FY is more bulk-sensitive than TEY because the fluorescence photons have an attenuation length of similar magnitude as the incident photons, but it suffers from a poor signal to noise ratio, especially in the soft X-ray regime where Auger processes dominate. Self-absorption and saturation effects can influence the resulting spectra, and usually do so more substantially than in TEY measurements. Additionally, the fluorescence decay can vary strongly over L- or M-edges, depending on the final state symmetries. This can lead to some peaks not being visible in FY at all [68, 62]. Detailed calculations are necessary to evaluate FY spectra quantitatively [69, 70].

XAS analysis can be divided into structures near the absorption edge (X-ray absorption near edge structure, or XANES) and those at higher energies (Extended X-ray absorption fine-structure or EXAFS). In both cases, the spectrum around a given absorption edge is divided into the pre-edge, edge and post-edge regions. Absorption structures in

the pre-edge region are dominated by quadrupole transitions and those into hybridised MO-orbitals, which are less likely than the dipole transitions that dominate the edge transition multiplet structure. In the post-edge region, which is the area of interest for EXAFS, oscillations in the absorption occur, which are caused by scattering effects and interference of the emitted electron wave with itself. For further information on EXAFS, see [71]. In this work, XANES is used exclusively.

2.5.5 X-ray magnetic circular dichroism

When XA-spectra of a magnetic material are measured using circularly polarised photons, the absorption at the $L_{2,3}$ edges depends on the helicity of the circular polarisation. This effect is called X-ray magnetic circular dichroism (XMCD). It results from spin-dependent absorption as shown in figure 2.14. It can be described with a two-step model [72], which will be presented here for simplicity in the context of an atomic one-electron system.

In the first step, core electrons are excited by circularly polarised photons. Due to their circular polarisation, the photons have an angular momentum of $\pm\hbar$ (depending on the helicity), which is transferred to the excited electrons in order to satisfy the conservation of angular momentum. If the electron is excited from a state with no spin-orbit splitting, the momentum is transferred only to its orbital momentum [72]. If it is instead excited from a state that exhibits spin-orbit splitting, a part of the momentum is transferred to the electron's spin. This, along with the fact that circularly polarised photons obey an additional dipole selection rule ($\Delta m_j = \pm 1$ depending on helicity), results in the excited electrons becoming spin-polarised because excitations of electrons with one of the spin directions are preferred. The preferred spin direction depends on the helicity of the photons as well as the spin-orbit coupling. For the $L_{2,3}$ excitations from the spin-orbit split $2p_{3/2}$ and $2p_{1/2}$ levels, this results in opposite spin polarisation (of different magnitudes). This polarisation due to the spin transfer of photon momentum is known as Fano effect [73]. This first step is independent of the magnetic properties of the material under investigation.

The second step involves the valence shell into which the spin polarised electrons are excited. Owing to exchange interaction effects that are discussed in section 2.4.2, the valence shell can be energetically split in majority and minority spin states, i.e. the spin-up and spin-down valence states are unequally occupied. Because an unequal number of states is available for the excited electrons of different spins to move into, and because spin-flips are not allowed in dipole transitions, electrons with one spin orientation are preferentially accepted during absorption. The absorption spectra with opposite helicities then exhibit different intensities at the transition energies required for the transition into these unequally occupied valence states because the transition probability is proportional to the density of unoccupied available states. In this way, the unoccupied states act as a spin-sensitive detector for the spin polarised excited

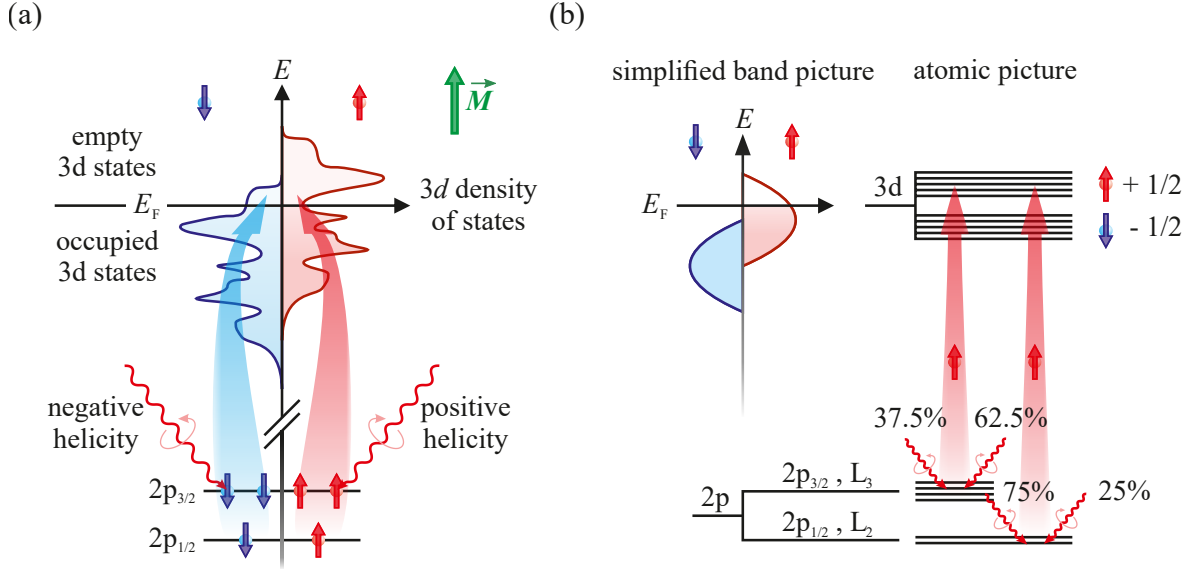


Figure 2.14: XMCD-effect of a 3d transition metal at the $L_{2,3}$ absorption edges. (a) Electrons are excited from the spin-orbit split 2p states into empty 3d valence states. The electrons are spin-polarised depending on the photon helicity and the valence states are spin-split because of exchange interactions, resulting in an unequal density of empty spin-up and spin-down states that acts as a spin sensor for the excited electrons. (b) The spin-polarisation of the electrons excited by photons of the same helicity differs between the spin-orbit split 2p states, both in sign and magnitude. The MCD-effect is maximised if the spin-down 3d states are fully occupied, allowing only spin-up electrons to be excited. Adapted from [74].

electrons. The difference between the two XA-spectra μ_+ and μ_- is the XMCD signal

$$\mu_{XMCD} = \mu_+ - \mu_- \quad (2.57)$$

which depends sensitively on the imbalance of the spin-dependent density of valence states, while the spectrum without polarisation effects can be acquired via

$$\mu_{XAS} = \mu_+ + \mu_- . \quad (2.58)$$

The above discussion assumes that the photon incidence is parallel to the magnetisation direction of the sample, given by an applied external field. In a thin film, this typically means that the polarisation plane is parallel to the surface normal. At higher incidence angles, the MCD-effect is diminished and at orthogonal incidence, it disappears. Lowering the degree of photon polarisation additionally diminishes the dichroic effect. Outside of the atomic one-electron approximation, the effect of the photon helicities on the electron spin polarisation is given by the transition matrix elements in equation 2.46. In the experiment, switching the direction of the sample magnetisation or the photon helicity is functionally equivalent, barring distortion effects induced by the externally applied magnetic field [62].

In non-magnetic materials, both spin orientations are equally occupied and consequently no XMCD signal can be observed. In this way, the XMCD signal is directly

related to the spin magnetic moment of the investigated atoms. If spin-orbit splitting of the valence shell is considered as well, the MCD signal also probes the orbital moment [72]. Both contributions can be experimentally extracted and separated via use of the sum rules, which are described in the following section.

Sum rules

As mentioned, the XMCD and XA-spectra taken together contain information about the (element-specific) orbital and spin moments. Both contributions can be separated approximately for a given cation or atom in 3d transition metals by use of the sum rules first proposed by Thole and Carra *et al.* [75, 76]. Using the sum rules, the orbital moment contribution m_o can be determined as

$$m_o = -\frac{4q}{3r}(10 - n_{3d}), \quad (2.59)$$

where $q = \int_{L3+L2} \mu_{\text{XMCD}} dE$ and $r = \int_{L3+L2} \mu_{\text{XAS}} dE$ with \int_{L3+L2} being the integral over the energy range encompassing both L-edges and n_{3d} being the number of holes or unoccupied 3d states in the investigated transition metal atom or cation. Similarly, the separated spin moment can be determined as

$$m_s = -\frac{6p - 4q}{r}(10 - n_{3d}) \left(1 + \frac{7 \langle T_z \rangle}{2 \langle S_z \rangle}\right)^{-1}, \quad (2.60)$$

where $p = \int_{L3} \mu_{\text{XMCD}} dE$, and where $\langle T_z \rangle$ and $\langle S_z \rangle$ are the expectation values of the magnetic dipole and spin operators in z-direction in the ground state, respectively. In bulk cubic crystals, the last term can usually be neglected because $\langle T_z \rangle \ll \langle S_z \rangle$.

As the sum rules only apply for the L-edge transitions, i.e. transitions of the form 2p→3d, other transitions measured in the spectrum close to the edges must be subtracted before evaluation of the moments. Transitions into the continuum above the 3d states can be modelled and subtracted using step functions [77]. The previously mentioned saturation effects can have a severe influence on the results of the sum rule analysis, even if the sum rules are otherwise applicable in good approximation. A common result of saturation effects is that the determined orbital moment is smaller than the 'real' value [66].

2.5.6 Multiplet calculations

The XA-spectra in this work are numerically evaluated using a set of models that collectively encompass the charge-transfer multiplet theory. The basis for this model is given by calculations of electron transitions in multi-electron atoms, also known as atomic multiplets. The ground state electron configuration of the cations in transition metal oxides is usually of the form $2p^6 3d^n$. After a photon absorption at the L-edge, a core electron excitation leaves the atom in the final state of the form $2p^5 3d^{n+1}$. In order

to calculate the theoretical transition probabilities and consequently the intensities - which are later used for comparison in the experimental analysis - equation 2.46 has to be evaluated, which requires terms for the initial and final wave functions $\psi_{i,f}$. The wave functions can be acquired by solving the Schrödinger equation for the atomic multi-electron Hamiltonian

$$H_a = \sum_i^N \frac{\mathbf{p}_i^2}{2m} + \sum_i^N \frac{-Ze^2}{r_i} + \sum_{i,j} \frac{e^2}{r_{ij}} + \sum_i^N \zeta(\mathbf{r}_i) \mathbf{L}_i \cdot \mathbf{S}_i, \quad (2.61)$$

which can be separated into terms for the average kinetic and potential energy of the electrons in the nucleus field, the Coulomb repulsion between electrons, and their spin-orbit coupling. The first two terms are the same for all electrons in a given atomic orbital and they can be treated as an energy offset, while the other contributions give the relative energies in a configuration [78]. The individual energy contributions of equation 2.61 can be approximately determined via atomistic Hartree-Fock calculations [79].

The spin-orbit coupling energy contribution in the ground state is limited to the 3d electrons because the 2p orbital is filled, and takes the form

$$\epsilon_{3d} = \langle 3d^n | \zeta_{3d} \mathbf{L}_{3d} \cdot \mathbf{S}_{3d} | 3d^n \rangle, \quad (2.62)$$

with the spin and orbital angular momentum operators \mathbf{S}_{3d} and \mathbf{L}_{3d} and the coupling strength ζ_{3d} . A similar spin-orbit term for the 3d orbital contributes to the final state energy, with an additional 2p-contribution

$$\epsilon_{2p} = \langle 2p^5 | \zeta_{2p} \mathbf{L}_{2p} \cdot \mathbf{S}_{2p} | 2p^6 \rangle \quad (2.63)$$

resulting from the core hole in the 2p orbital.

The Coulomb energy term for the initial state can be treated as briefly mentioned in section 2.4.2 by applying the Coulomb operator:

$$\langle 2p^6 3d^n | \frac{e^2}{r_{12}} | 2p^6 3d^n \rangle = \sum_k f_k F_{dd}^k + \sum_k g_k G_{dd}^k \quad (2.64)$$

with the radial Slater-Condon parameters F_{dd}^k and G_{dd}^k separated from the angular parts of the calculated Hartree-Fock matrix element via the Wigner-Eckhart theorem [80]. In practice, they are typically reduced to 80% of their Hartree-Fock values [78]. The parameters are only non-zero for certain k , depending on the electron configuration. The final state contains a similar Coulomb energy contribution, which depends on the wave function overlap of the 2p core-hole and the 3d valence states. The interactions resulting from this overlap are commonly referred to as multiplet effects [78] and they can result in substantial splitting, depending on the size of the Slater-Condon parameters.

It should be noted that the exchange terms G_{dd}^k in equation 2.64 and similar G_{pd}^k terms for the final state are related to the intra-atomic electron exchange concerning the

atomic 2p and 3d states, which is not to be confused with the inter-atomic exchange that is responsible for collective magnetism as described in section 2.4.2. The latter is only considered in the calculation of MCD spectra and will be discussed further below.

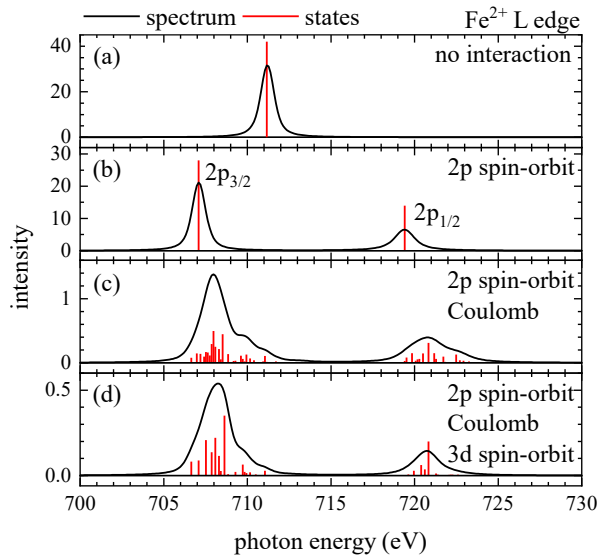


Figure 2.15: Exemplary results of atomistic multiplet calculations for the L-edge of Fe^{2+} cations. (a) and (b) show the case of transitions in the single-electron picture with and without 2p spin-orbit interactions of the final state. In (c) and (d), the effects of multi-electron Coulomb interactions of the initial and final state as well as 3d spin-orbit coupling are introduced, resulting in a multiplet of transition lines. The lines are broadened with Gaussian and Lorentzian curves. Adapted from [81].

As mentioned previously, the transition operator is typically approximated with the dipole operator because multipole transitions are orders of magnitude less likely to occur in the soft X-ray regime than dipole transitions. With the transition operator as well as the initial and final wave functions (approximately) known, the transition probabilities can be calculated using equation 2.46. The discrete transition lines that result from these atomistic multiplet calculations are subsequently broadened by a mixture of Gaussian and Lorentzian functions to account for experimental effects as well as core-hole lifetime broadening as is also done in XPS. As an example, the result of multiplet calculations for an Fe^{2+} cation is presented in figure 2.15, where the effect of individual contributions to the atomistic Hamiltonian is shown.

Ligand field splitting

The atomistic model introduced above neglects any influence of the crystal structure in which the cations are embedded. In order to account for the electrostatic interactions with the electrons of the surrounding ligand atoms (usually O^{2-}), an additional energy term H_{cf} - known as the ligand- or crystal field - can be added as a perturbation to the atomistic Hamiltonian. The ligand field depends on the symmetry of the crystal environment around the absorbing atom. In transition metal oxide spinels, only two kinds of ligand field symmetry have to be considered, barring distortion effects. The cations can occupy either tetrahedral or octahedral places, in which they are surrounded by ligands forming either a tetrahedron or an octahedron, as is visible in figure 2.16. Despite their difference in symmetry, both arrangements can be described by a common energy parameter $10Dq = E_{e_g} - E_{t_{2g}}$, which determines the additional splitting of the previously degenerate 3d states into t_{2g} and e_g states (or t_2 and e in the

tetrahedral symmetry) induced by the crystal field [82]. In transition metals, the splitting parameter is generally positive for the octahedral and negative for the tetrahedral coordination. In this description, the additional splitting by Coulomb and spin-orbit effects is not yet considered.

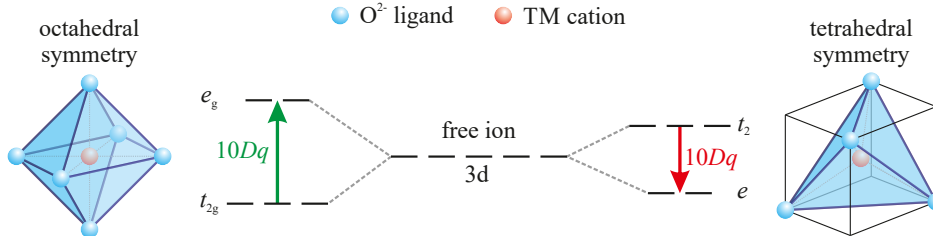


Figure 2.16: Principle of ligand field splitting for transition metal cations surrounded by oxygen ligands in the octahedral and tetrahedral symmetry. The degenerate 3d states of the free cation are split depending on the symmetry. The splitting is described by the common parameter $10Dq$. Adapted from [74].

Charge-transfer

An additional effect influencing the possible transitions is the charge-transfer between the ligands and the absorbing cation [26]. In this process, an oxygen ligand (partially) transfers one of its 2p electrons to a free state in the 3d orbital of the transition metal. For an L-edge absorption process this is modelled by mixing transitions from the $3d^n$ state to the final $2p^5 3d^{n+1}$ state with the $3d^{n+1} L^{-1}$ to $2p^5 3d^{n+2} L^{-1}$ transition with full charge transfer (where L^{-1} indicates a ligand hole), which are shown in figure 2.17. The ground state is separated from its charge transfer state by the charge transfer energy Δ_i . In the final state, additional terms have to be considered. The 2p core hole results in an attractive potential U_{pd} that influences the electrons in the final state. The electron that was excited from a 2p state into the 3d orbital induces a Coulomb repulsion U_{dd} with the other 3d electrons. The charge transfer separation in the final state is related to that of the ground state as $\Delta_f = \Delta_i + U_{dd} - U_{pd}$. The mixing strength between the states with and without charge transfer is assumed to be equal for the ground and final states, but not for e_g and t_{2g} states. With the inclusion of all the effects discussed in this section so far, the presented theory for describing the multi-electron transitions (in 3d transition metals) is known as charge-transfer multiplet theory (CTM).

When calculating XMCD spectra, an additional parameter in the form of an exchange field Δ_{exc} is required, which models the splitting of the spin states of different orientation because of inter-atomic exchange interactions in magnetic materials. A large exchange field results in a higher spin polarisation. Splitting caused by the exchange field is usually small enough to be bridged by thermal excitation [83]. The thermally occupied population of the higher levels is modelled with a Boltzmann distribution.

Charge transfer multiplet calculations are generally good at reproducing the spectra of materials with localised electrons, as is the case for transition metal oxides. However,

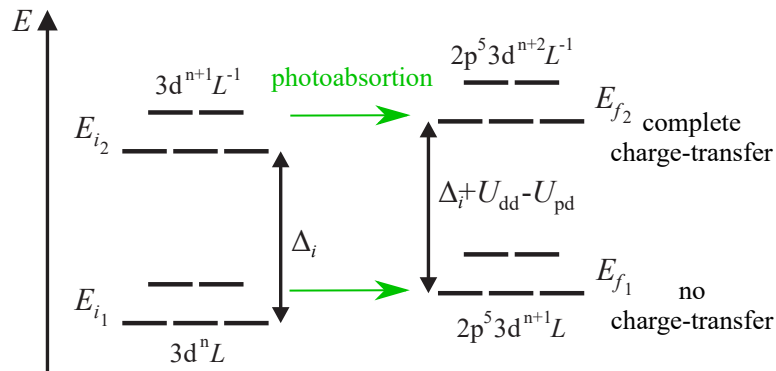


Figure 2.17: Principle of photoabsorption from 2p to 3d states, with (E_{i_2}, E_{f_2}) and without (E_{i_1}, E_{f_1}) full charge-transfer between ligand L and the transition metal cation. Δ_i is the charge-transfer energy of the ground state while U_{pd} and U_{dd} are potentials resulting from Coulomb interactions between the 2p core-hole and 3d electrons, and the 3d electrons themselves, respectively. Adapted from [19].

more delocalised systems such as metals are better described by density functional theory [78]. Additionally, the atomistic theory breaks down quickly at energies not close to the edges, as neither the background due to continuum transitions (which is usually modelled with broadened step functions) nor satellites more than a few eV above the edges are replicated. In theory, CTM calculations can be used to approximate photoelectron spectra as well, although the discrepancies between the calculations and measurements are typically even larger because the CTM model fails to account for the inelastic background and the more pronounced charge-transfer effects in XPS [84]. There are alternative models, such as the multiple scattering theory, which assumes single electron states but considers inelastic scattering at the atoms surrounding the absorber. This model is often used in EXAFS [71], as it describes the features far removed from the edges well, including background effects and satellites, but it fails to reproduce the edge structure, which in EXAFS is instead modelled with a simple step function [85]. In this work, only XANES measurements were performed and as such the CTM-theory is used to replicate the measured spectra.

2.6 Transmission electron microscopy

Transmission electron microscopy (TEM) is a direct imaging technique that provides information about the real space structure of the sample under investigation. Its principle of image formation is almost identical to an optical microscope while using electrons instead of photons and with the optical elements replaced by magnetic lenses [12, 86]. A condenser lens focusses the electron beam onto the sample. After passing through the sample, the beam is magnified and projected onto a screen by an array of lenses, the first and most important of which is the objective lens. An aperture at the back focal plane of the objective lens determines both the image contrast as well as the resolution limit of the microscope. The contrast arises from the aperture cutting off scattered

electrons, which lets regions of higher atomic density or with higher atomic number appear dark. In crystals, electrons can additionally be diffracted, as well as scattered. The interference of diffracted electrons creates a diffraction pattern at the objective aperture, which can be used to create different contrasts, using only the diffracted beam (dark-field imaging) or by cutting off the diffracted electrons, as is done with the scattered electrons, and using only the primary beam (bright-field imaging).

Similar to optical microscopes, the resolution can be approximated by the diffraction limit

$$\Delta = \frac{\lambda}{2 \sin \alpha}, \quad (2.65)$$

where λ is the electron wavelength and α is one-half of the angular aperture [12]. With electrons accelerated to over 100 keV, resolutions of the order of 1 Å are theoretically possible, but lens aberrations limit the effectively achievable resolution. A larger aperture enhances the resolution as seen in equation 2.65, but worsens the contrast as discussed above. Due to the short IMFP of electrons in solids, investigated films have to be thin, with maximal thicknesses in the order of 100 nm [12].

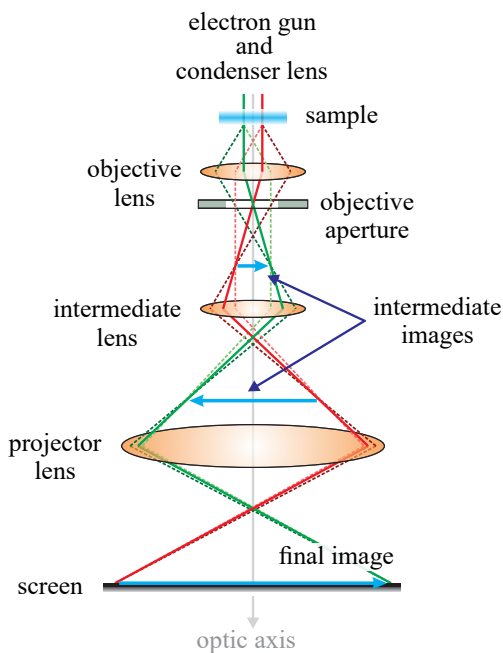


Figure 2.18: Schematic diagram of the image formation in a transmission electron microscope. The electron beam is collimated onto the sample and passes through it into a lens system and onto a screen, where it becomes visible. The objective aperture enables the operation in dark or bright field mode. The intermediate lens can consist of multiple lenses that serve to magnify the image. The dashed lines indicate the beam paths of scattered electrons. Adapted from [74, 87].

Scanning transmission electron microscopy (STEM) is a subtype of TEM measurement that differs from conventional TEM by the fact that only fine spots in the range of a few Å are imaged while the beam is scanned over the sample, in a similar way to techniques like AFM. Because of this rastered scanning process, STEM can be used for analytical techniques like energy dispersive X-ray spectroscopy (EDXS) and (high-angle) annular dark-field imaging (HAADF) [88].

EDXS is similar to XAS, in that the fluorescence of excited atoms is measured while the energy of the incident electrons is varied [89]. The elemental composition of the

spot under investigation in STEM can be determined via comparison of the energy-dependent intensity peak positions with predicted values from theory [90, 91].

In annular dark-field imaging, an annular detector is used to collect scattered as well as diffracted electrons, in contrast to conventional TEM. This results in a larger signal [88]. High-angle annular dark-field imaging measures specifically the electrons scattered at very high angles, both elastically and resulting from thermal diffuse scattering processes. This makes the technique more sensitive to variation in the atomic number of the probed atoms, since atoms with a higher atomic number scatter more electrons at high angles [88].

In general, the features seen in TEM measurements do not correspond directly to individual atoms. For this reason, quantitative information is difficult to acquire, e.g. by comparing numerical image simulations with the measured features [12].

3 | Relevant Materials

In this chapter the materials that are relevant in the experimental preparation and interpretation of measurements performed in this work are described.

3.1 Nickel(II)- and cobalt(II)-monoxide (NiO & CoO)

Cobalt(II)-monoxide (CoO) consists in equal parts of O^{2-} and Co^{2+} ions, crystallising in a rock-salt structure, as depicted in figure 3.1. Within this structure, Co^{2+} and O^{2-} ions each form separate face-centered cubic sublattices, which are shifted by half a lattice constant in the direction of a cubic lattice vector. This means that the Co^{2+} cations occupy the octahedral sites of the O^{2-} fcc sublattice and vice versa. The surface unit cell is rotated by 45° relative to the volume unit cell, with lattice constants that are smaller than the bulk values by a factor of $\sqrt{2}$. Nickel(II)-monoxide (NiO) can be described analogously to CoO. In NiO, the Co^{2+} ions are replaced by Ni^{2+} ions, while the structure remains the same. The lattice constants of CoO and NiO are $a_{CoO} = 4.260 \text{ \AA}$ and $a_{NiO} = 4.161 \text{ \AA}$ and $a_{CoO,s} = 3.012 \text{ \AA}$ and $a_{NiO,s} = 2.942 \text{ \AA}$ for the volume and surface unit cell, respectively. Both NiO and CoO are insulating antiferromagnets, with Néel temperatures of $T_{N,NiO} = 523 \text{ K}$ and $T_{N,CoO} = 293 \text{ K}$ and band gaps of $E_{G,NiO} = 4 \text{ eV}$ and $E_{G,CoO} = 2.5 \text{ eV}$ [92, 93, 94].

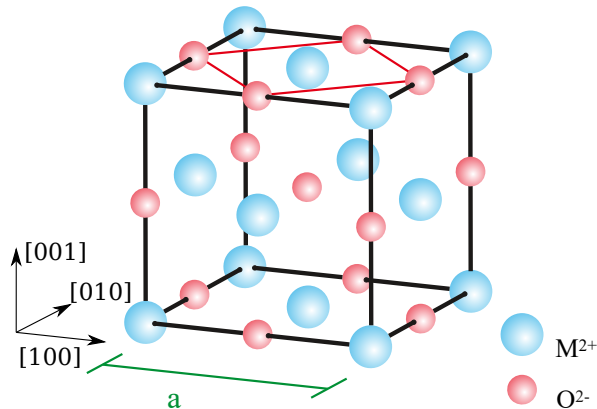


Figure 3.1: Volume and [001]-surface unit cells of the rock salt structure. M is representative of the metal cation, e.g. Ni or Co.

In their antiferromagnetic phase, both NiO and CoO are subject to distortions. CoO is distorted tetragonally [94], resulting in a reduction to monoclinic symmetry, whereas NiO is subject to rhombohedral distortion [95]. NiO is generally thought to consist of alternating antiferromagnetic (111)-planes, with the moments being oriented either parallel to the plane [95] or along the $\langle 211 \rangle$ directions [96]. However, in thin films or nanoparticles of NiO, this behaviour can vary drastically, especially when interactions with other materials are involved [97, 98, 99].

The magnetic structure of CoO was first described as being similar to NiO, with antiferromagnetic (111)-planes in which the moments are oriented in the $[\bar{1}\bar{1}7]$ -direction [95]. However, the exact nature of the magnetic structure in CoO is complex and has been a point of debate. Tomiyasu *et al.* [100] described CoO as consisting of two coexisting AFM phases of different ordering, with stacking occurring in the $[111]$ and in the tetragonal $[001]$ direction, with magnetic moments in the $[\bar{0}.325 \bar{0}.325 0.888]$ and $[1\bar{1}0]$ directions, respectively.

Due to their similarity in structure and properties, CoO and NiO can coexist in a single $(\text{Ni}_x\text{Co}_{1-x})\text{O}$ phase, with characteristics such as lattice constant and Néel temperature determined by the stoichiometry x [96].

3.2 Magnesium aluminium oxide (MgAl_2O_4)

Magnesium aluminium oxide (MgAl_2O_4), also known as spinel, crystallises in the face-centered cubic spinel structure $^T[A_{1-n} B_n] ^O[A_n B_{2-n}]O_4$ shown in figure 3.2, where T and O refer to occupied cation vacancies with tetrahedral and octahedral coordination, respectively, and $0 \leq n \leq 1$ denotes the degree of inversion, with $n = 0$ and $n = 1$ describing a normal and an inverse spinel, respectively.

In the spinel structure, 32 O^{2-} anions form the unit cell of an fcc-sublattice, which contains octahedral and tetrahedral vacancies. One half of the 32 octahedral vacancies and one eighth of the 64 tetrahedral vacancies are occupied at random by cations A and B in variable combinations of formal charge [101]. This means that the cubic unit cell contains eight formula units of AB_2O_4 . The surface unit cells in spinels behave identically to those in rock salts, in relation to the bulk structure.

MgAl_2O_4 ideally crystallises as a normal spinel, with Mg^{2+} cations occupying the tetrahedral and Al^{3+} occupying the octahedral sites, although in practice, deviations from this distribution are possible [102]. MgAl_2O_4 is stable below temperatures of about 1200°C , where it decomposes into MgO and Al_2O_3 [103]. It is a semiconductor with a band gap of 7.8 eV and a metal-semiconductor-transition at around 115°C [104]. MgAl_2O_4 is said to be either paramagnetic, antiferromagnetic with a Néel temperature below 195°C [105], or diamagnetic [102]. The reported lattice parameter a_0 of MgAl_2O_4 varies from 8 Å to 8.4 Å [102, 104].

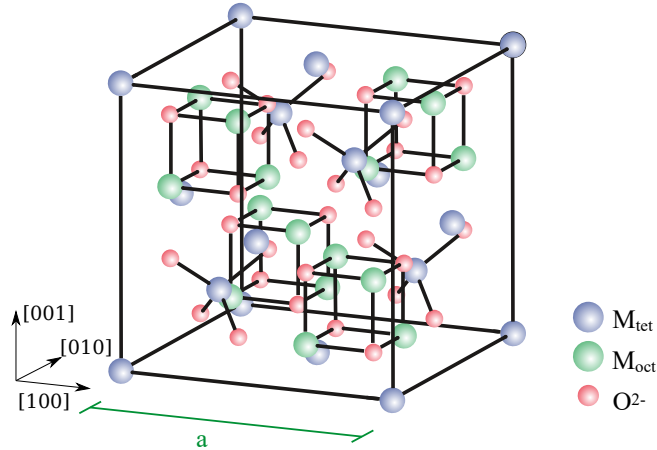


Figure 3.2: Volume unit cell of the spinel structure. Metal cations are distributed across 16 of the 32 O_h vacancies and across 8 of the 64 T_d vacancies, where the occupied vacancies are chosen randomly. The type of cation on each site depends on the material and details of the deposition method used.

3.3 Nickel cobaltite (NiCo_2O_4)

Nickel cobaltite (NiCo_2O_4) is commonly described as crystallising in the inverse spinel structure discussed above. The ionic distribution, as well as the resulting structural, electric and magnetic properties, heavily depend on the stoichiometry and the method of creation [8]. As such, nickel cobaltite can vary from being a metallic ferrimagnet with transition temperatures between 300 K and 400 K [1, 4] to being a non-magnetic insulator [3, 4] with reported lattice constants between 8.11 Å and 8.185 Å [1, 4, 2].

The magnetic behaviour of (inverse) transition metal oxide spinels can generally be expected to bear similarities to magnetite. In magnetite, there are three main components that determine the net magnetic moment [106]. The strongest interaction is the super exchange between the M^{3+} cations at tetrahedral and octahedral sites. The Goodenough-Kanamori rules predict such an interaction due to the overlap angle of M 3d and O 2p orbitals of $\approx 125^\circ$. Additionally, there is a ferromagnetic super exchange interaction between cations of the same valencies at both T and O sites, as well as a double exchange interaction between the M^{3+} and M^{2+} cations at the O sites (and at the T sites in case of non-ideal cation valencies). Further interactions are thought to be small enough to be negligible. Whether this arrangement results in ferrimagnetic or antiferromagnetic behaviour depends on the transition metals, their valencies and their spin states.

The ideal inverse nickel cobaltite spinel with a mixed-valence cation distribution of the form $T[\text{Co}_y^{2+}\text{Co}_{1-y}^{3+}]_O[\text{Co}^{3+}\text{Ni}_{1-y}^{2+}\text{Ni}_y^{3+}]\text{O}_4^{2-}$ is expected to have a spin magnetic moment per unit cell of $2\mu_B$ regardless of y , if the tetrahedrally coordinated cations are assumed to be in high spin states and the octahedrally coordinated cations in low spin states [4]. If $y = 0$, the net spin magnetisation of $2\mu_B/\text{f.u.}$ does not depend on the spin state of Co^{3+} , as the Co^{3+} cations on both sites fully compensate each other. The

fully inverted spinel structure is only an idealisation, and films with a lower degree of inversion can be found in literature [107]. Additionally, ferrimagnetic, metallic nickel cobaltite films tend to exhibit a mixed-valence structure with a large amount of $\text{Ni}_{\text{Oct}}^{3+}$, while structures close to $y = 0$ tend to result in non-magnetic insulators [4, 108, 109].

4 | Experimental Setup and Sample Preparation

In this work, multiple samples of $\text{Ni}_x\text{Co}_{3-x}\text{O}_4$ on $\text{MgAl}_2\text{O}_4(001)$ were prepared at different epitaxy temperatures using an oxygen-plasma assisted RMBE technique under UHV conditions. Subsequently, measurements involving LEED (4.2), XPS (4.3), XRR (4.4), SQUID magnetometry (4.5), XAS (4.6) and TEM (4.7) were performed on them. In this chapter, the setups used to prepare the samples and to perform each experiment are presented, as well as the respective experimental conditions and, if applicable, the steps performed to process the data.

4.1 Sample preparation in an ultra-high vacuum system

In order to produce samples of reasonably high purity and to detect the photoelectrons and diffracted electrons used to characterise them, an ultra high vacuum is required, so that sample contamination by adsorbants is minimised and the inelastic free mean path of electrons freed from the sample surface is large enough for them to reach the detectors.

The vacuum chamber system used for sample preparation and *in situ* measurement of LEED and XPS is depicted in figure 4.1. It consists of three chambers and an airlock, separated by valves, with a common rotary vane pump connected to all chambers and separate turbomolecular pumps for each chamber. The chambers used for sample preparation and measurement of XPS and LEED additionally include ion getter pumps, which can lower the pressure down to the order of 1×10^{-10} mbar.

Chambers one and two include inlets for molecular oxygen as well as heating elements, which consist of heating filaments and a high voltage acceleration cathode aimed at the sample holder. Each heating element is coupled to a thermal sensor in order to keep the temperature at the desired level. Chamber two additionally includes two effusion cells at roughly equal distances and at similar angles relative to the sample holder for the epitaxy of nickel and cobalt, respectively. The effusion cells contain a solid target of the given metal, which can be heated by electrons emitted from a heating filament that are accelerated onto the target by an applied high voltage. At high

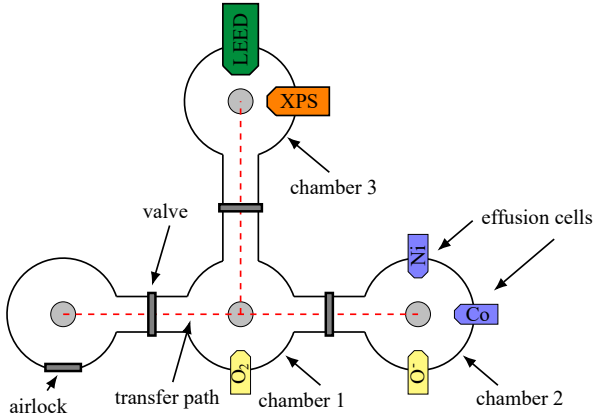


Figure 4.1: Schematic overview of the UHV setup used for sample preparation and *in situ* characterisation via XPS and LEED. The sample is introduced into the setup through the airlock and is moved from chamber to chamber along the transfer path. The samples are first cleaned via heat treatment in chamber one, after which the epitaxy process is performed using the effusion cells and the oxygen plasma source in chamber two. The subsequent analysis takes place in chamber three. At each step, the sample is placed on a central sample holder inside each chamber. Adapted from [110].

enough temperatures, metal atoms leave the target as a gas and can be focussed onto the substrate through a controllable shutter. The evaporation rate can be monitored using a flux meter close to the shutter. For the epitaxy of $\text{Ni}_x\text{Co}_{3-x}\text{O}_4$, it is beneficial to work under an atomic oxygen atmosphere because of its higher reactivity compared to molecular oxygen, which is why chamber two contains a plasma source. Chamber three contains the XPS and LEED devices used for *in situ* characterisation. The vacuum quality necessary for measurements is ensured by a titanium sublimator, along with the previously mentioned pump system.

The $\text{Ni}_x\text{Co}_{3-x}\text{O}_4$ films were grown on $\text{MgAl}_2\text{O}_4(001)$ substrates provided by CrysTec GmbH with a surface orientation tolerance $< 0.005^\circ$ guaranteed by the manufacturer. The substrates were mounted on sample holders and heated in chamber 1 at a temperature of 400°C and at a molecular oxygen partial pressure of 1×10^{-4} mbar for one hour. The oxygen was included in order to prevent the formation of oxygen vacancies in the substrate surface and to aid the desorption process of the adsorbants, which are expected to mostly consist of carbon oxides. The cleaned substrates were then investigated via XPS and LEED to confirm whether the cleaning process was successful.

The reactive molecular beam epitaxy process was performed in chamber 2. The substrates were heated to temperatures of 250°C , 300°C , 400°C , 500°C and 620°C , respectively, under an atomic oxygen partial pressure of 5×10^{-6} mbar. In order to facilitate these conditions, the acceleration voltage of the sample heating filament was set to 1 kV and the plasma cracker source was powered at a current of 50 mA. Both the plasma source as well as the effusion cells were powered until they were stable before the epitaxy process was started. For all samples, the epitaxy length was 4000 s and the effusion cell fluxes were set to a ratio that was expected to yield nearly stoichiometric NiCo_2O_4 according to earlier film thickness calibrations performed by means of XRR measurements. At the end of the epitaxy process, the heating filament current was turned off, and subsequently the plasma source as well as the oxygen intake were

shut off only after the sample had cooled to 120 °C, in order to prevent the transformation of the films into a rock-salt at high temperatures, which had seemingly been observed in earlier experiments. The grown films were then characterised *ex situ* with the above-mentioned array of measurements.

4.1.1 Plasma source

In order to produce an atomic oxygen atmosphere, a plasma cracker source of the model *PCS-ECR* manufactured by SPECS was used.

A plasma is a quasi-neutral gas consisting of ions and free electrons. It can be fully or partially ionised and is defined by strong shielding effects in the vicinity of local charges, a dominance of bulk effects over boundary effects and plasmon frequencies that are larger than the collision frequency of electrons with neutral particles. More information on the characteristics and creation of plasmas can be found in [111, 112].

The plasma source used in this work utilises a microwave generator to produce a radially symmetric 2.45 GHz microwave field that ionises the molecular oxygen that is vented into the plasma source chamber. A multi-polar magnet array is powered at 86 mT to enable the utilisation of electron cyclotron resonance (ECR) by coupling the microwave field to the cyclotron frequency of the electrons in the magnetic field of the array [113]. The electrons that gain kinetic energy through the resonance process can in turn ionise additional oxygen molecules, thus stabilising the plasma.

The microwave generator was powered at about 250 W with an oxygen partial pressure of about 5×10^{-6} mbar and the source was used as an atomic source, with particle energies below 1 eV.

4.2 Low-energy electron diffraction setup

The experimental setup used for LEED measurements is an *ErLEED 150* by SPECS. The setup is depicted schematically in figure 4.2 and due to technical difficulties the measurements took place *ex situ*, except for a reference measurement of the bare substrate. Electrons are emitted from a cathode at an acceleration voltage $-V$ and a current of about 2.25 A, and are accelerated to varying energies up to 1 keV using a combination of an anode and a Wehnelt cylinder to narrow the beam, after which they pass through a lens system, which collimates the electrons onto the sample, where they are diffracted. The electrons have to pass through three concentric grids before reaching the screen. The first grid, along with the last lens system component and the sample itself, is at ground potential, so that the electrons propagate in a field-free space until they reach the first hemispherical grid after being scattered at the sample surface. This is done in order to prevent distortions resulting from possible electric fields diverting the electrons from their straight scattering paths. The second grid is at a slightly positive potential relative to the cathode (referred to as the suppression voltage) and serves to

decelerate the electrons so that inelastically scattered electrons are less likely to reach the screen, consequently improving the signal-to-noise ratio. The third grid is again at ground potential and screens the second grid from the potential of the fluorescence screen at about 6 kV. The screen potential re-accelerates the electrons that passed the grids. At contact with the screen the electrons cause fluorescence, which - together with a camera behind the screen - makes the diffraction pattern of the electrons in reciprocal space directly visible. The camera is situated behind the emitting cathode, making the (00) reflex invisible in this setup.

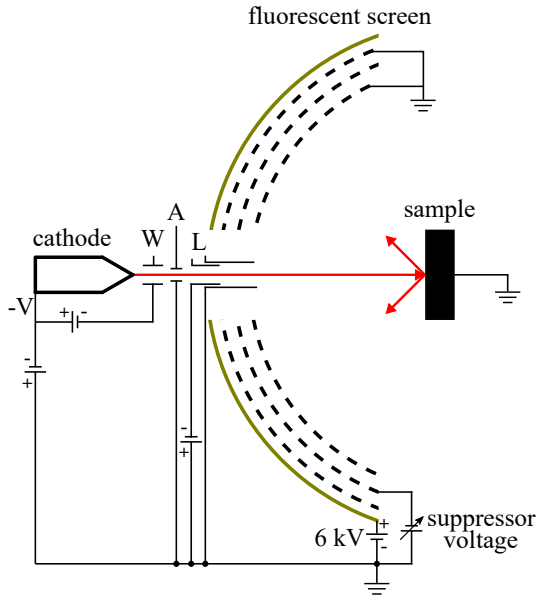


Figure 4.2: Schematic of the LEED system, consisting of a cathode at acceleration voltage $-V$, an anode (A) and Wehnelt cylinder (W) that control the electron emission, lenses (L) for collimation of the electron beam onto the sample, and a multi-grid system that serves to suppress inelastically scattered electrons before they reach the fluorescent screen, where the diffracted electrons make the reciprocal sample structure directly visible. Adapted from [12].

LEED measurements for all samples were performed in an energy range of 90 eV to 300 eV, both before and after the epitaxy process. The lens parameters of the setup were optimised for maximal clarity of the camera picture for each individual measurement.

4.3 X-ray photoelectron spectrometer

For XPS measurements a *Phoibos HSA 150*-setup by SPECS was used. It includes a non-monochromatic X-ray source, a detection system consisting of a hemispherical analyser and multiple channeltrons as detector, as well as a lens system for focussing the photoelectrons from the sample into the analyser. A schematic representation of the setup is depicted in figure 4.3.

The X-ray source emits photons with one of two distinct energies dictated by the employed anode material, which can either be Mg or Al. The Mg (Al) anode primarily emits photons with an energy of the $K_{\alpha 1,2}$ line of 1253.6 eV (1486.6 eV), although, additionally, photons with an energy shift of 8.4 eV (9.8 eV) and 10.1 eV (11.8 eV) toward higher energies have to be considered to account for the lines from the $K_{\alpha 3}$ and

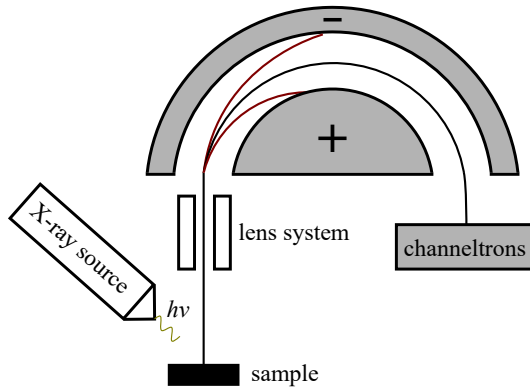


Figure 4.3: Schematic of the XPS setup, consisting of an X-ray source directed at the sample, electron optics used to focus and decelerate the photoelectrons into a hemispheric analyser, and a detector consisting of multiple channeltrons. Two electrodes inside the analyser force the electrons onto curved paths that end in the channeltrons only if the kinetic energy of the electrons matches E_{pass} . Adapted from [110].

$K_{\alpha 4}$ transitions, which have intensities of 8% (6.4%) and 4.1% (3.2%) relative to the main line, respectively. Additional contributions are usually negligible.

The photons emit photoelectrons from the sample surface, which are then focussed into the hemispheric analyser by the lens system. The analyser consists of two concentric electrodes with a potential difference between them. At a constant potential, only electrons in a specific range of kinetic energy reach the channeltron detectors at the end of the analyser, because the radius of the electron path inside the analyser depends on both the kinetic energy of the electrons as well as the electrode potential. In the used setup, the kinetic energy of the electrons is tuned to a constant pass energy by decelerating and accelerating the electrons via the lens system, so that the spectral resolution remains constant over the whole energy range of the spectrum. This is known as fixed analyser-transmission mode. A higher pass energy results in a lower spectral resolution but a better signal-to-noise ratio. This is because the energy resolution of the hemispheric analyser is relative to the kinetic energy of the electrons and as such the absolute energy differences between the electrons entering the different channeltrons scale with the pass energy.

XP-spectra were measured for all samples, both before and after the epitaxy process. Multiple spectra were measured for each sample: first, a survey scan was performed over the whole spectrum, to ascertain whether the general peak structure matches the expected elemental composition. After that, individual spectra were taken in the vicinity of the Co 2p, Ni 2p, and O 1s peaks. Due to technical difficulties, all spectra had to be re-measured *ex situ*, which is why additional C 1s spectra were taken to account for adsorbate effects. Additionally, the valence bands as well as the Co/Ni 3p peaks of the grown films were measured *ex situ* with a different setup, which includes monochromatic Al-source as well as a dual-beam neutralisation system [60] for (partial) compensation of surface charge effects. All measurements were taken with a pass energy close to $E_{\text{pass}} = 50 \text{ eV}$.

Curve fits of XP-spectra were generally performed by first subtracting a Shirley-background from the range of peaks under investigation and consequently fitting pseudo-Voigt composite functions according to literature values for the material. For all peaks, FWHMs of up to 4 eV were allowed, as well as a deviation from literature peak posi-

tions of up to ± 0.5 eV for the main peaks and up to ± 1 eV for the satellites. The fraction of Lorentzian to Gaussian contribution was restricted to the range of 0.2 - 0.5.

4.4 X-ray reflectrometer

In order to analyse the sample film thickness, an XRR setup with an X-ray diffractometer of the model *X'Pert³ MRD* by Malvern Panalytical is used. The $K_{\alpha 1}$ line of a copper anode at an energy of 8048 keV was used as an X-ray source.

XRR measurements were performed in an air atmosphere in the $\theta/2\theta$ geometry, in which the X-ray beam strikes the sample at an angle θ_i relative to the sample surface plane, while the detector is kept at an angle $2\theta_i$ relative to the X-ray source beam. The incidence angle θ_i is varied at low values, in order to gather the film thickness from the resulting Kiessig-fringes as described in chapter 2.3.

The measured XRR data were fit using the software package *Reflex* [24] according to the optical matrix method by Abelès [23]. The free parameters were the film thickness d and the surface roughness σ , as well as the substrate roughness, while the other substrate parameters as well as values for δ and β of nickel cobaltite from literature [114] were input as fixed parameters, although a tolerance of about 10 % was used for the latter, in order to account for deviations from the spinel structure.

4.5 SQUID-setup

In order to characterise the magnetic properties of the samples, a superconducting quantum interference device is used. The setup used for this work is an *S700X*, manufactured by Cryogenic Ltd., the schematics of which are presented in figure 4.4.

A liquid helium reservoir is used to cool both the sample to be measured as well as the superconducting magnet, which makes it possible to achieve temperatures as low as 1.6 K at the sample position. A reservoir of liquid nitrogen prevents the helium from vaporising too quickly. The helium can be heated up to about 400 K via two heating elements and the heated helium gas can be vented into the variable temperature insert (VTI), where the sample is affixed to a hollow kapton cylinder. The VTI is enclosed by the magnet and contains a superconducting pick-up coil, which is coupled to the SQUID itself via a flux transformer. The magnet can provide fields with a strength of up to 7 T along the vertical axis of the VTI, which lies parallel to the sample surface. A linear motor moves the sample up and down inside the VTI, which results in magnetic flux variations that induce a current in the pick-up coil. This current is proportional to the absolute change in magnetic flux instead of the rate of change, because the pick-up coil is superconducting. The current induced in the pick-up coil is transformed into a voltage output by the DC-SQUID. The proportionality to the change in magnetic flux remains, so the voltage can be measured as a function of the vertical sample position

inside the coil. An electrical feedback system keeps the SQUID working point near the voltage maxima, so the measured voltage depends nearly linearly on the flux applied to the system. The magnetic moment μ of the sample can then be obtained by fitting the voltage-position signal with the expected curve from an ideal point dipole positioned on the axis of movement [115, 116]. The calibration, measurement and data acquisition are controlled via a software package provided by the manufacturer.

In theory, the magnetic flux resulting from the sample magnetisation could be measured without moving the sample. However, the linear movement of the sample makes it possible to subtract the time-dependent background drift introduced by e.g. the remnant field of the magnet and metal components of the VTI [116].

The setup of flux transformer and pick-up coil has several advantages compared to placing the SQUID device directly around the VTI. First, this setup allows the SQUID itself to be placed in a less noisy and more stable environment than the pick-up coil itself. Second, the pick-up coil constitutes a second-order gradiometer. It contains two clockwise central loops and one counter-clockwise loop on either side. This design serves to cancel out gradients or magnetic drift of the externally applied fields.

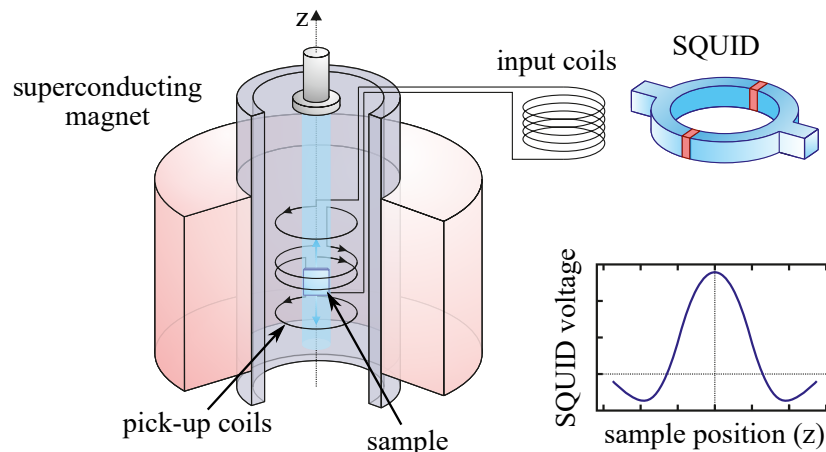


Figure 4.4: Schematic of the main parts of the SQUID magnetometer. The sample is mounted inside a kapton straw and is placed in a variable temperature insert (VTI), surrounded by flux pick-up coils as well as a superconducting solenoid magnet. The temperature is controlled by venting pre-heated gaseous helium into the chamber from the liquid helium reservoir surrounding the VTI and the magnet (not pictured). The sample magnetic moment is measured by moving the sample along the vertical z -axis, which induces a current in the pick-up coil that gets transformed into a voltage in the SQUID that is coupled to the pick-up coils via an input coil. The SQUID voltage is measured while varying the vertical sample position and the sample magnetic moment is extracted via curve fitting. The working point of the SQUID is kept constant using an electronic feedback system. Adapted from [74].

For all samples, field cooling (FC) and zero field cooling (ZFC) curves were measured. First, the samples were heated up to 350 K and kept there for a few minutes with no applied field, in order to dissipate any magnetisation that may have been introduced while loading the samples into the device. Then, the samples were cooled to 5 K,

at which point a constant field of 0.1 T was applied. The magnetisation was then measured, while the temperature was increased stepwise up to 300 K. This is the ZFC curve. Afterwards, the samples were cooled down to 5 K again, this time with the applied field, and then the temperature curve was measured again, resulting in the FC curve. Additionally, magnetisation curves were taken for all samples at multiple temperatures. The samples were again heated to 350 K before a temperature of 5 K, 80 K or 300 K was set and the magnetisation was measured while varying the field strength in the full available range from -7 T to 7 T.

4.5.1 Data processing

The raw magnetisations contain background signals that have to be taken into consideration, because the samples consist of the thin films of interest as well as the substrates. In both the ZFC/FC curves as well as the magnetisation curves, the background of the bare substrate and the background of the sample holder were subtracted as follows: first, the sample holder in isolation and a substrate affixed to the sample holder were measured. Then, the measurement of the sample holder was subtracted from the measurement of the substrate in order to isolate both signals. In the final measurements of the samples, the previously isolated signal of the bare substrate was scaled to the size of the sample in question and subtracted, together with the signal of the sample holder. In doing this, it was assumed that the substrate and sample holder would contribute similar backgrounds for all samples. In case of the magnetisation curves, additional background corrections were applied. A linear background was fitted to the saturated high-field regions and subtracted in order to account for a remaining diamagnetic response of the films. The diamagnetic contributions of the sample holder and substrate should ideally have been subtracted in the earlier step. The magnetisation curves were further corrected for an offset from the center and a temperature drift, although the offset was deemed negligible in all measurements. For the temperature drift, a positive field correction of the form

$$M_{\text{corr}}^+(\text{H}) = M^+(\text{H}) - \text{err}(\text{H}), M_{\text{corr}}^- = M^-(\text{H}) - \text{err}(-\text{H}), \text{H} > 0 \quad (4.1)$$

was applied, where M^\pm refers to the upper and lower branch of the hysteresis, respectively and $\text{err}(\text{H}) = M^+(\text{H}) - M^-(-\text{H})$. Parameters such as the saturation magnetisation and coercivity were extracted by curve fitting the magnetisation curves using an array of generalised sigmoid logistic functions [117], to minimise the effect of noise on the parameters. Further details on the corrections and fitting process can be found in [118, 119].

4.6 XAS & XMCD

The XAS and XMCD measurements in this work were performed externally at the Advanced Light Source (ALS) at the Lawrence Berkeley National Laboratory in Berkeley,

USA, using beamline 4.0.2. Synchrotron radiation is required to perform XAS experiments due to its unique ability to supply high beam intensities of continuously tunable photon energies, in contrast to the discrete energies supplied by conventional laboratory X-ray sources. For information about the generation of (polarised) synchrotron radiation, refer to [20, 62].

The experimental setup consists of a sample stage, which can be rotated to change the incidence angle θ to the incoming X-ray beam, as well as a superconducting vector magnet that produces a field parallel to the sample surface. The sample is additionally connected to ground by a conductive wire and silver paste, in order to enable the measurement of the TEY signal via the neutralisation current passing through the wire during the absorption process. The setup, which is presented schematically in figure 4.5, is placed in an ultra-high vacuum chamber.

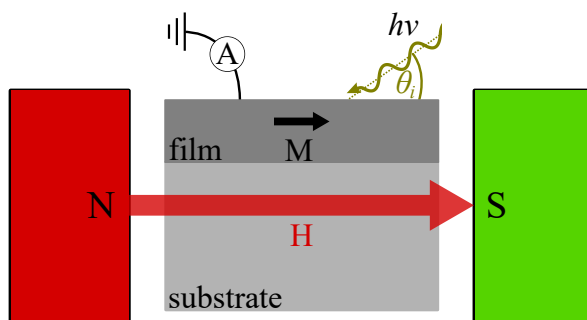


Figure 4.5: Experimental setup used for XAS & XMCD experiments. The sample is placed at the center of a magnetic field (indicated by the red arrow) that is parallel to the sample surface. The film is illuminated by circularly polarised X-rays at an angle of θ_i relative to the surface. The absorption coefficient is indirectly measured via the neutralisation current flowing from ground to the film when absorption processes take place. Adapted from [81].

Measurements of all samples were performed at room temperature in TEY mode at a photon incidence angle of 30° . The two polarisation spectra were taken by reversing the magnetic field direction and consequently the sample magnetisation between measurements, which is equivalent to switching the photon polarisation [62]. A magnetic field of 3.6 T was applied and the photon energy was varied with a step size of 0.05 eV. The degree of circular photon polarisation was 90%.

4.6.1 Processing of absorption data

The measured data were processed before CTM curve fits were performed. For each spectrum, eight measurements under identical conditions were averaged and the spectra were normalised to the incidence intensity I_0 in arbitrary units, to account for fluctuations in the incident beam. Additionally, the spectra were normalised to the intensity I_c in the nearly constant region below the L_3 peak. The XAS and MCD signals were produced by summing and subtracting the spectra with opposite applied magnetic fields, respectively. Since the CTM calculations do not account for the continuum background, step functions that serve to model continuum transitions were subtracted from the spectra [77]. The square step functions were placed in the maxima of the $L_{2,3}$ peaks and were convoluted with a Lorentzian function with a full width at half-maximum of

0.4 eV. In the nickel spectra, an additional step was subtracted just below the L_2 peak [50]. After this process, the spectra were quantitatively evaluated using the software package FMD. It is based on CTM4XAS [120], which utilises Cowan code [121] to calculate CTM spectra for di- and trivalent Ni, Co and Fe. Using FMD, the XAS and MCD spectra are fit simultaneously, using the CTM parameters described in section 2.5.6, which include charge-transfer energies for ground and final states, crystal field splitting values and exchange splitting with additional Gaussian and Lorentzian broadening parameters for the experimental and core-hole lifetime broadening, respectively. More information on FMD and the fitting parameters can be found in [81].

4.7 TEM

As mentioned in section 2.6, the electron beams used in TEM have maximum penetration depths in the order of multiple hundred nm. If samples are thicker, or if cross-sections are analysed, they need to be cut into pieces of suitable thickness. For the sample investigated in this work, a cross-section preparation method [122] similar to that presented in figure 4.6 was utilised. Using this method, the samples are sliced into thin pieces normal to the film surface, which are then glued together film-to-film using epoxy glue. The resulting multi-layered blocks are cut again and a slice is adhered to a metal (e.g. Ti) ring for stability, although cylindrical tubes are often used as well. A certain area of the slice is then thinned until it is electron transparent, first by dimple-grinding and finally by ion-milling. The TEM images are then taken inside the ion-milled area containing the interface between substrate and film.

Cross-section measurements were performed externally on the 250 °C-film at the Technische Universität Dresden, using conventional TEM as well as HAADF-STEM with EDXS.

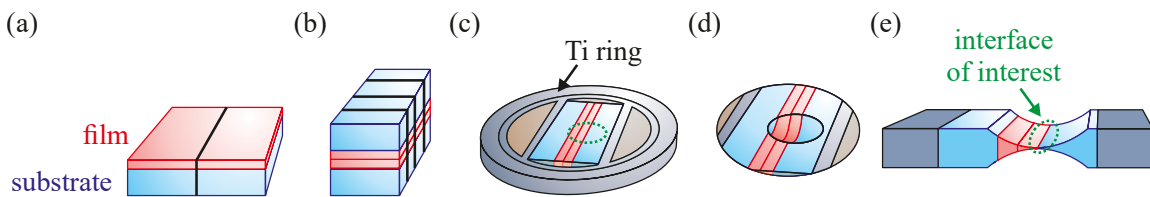


Figure 4.6: Cross-section preparation method used in TEM measurements. (a) First, the sample is cut into slices and (b) these slices are glued together face-to-face. A thin piece of this 'sandwich' is cut off and (c) embedded in a titanium ring holder or a cylindrical tube. (d) An area containing the interface between the substrate and the sample is then thinned by dimple-grinding and ion-milling until it becomes electron transparent. (e) The thinned interface area can then be investigated using various TEM modes. Taken from [74].

5 | Results and Discussion

In this chapter, the results of the experiments detailed in chapter 4 are presented and discussed. First, the general structure and thickness of the films are evaluated using LEED and XRR. The film composition is then investigated using the results of XPS, TEM and XAS measurements. Finally, the magnetic properties of the films are discussed in the context of the previous measurements.

5.1 LEED

Exemplary results of the LEED measurements, performed at an energy of 117 eV, are presented in figure 5.1. In addition to the samples prepared for the temperature series, one example of a substrate measurement is shown for reference. In the substrate measurement, the (1×1) pattern of the quadratic $\text{MgAl}_2\text{O}_4(001)$ surface structure is visible with sharp diffraction spots indicating a high crystallinity, which is to be expected for the substrates. The subsequent images show the films grown on the MgAl_2O_4 substrates to have a similar surface structure, as the diffraction spots are found at almost identical positions. This is indicative of the films exhibiting a spinel structure with a low lattice mismatch to the substrate. This observation is consistent with the presence of $\text{Ni}_x\text{Co}_{3-x}\text{O}_4$ in the surface layers of the films, which is expected to have a lattice mismatch with MgAl_2O_4 in the range of 0.4 % to 1.3 % [4, 1, 104]. There are no obvious differences between the diffraction patterns of the different samples.

From figure 5.1 it appears that the diffraction peaks of the epitaxial films are wider and less intensive than those of the bare substrate. In order to compare the peak quality of the samples, intensity profiles of the (12) and (21) peak were taken, fitted with a Lorentzian curve after a linear background was subtracted (as is depicted in figure 5.2(a)), and averaged. The full widths at half maximum (FWHMs) of the grown films are larger than those of the bare substrates (not shown) by roughly a factor of two. This, along with the lower intensities, indicates that the grown films contain more lattice defects and consist of smaller crystallites than the substrates. In figure 5.2(b), the FWHMs of all films are depicted. It is apparent that all films are very similar in their crystalline properties, with FWHMs of about 42 %BZ. Only the 620 °C-sample shows diffraction peaks with somewhat smaller FWHMs at 36 %BZ, which suggests a structure with larger crystallite grains and potentially with less crystal defects.

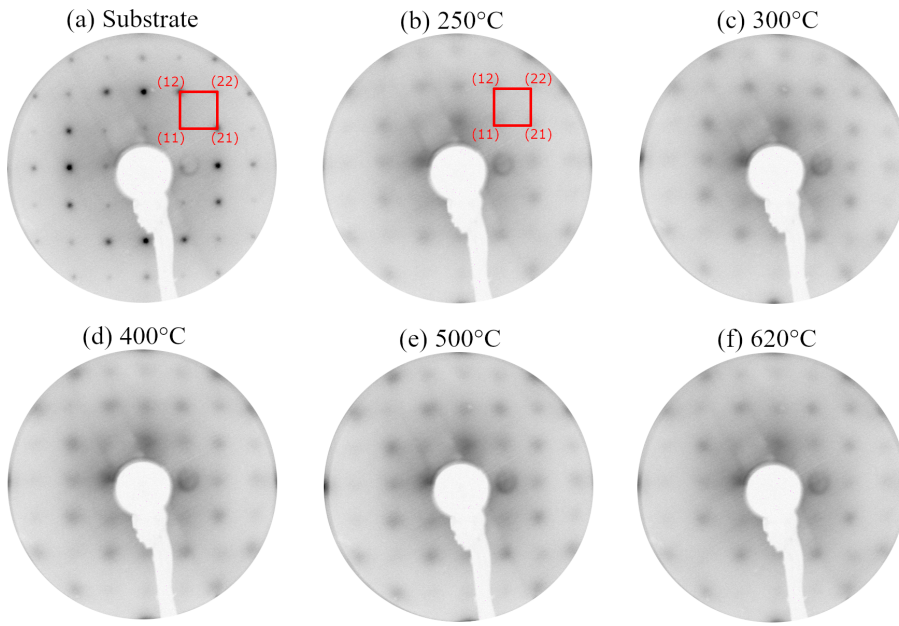


Figure 5.1: LEED diffraction patterns of (a) an MgAl_2O_4 substrate and (b) - (f) the nickel cobaltite films grown at epitaxy temperatures of 250 °C, 300 °C, 400 °C, 500 °C and 620 °C. A (1×1) surface unit cell of both the substrate and the films is indicated along with its diffraction spots.

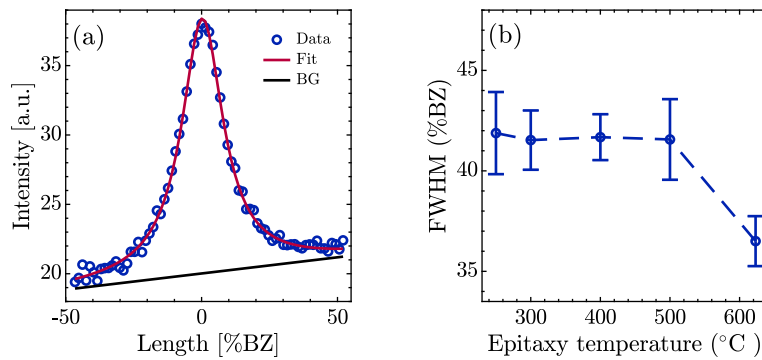


Figure 5.2: (a) Intensity profile cross-section of a (21) diffraction peak. A linear background(black) is subtracted before a lorentzian curve(red) is fitted to the data(blue). (b) FWHMs of the grown films in terms of the Brillouin zone of the substrate.

5.2 XRR

The film thicknesses as well as their roughness parameters were determined via curve fitting of XRR measurements taken in the $\theta/2\theta$ -geometry according to section 4.4. The resulting reflectivity curves as well as the fits used in their analysis are depicted in figure 5.3.

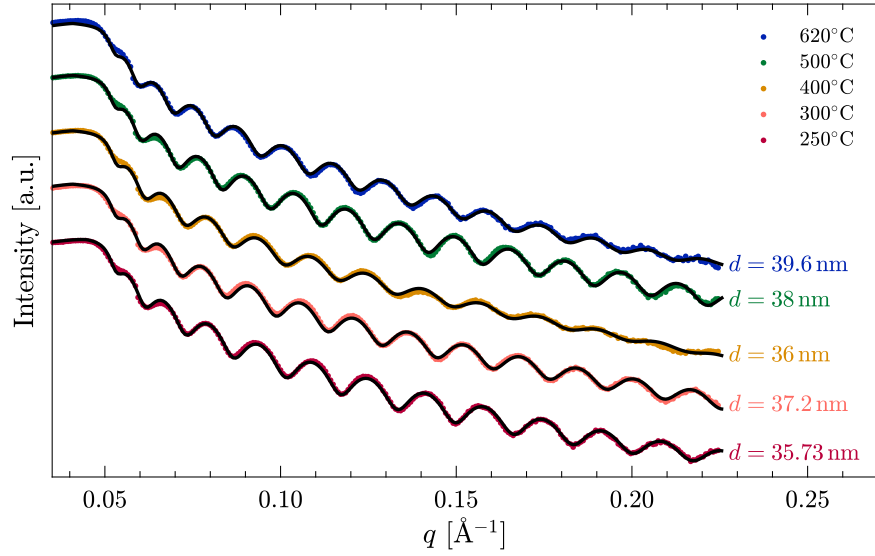


Figure 5.3: XRR measurements of the prepared films grown at different temperatures (coloured), along with their respective fits (black). The film thicknesses resulting from the fits are included next to the curves.

All samples exhibit regular Kiessig-Fringes as they are expected from a system with a uniform single layer film on top of the substrate. The fit model was adjusted accordingly and literature values [114] for the optical parameters of NiCo_2O_4 and MgAl_2O_4 were used for the film and the substrate, respectively. A deviation of about 10 % was allowed for the optical constants of the film. The calculated curves fit the sample data well, except for some outliers at low angles near q_c and at high angles for the rougher samples. The film thickness values resulting from the fitting process are included in figure 5.3, while the surface and interface roughness values are depicted in figure 5.4.

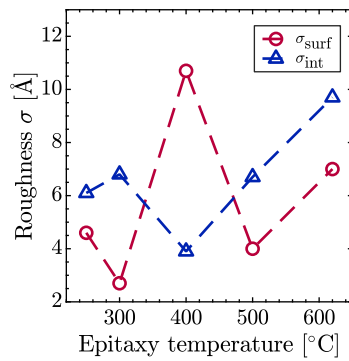


Figure 5.4: Roughness values of the substrate-film interfaces and the surfaces of the grown films resulting from the curve fits.

The samples have similar thicknesses, clustering around 37.67 ± 1.94 nm. The pronounced drop in oscillation amplitudes with rising angle indicates that the films grown at 620 °C and 400 °C are notably rougher than their counterparts. The roughness parameters resulting from the fit, shown in figure 5.4, seem to confirm this observation,

although no obvious trend depending on the epitaxy temperature emerges. It should be noted that the roughness parameters returned by the fit are highly interdependent with other fixed and variable parameters, which makes them volatile during the fitting process. As such, they should be interpreted as rough estimates only. In contrast, the thickness exclusively depends on the difference Δq between fringe maxima, which should result in reasonable values as long as the general form of the intensity curve is reproduced adequately.

5.3 XPS

The elemental composition of all samples was investigated via analysis of XP-spectra. An exemplary survey spectrum of one of the samples, measured *in situ* with an Mg anode, is depicted in figure 5.5. The most intense peaks expected from a material containing Co, Ni and O are all present and marked in the figure. No trace of the substrate material could be identified in any of the spectra.

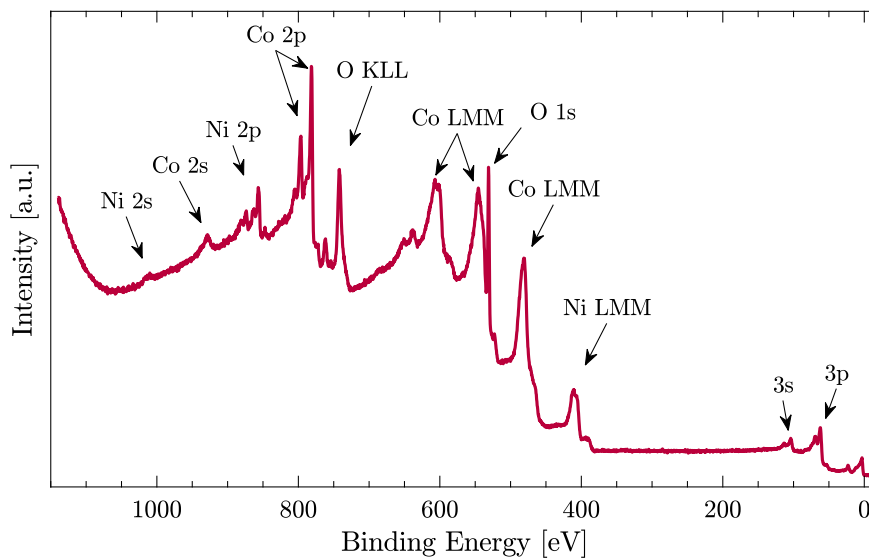


Figure 5.5: Survey spectrum of the 300 °C-sample, taken with an Mg source with $E_{\text{ph}} = 1253.6$ eV. The signals of photoelectrons emitted from core orbitals as well as Auger electrons are visible. Parts of the Co LMM and Ni LMM peaks overlap, as well as the Co 2p peaks and O KLL peaks. In addition to the marked transitions, the O 2s peak as well as the valence band excitations are visible at low binding energies.

Spectra of the 2p and 3p orbitals of Co and Ni as well as the valence band spectra were remeasured more accurately in order to gain information about the coordination and oxidation state of the metal cations as well as their stoichiometry. The rest of this section focuses on the analysis of these spectra.

5.3.1 2p spectra

The 2p spectra of Co and Ni contain characteristic features that enable the qualitative determination of the dominant oxide species by comparison with reference spectra of known materials. The sample 2p spectra were measured using an Mg-source, after the samples were exposed to air. In order to correct for a shift in the apparent binding energies due to charge buildup at the sample surfaces, the spectra were shifted so that the O 1s peak is positioned at 529.5 eV, as roughly expected from metal oxides, such as nickel cobaltite, CoO or Co₃O₄ [59, 123, 101]. No inelastic background was subtracted from the spectra, as no quantitative evaluation of the data was performed.

Co 2p

Figure 5.6 shows the Co 2p spectra of all samples as well as reference spectra for CoO and Co₃O₄, which exist in the rock salt phase and normal spinel phase, respectively. The latter is known to resemble ideal inverse NiCo₂O₄ in its Co 2p spectrum and especially in its satellite structure because of similarities in the cobalt cation composition in both materials [8, 124, 101]. The main Co 2p_{3/2} and Co 2p_{1/2} peaks are visible in all spectra, as well as shake-up satellites at higher E_B [125, 126] and parasitic satellites at around 771 eV due to the non-monochromatic photon source. The different film spectra are nearly indistinguishable in their peak positions and intensities. The main Co 2p peaks are separated due to spin-orbit splitting with their measured positions being E_{B,Co_{1/2}} ≈ 795 eV and E_{B,Co_{3/2}} ≈ 779.7 eV after applying the binding energy correction mentioned above.

The Co 2p_{3/2} peak position fits the literature values for both CoO and Co₃O₄/NiCo₂O₄ at around 780 eV reasonably well, although the agreement with the Co₃O₄ reference peak position appears to be slightly better than that with the CoO peak. This is in line with the position found for both spinel structures in literature, with a separation of about 1 eV to the CoO peak [101, 107]. Similarly, the Co_{1/2} peak position and the resulting spin-orbit splitting fits the expected values for spinels like Co₃O₄ and nickel cobaltite (794.3 eV to 796.2 eV) [107, 127] as well as the measured reference spectrum for Co₃O₄ slightly better than those reported and measured for CoO (around 796 eV to 796.6 eV) [101, 125].

The peaks marked with the numbers 1-4 in figure 5.6 are shake-up satellites of CoO (1 & 2) and Co₃O₄ (3 & 4), respectively, although they are sometimes referred to as charge-transfer features as well [101]. The reported number and intensity distribution of the satellites varies, especially for Co₃O₄ [127, 125, 128, 129]. Generally, the satellite structure in CoO is much more pronounced and located at lower E_B relative to the main peaks, in comparison with that of Co₃O₄ and NiCo₂O₄ [129, 130]. As such, it can be used as an indicator for the existence of octahedrally coordinated Co²⁺ ions in the material, which should not exist in substantial amounts in the ideal cobaltite spinels. The satellite features are generally thought to be better suited for distinguishing octahedral Co²⁺ and Co³⁺ than the main peak positions because the latter are too close

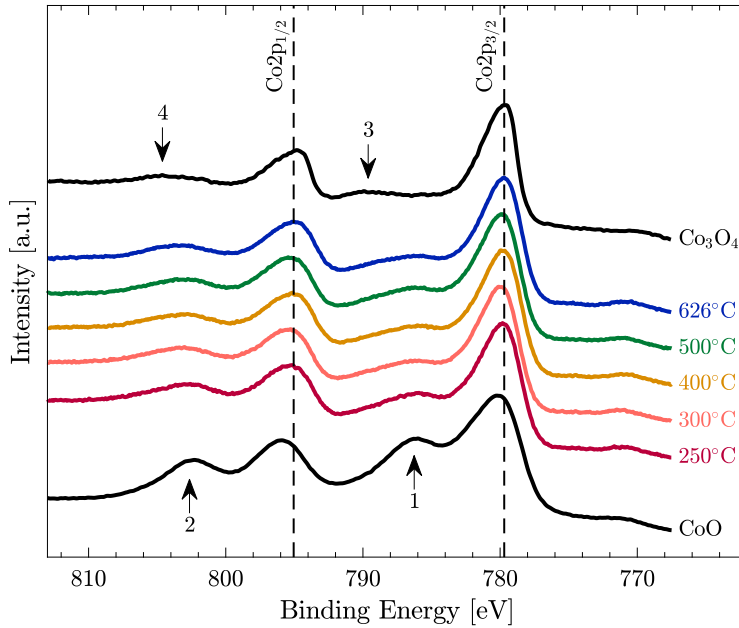


Figure 5.6: Co 2p spectra of the samples grown at different temperatures as well as reference spectra of CoO and Co_3O_4 specimen. The main Co $2p_{1/2}$ and Co $2p_{3/2}$ peaks of the grown films are marked with vertical lines. Satellite structures resulting from shake-up processes are marked by arrows for both reference spectra.

together for the cations of different valencies [101].

It is observable that the satellite structure of the grown films does not correspond fully to the ion configuration of either reference material, as the characteristic $\text{Co}_{\text{oct}}^{2+}$ peaks are present but less intense compared to the main peaks than in CoO. If the peaks 3 & 4 are present in the spectra, they are not clearly identifiable due to their low intensity.

In total, the characteristics of the film spectra seem to lie somewhere between those of CoO and the spinel, both in terms of the satellite structure and the main peak positions. This finding suggests a mixture of both a rock-salt and a spinel phase to exist inside the probed film surface. This would appear to contradict the spinel structure that is visible in the LEED measurements. It is possible that the films exhibited a spinel structure only shortly after the epitaxy process, decomposing over time, at least in part, into the rock salt structure. Similar effects were observed previously in nickel cobaltite films [131]. Alternatively, an excess of $\text{Co}_{\text{oct}}^{2+}$ ions could be present in a single spinel phase, which would have to be compensated for, at least in part, by nickel vacancies and/or Ni^{3+} , as well as Ni_{tet} ions, which do not appear in the ideal inverse spinel NiCo_2O_4 . In theory, it is possible to determine the amounts of cations in different oxidation and coordination states from a function fit of the 2p spectra, but the large number of functions and free parameters required to account for all different cation types would severely limit the amount of meaningful information that could be gathered from such a fit. Consequently, no such measure was undertaken in this work. Further investigation of the cation and phase distribution is instead relegated to sections 5.4 and 5.5.

Ni 2p

The Ni 2p spectra are presented in figure 5.7, together with reference spectra for NiO and the spinel NiFe_2O_4 , in which the nickel cations behave similarly to those in nickel cobaltite. The spectra consist of the main Ni $2p_{1/2}$ and Ni $2p_{3/2}$ peaks as well as their respective satellites and the parasitic satellites at about 844 eV. As before, all film spectra look nearly identical. The spectra consist of the main Ni $2p_{1/2}$ and Ni $2p_{3/2}$ peaks as well as their respective satellites and the parasitic satellites at about 844 eV. As before, all film spectra look nearly identical. The main peak positions of $E_{\text{B},\text{Ni}_{3/2}} \approx 854.7$ eV and $E_{\text{B},\text{Ni}_{1/2}} \approx 872.4$ eV are in reasonable agreement with their literature positions for NiO and nickel-containing spinels such as NiFe_2O_4 and nickel cobaltite [107, 132, 128]. In contrast to the Co 2p spectra, the Ni 2p satellites are expected to appear in the spinel as well as the monoxide because they are related to shake-up transitions in Ni^{2+} cations [132, 130]. As in the case of Co 2p, the satellites are sometimes also said to originate from charge-transfer effects instead [133, 128]. The distinctive two-peak structure of the Ni $2p_{3/2}$ main peak, as seen in both reference spectra, is ascribed to multiple different origins in literature. In NiO, the shoulder is generally thought to result from a screening effect of neighbouring NiO_6 clusters [134]. In contrast, in nickel spinels the shoulder is thought to result from either Ni^{3+} cations in the spinel structure [107, 130] or from additional NiO phases [134], as the spinel structure containing only Ni^{2+} exhibits no double main-peak structure [128]. The contributions to the main peaks in the spectra measured for this work cannot be properly distinguished due to a lack of resolution. As such, no additional information about the state of the Ni cations can be gathered from the 2p spectra.

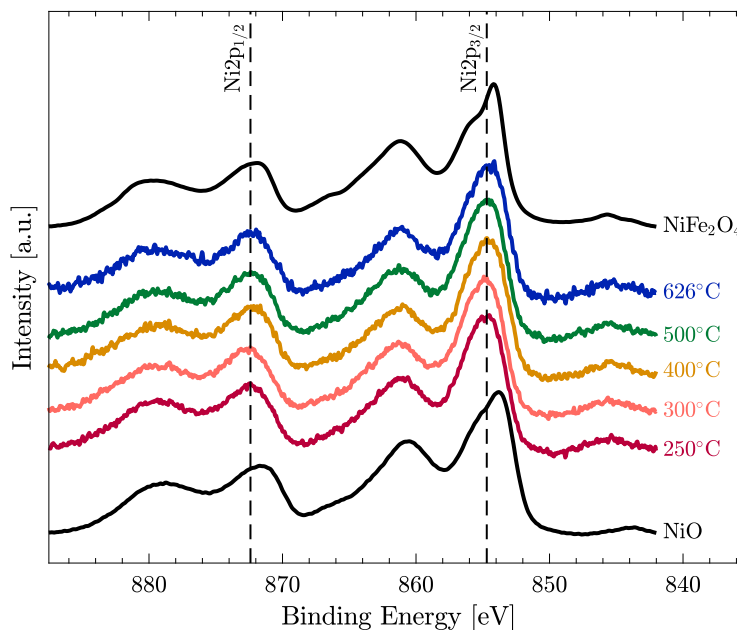


Figure 5.7: Ni 2p spectra of the samples grown at different temperatures as well as a reference spectrum of NiFe_2O_4 . The main Ni $2p_{1/2}$ and Ni $2p_{3/2}$ peaks of the grown films are marked. A linear background was subtracted.

5.3.2 3p spectra

Figure 5.8 shows the XP-spectra of both Ni 3p and Co 3p orbitals, as well as reference spectra for NiO, CoO and Co₃O₄, which, as shown in the 2p spectra, are closely related to the samples. The O 2s peak at about 23 eV is visible as well. Measurements were performed with an Al-source and a charge-neutralisation setup. The spectra were shifted in energy so that the C 1s peaks are situated at 285 eV [59, 135]. Traces of the reference satellite peaks marked 1 through 5 are visible in the film spectra, although peaks 2 and 4, as well as 1 and 5 overlap to an extent that makes separating them difficult. The peak and integral intensity of the main Ni 3p peak relative to the Co 3p peak shrinks with higher epitaxy temperature of the films, which indicates a change in stoichiometry.

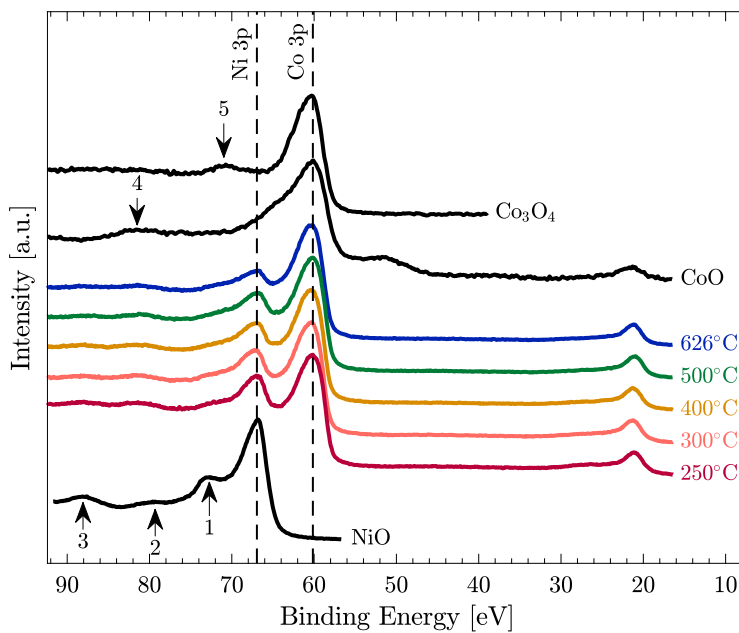


Figure 5.8: Measured Co and Ni 3p spectra of the grown films as well as reference spectra for Co₃O₄, CoO and NiO. The main 3p orbital peaks are marked, as well as satellite peaks of the reference materials 1-5. The O 2s orbital is included at low E_B .

3p spectrum fits

In order to investigate the stoichiometry in more detail, curve fits of the 3p spectra were performed. Figure 5.9 depicts an exemplary curve fit of the 400°C-sample spectrum shown in figure 5.8. A Shirley-background, calculated over the depicted range, was included in the spectrum. No sources specifying the individual component 3p peaks expected in a nickel cobaltite film could be found, so it was assumed that the spectrum should contain features found in NiO/NiFe₂O₄ and CoO, as well as Co₃O₄, since these materials are closely related to NiCo₂O₄. This approach is consistent with the observation that the Co 2p spectra show some characteristics of both rock-salt and

spinel phases. In order to separate the overlapping peaks resulting from Co and Ni, a reference measurement of NiO was fit according to literature (see appendix A). The relative intensities and positions of the main peaks in the resulting NiO-fit were carried over into the film spectra and held constant, while the satellite positions were fit as usual. The overlapping Co satellites had no additional constraints imposed on their parameters.

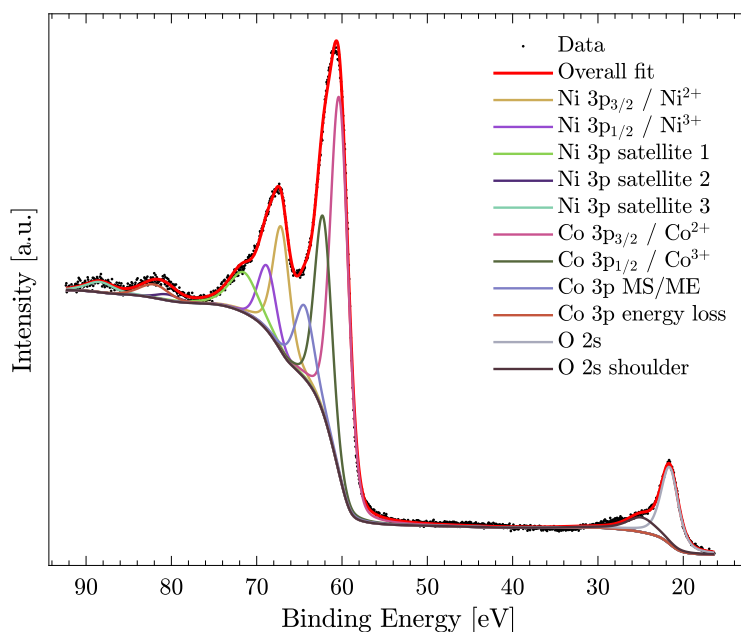


Figure 5.9: Exemplary composite curve fit of the 400 °C-film. The peaks are labelled according to their origin found in literature. A Shirley-background was included in the composite functions.

For both Ni and Co, the main peaks around 67 eV and 60.2 eV, respectively, were assumed to be composite features, containing what appears to be the two spin-orbit split $3p_{3/2}$ and $3p_{1/2}$ peaks. While it is oftentimes thought that the spin-orbit splitting in the 3p spectra of transition metals can only be resolved with difficulty [126], there have been attempts at distinguishing the spin-orbit split peaks, with energy differences between 1 eV and 2 eV for both elements [136, 137, 138, 123]. Alternatively, the 3p peak splitting is sometimes explained as originating from transition metal cations in different oxidation states [139, 140]. Good curve fits could not be produced without assuming split main peaks for both Ni and Co, and the spin-orbit splitting and chemical shift both seem to be a reasonable explanation for this fact. Additionally, three satellites, at about 72 eV, 81 eV and 88 eV, were included for Ni. The two satellites at lower energies are in agreement with literature values for both NiO and NFO [132, 128, 141], although no explanation of their origin could be found. The satellite at 88 eV was not found in literature, but it is visible in both reference spectra of NiO and NiFe_2O_4 (not shown), while not being present in the reference spectrum of CoO (see appendix B). Consequently, this satellite was considered part of the nickel spectrum in the stoichiometry calculations below.

While the main peak of Co 3p looks similar for both CoO and Co₃O₄ [125, 126], the satellite structure differs. A Co³⁺ peak at about 71 eV, which is expected for Co₃O₄ [126] and consequently for NiCo₂O₄, was originally included in the fits, but yielded intensities close to 0, so it was discarded. Additionally, peaks at about 64.4 eV and 82 eV had to be included to produce a good fit. Both peaks can be attributed to the presence of CoO-like, octahedral Co²⁺ in the films, as they result from multiplet splitting, multi-electron excitation and energy loss processes in CoO [125]. A third CoO satellite of unknown origin is visible in the reference spectrum and in previous works [142], but it was left out of the curve fits for similar reasons as for the Co₃O₄ satellite discussed above. The O 2s peak at 21.6 eV was included, as well as a shoulder at about 25.5 eV that is found in transition metal oxides, e.g. in NiO [59, 132]. Due to small surface charges that could not be compensated for by using the neutralisation system, additional peaks arising from uncharged parts of the surface could be present. These were not considered in the fit, because they could not be identified in the isolated C 1s and O 1s spectra and thus were deemed inconsequential.

Stoichiometry

The areas under the composite peaks in the resulting fits were summed up and used in equation 2.54 to determine the relative element quantities, also known as yields, in conjunction with literature values of 26 248 barns and 30 151 barns for the total photoelectric cross-section σ_{3p}^t (1486.6 eV) of Co 3p and Ni 3p, respectively [56]. To arrive at these values, both cross-sections of the 3p_{3/2} and 3p_{1/2} peaks were added to account for the whole spectrum. Additionally, the oxygen yield was calculated in the same manner, using a value of 1910.8 barns for $\sigma_{O\ 2s}^t$ (1486.6 eV). The resulting yields, $y_{Ni} = \frac{N_{Ni}}{N_{Ni}+N_{Co}}$ and $y_O = \frac{N_O}{N_O+N_{Ni}+N_{Co}}$, are shown for all samples in figure 5.10.

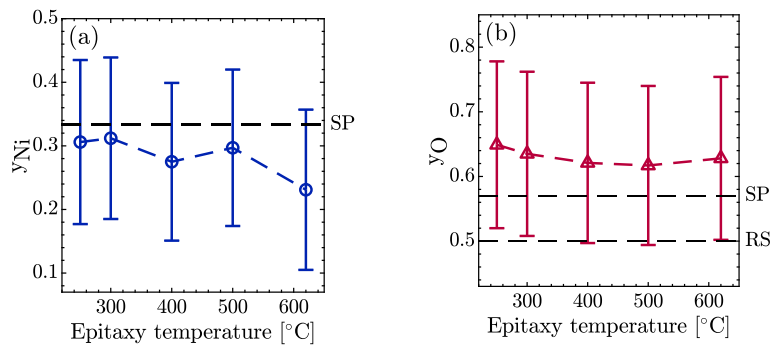


Figure 5.10: (a) Nickel and (b) oxygen yields of the grown films. An error of 20% was assumed for all values. The expected yields for ideal stoichiometric NiCo₂O₄-spinel (SP) and (Co/Ni)O rock-salt (RS) are included.

It is apparent that all y_{Ni} values are roughly equivalent, owing to the large error of about 20%, which was assumed due to the inaccuracies inherent in the XPS composite

fits, especially since a large amount of composite functions with multiple free parameters were used, and because the fitting process involving the NiO reference spectrum is certain to be - to some extent - non-physical because the sample structure and consequently the spectra are expected to differ slightly from pure NiO. Despite the large uncertainties, a tendency towards a lower amount of Ni can be seen for the 620°C-sample, which fits the qualitative observation of smaller Ni 3p peaks in figure 5.8. The oxygen yield is roughly constant between samples as well. It is apparent that the values of y_O fit the value of $y_{O,SP} \approx 0.57$ that would be expected in a spinel within the margin of error, although the yields tend towards larger values. The oxygen yields are more difficult to reconcile with the previously observed CoO characteristics, since (Co/Ni)O contains less oxygen than the spinel phase ($y_{O,RS} \approx 0.5$). A crystal structure containing phases of both the rock-salt and nickel cobaltite - as suggested by the Co 2p spectra - would be consistent with the deviations from the (Co/Ni)O-yield. The tendency towards higher yields than in the spinel could indicate a surplus amount of oxygen due to adsorbants (e.g. hydroxyls) or the occurrence of cation vacancies in the probed surface layer. To ascertain whether this method of acquiring the oxygen yield is reasonable, a reference measurement of CoO was investigated in the same way (see appendix B), resulting in a yield of 0.51, which is close to the expected value. As such, it seems that the tendency towards a larger amount of oxygen is a result of the material or adsorbate properties instead of being a systematic error of the evaluation method.

5.3.3 Valence band spectra

In order to supplement the observations above, the valence band region of all films was investigated using an Al-source as well as a charge neutralisation setup. The resulting spectra are depicted in figure 5.11 along with reference spectra of CoO and NiO.

The peaks marked 1, 3 and 5 are the main NiO 3d peak at 2.2 eV, as well as two satellites at about 4.05 eV and 9.25 eV. The main peak and the satellite at lower energy are related to 4T_1 and 2T_1 final states, respectively, while the broad high-energy satellite is a composite of two peaks originating from both states [143]. The arrows labelled 2, 4 and 6 show peaks of similar origin for CoO at positions of 1.75 eV, 4 eV and 10.4 eV. The main peak is a feature of the $3d^7L^{-1} \ ^5T_2$ final state, whereas the low-energy satellite results from Co 3d e_g orbitals and the high-energy satellite is a shake-up feature resulting from multi-electron excitations between the $3d^6$ final state and the O 2p orbitals [127, 144, 125, 145]. There are additional peaks in the energy range of 5 eV to 8 eV present in the spectra, which originate from the O 2p orbitals. Since these are difficult to resolve and differ only marginally between rock salt and spinel materials [127], they were not investigated further.

The film valence band spectra contain similar features as the reference materials but they also exhibit some differences. The satellite at about 3.75 eV is shifted slightly to lower binding energies when compared to what a composite of satellites 3 and 4 would look like. The high-energy satellite is likewise shifted to marginally lower E_B when compared to peak 6, though this might be explainable by the effect of peak 5

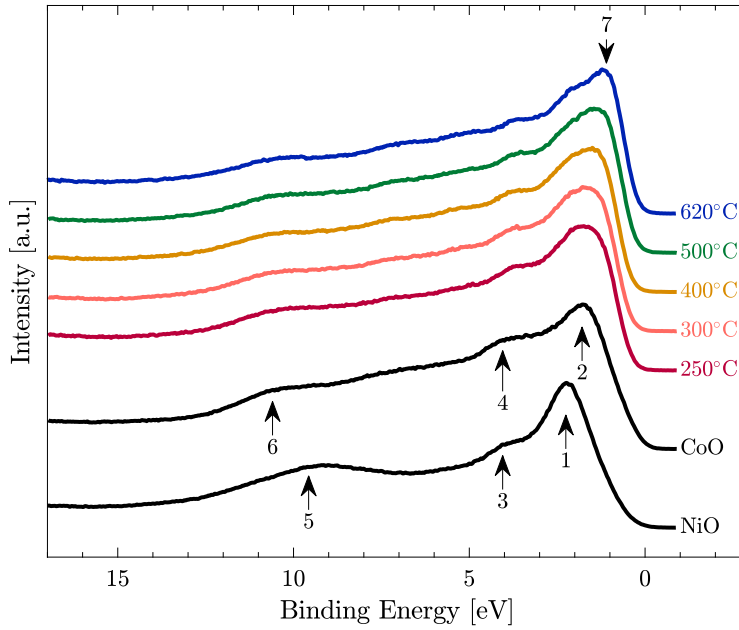


Figure 5.11: Valence band spectra of the samples. Peaks 1-7 mark characteristic features of different materials according to literature. Spectra of CoO and NiO are included for reference. The spectra were measured with a monochromatic Al source and shifted so that $E_{B, C 1s} = 285$ eV.

on its shape. The main peak of the sample spectra seems to gain some width towards lower binding energies when compared to peaks 1 and 2. This effect appears to become stronger for higher epitaxy temperatures. In the spectrum of the 620 °C-sample, the shoulder that is likely to originate from peak 1 is clearly separable from the peak at about 1.1 eV, marked as peak 7. This peak position is close to literature values for the main peak of Co_3O_4 , resulting from the $\text{Co}_{\text{oct}}^{3+} 3d^5 {}^2T_2$ final state [144, 127]. This could indicate a spinel character of the cobalt cation coordination that increases towards higher growth temperature. The existence of the satellite close to 11 eV, however, indicates a rock-salt phase even in the 620 °C-sample, because this satellite is not visible in cobaltite spinels such as Co_3O_4 [127]. Similarly, the small discrepancies between the satellite peak positions of the films and the reference spectra could be a result of a partial spinel character of the films, as suggested by the earlier investigations in this chapter.

It was considered that the shoulder originating from peak 1 possibly becomes distinguishable simply due to the lower nickel content as seen in figure 5.10 and not due to a shift in peak positions. The agreement of peak 7 with the literature position of Co_3O_4 could then result from a systematic error in correcting the energy shift due to charge build-up, which is achieved by moving the C 1s peak to 285 eV. Since this value is chosen somewhat arbitrarily, although based on literature [59], it might result in a shift of the whole spectrum to higher or lower energies than their real values. However, the satellites in the film spectra corresponding roughly to satellites 3 and 4 are at nearly constant positions, while the maximum in the main peak shifts by about 0.6 eV

between the samples. This observation is consistent with slight differences in the film structures being the cause for the differences in the valence band spectra instead of systematic correction errors.

A rise of spinel character with epitaxy temperature seems to contradict the LEED measurements as well as the 2p spectra, where the samples are nearly indistinguishable from each other. A possible explanation could be that the differences in phase composition between the samples are small and only visible in the valence bands, which are more sensitive to the valence states and coordination of the cations.

5.4 Transmission electron microscopy

The phase and element distribution of the films was investigated via TEM measurements on the 250 °C-sample. A cross-section of the film along the [010] axis close to the substrate interface is shown in figure 5.12. In the lower part of the image, the MgAl_2O_4 substrate is visible. It forms a clean and ordered interface with the grown film in the upper part of the image. The crystal structure of the film is divided into two phases, which appear to be randomly distributed, with one phase occurring predominantly. Three distinct parts of the image have been highlighted, showing the spinel structure of the substrate, the dominant structure in the film and the minority phase structure, respectively. Spatial Fourier transforms of these areas have been performed. It is apparent that the minority film phase has a spinel-like structure (a) that is roughly comparable to the substrate (c) but with broader peaks in reciprocal space. Both reciprocal structures are in reasonable agreement with the expected structure of MgAl_2O_4 $\langle 100 \rangle$ and NiCo_2O_4 $\langle 100 \rangle$, respectively [146]. However, the spinel structure in the film exhibits less intense NiCo_2O_4 (206) and (202) reflexes, indicating an imperfect spinel structure in the probed area, possibly due to some admixture of the majority phase. The majority phase has a rock-salt-like structure [147] (b), indicated by a lack of both the (206) and (202) reflexes, while the (004) reflex is still visible. While the film generally exhibits what appears to be a well-ordered crystal structure, there is a large disparity in contrast between different areas of the measured film cross-section. The thickness of the film was evaluated as being about 37 nm, which is in good agreement with the corresponding XRR fit in figure 5.3.

To further investigate the elemental distribution in the film, EDXS-based STEM measurements were performed with regard to the amounts of Co, Ni, Mg and Al in both the substrate and the film, the results of which can be seen in figure 5.13. Some dispersion of Mg into the film can be observed, but otherwise the film exhibits a clean interface to the substrate, as observed earlier. Elemental distributions both inside the substrate as well as in the grown film are mostly even, and no extended areas of higher element concentration can be found. An attempt was made to confirm the stoichiometry given by the XPS investigation. The individual element signals were integrated and their ratios were compared to the values expected from the stoichiometry. Both the substrate as well as the grown film exhibit a ratio B:A (for the structure AB_2O_4) of roughly

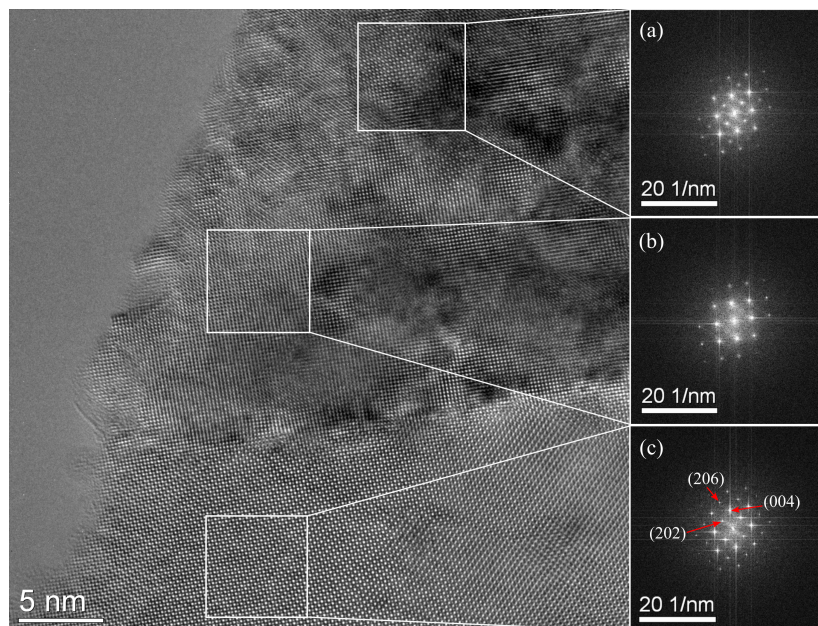


Figure 5.12: TEM cross-section of the interface between the substrate and the film grown at 250 °C. Two distinct phases are visible in the film. Spatial fourier transforms were performed for the marked areas of (a) the spinel phase component of the film, (b) the rock-salt phase component of the film and (c) the substrate, for reference. Three reflexes that are characteristic of the spinel and rock-salt structure are indicated.

1.12:1. It was concluded that the performed EDXS measurements can not be used for a proper quantitative analysis of the element ratios, although the stoichiometries of the substrate and the film seem to be similar, as expected from the XPS analysis. A qualitative analysis of the oxygen distribution (see figure 5.14) suggests that the film contains less oxygen than the substrate.

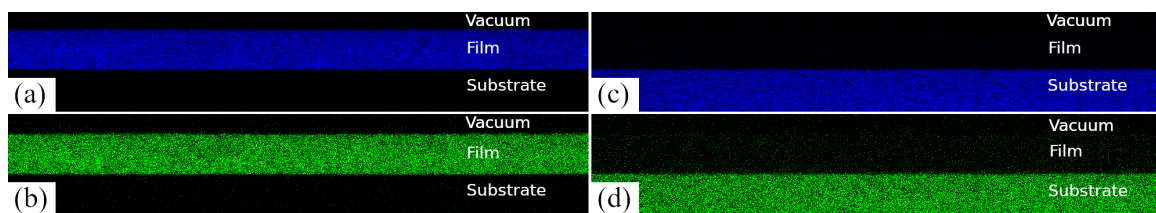


Figure 5.13: EDXS-based STEM cross-sections of the substrate-film interface. The distributions of (a) Co, (b) Ni, (c) Mg and (d) Al are shown, respectively. The elemental distributions in both materials are approximately uniform.

The spatial Fourier transforms indicate that the grown film is divided into spinel and rock-salt phases. The tendency towards less oxygen in the film compared to the substrate supports this observation, as do the previous XPS investigations, in which the films were shown to exhibit certain characteristics of both $\text{NiCo}_2\text{O}_4/\text{Co}_3\text{O}_4$ and $(\text{Co}/\text{Ni})\text{O}$. Since the elemental concentration is approximately uniform across the film, it is likely that the rock-salt consists of a mixed $(\text{Co}_\beta, \text{Ni}_{1-\beta})\text{O}$ phase, which was

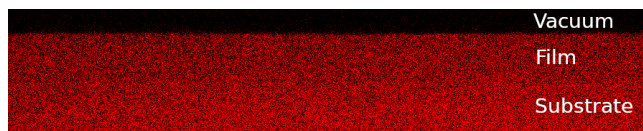


Figure 5.14: Oxygen distribution resulting from EDXS measurements of the substrate-film interface cross-sections. The oxygen amount in the film appears to be slightly lower than in the substrate.

previously reported as forming in mixtures of cobalt and nickel [96], rather than separate pure cobalt and nickel monoxides. For the same reason, the areas of different contrast are likely to result from crystal defects and a difference in crystallite orientations rather than a difference in elemental concentration. The minority spinel phase is likely to be nickel cobaltite, although the phase stoichiometry as well as the cation valencies and site distributions cannot be determined from the TEM structure analysis. A similar phase separation has been observed in nickel cobaltite films produced via pulsed laser deposition [147].

The slightly lower amount of oxygen in the film compared to the substrate is in contrast to the findings of the elevated oxygen amount as determined from XPS. This is consistent with the idea that the oxygen stoichiometry in the XPS measurements is altered by surface adsorbates like carboxides or hydroxyls and does not fully represent the film composition.

5.5 X-ray absorption

In order to further investigate the cation distribution and the phase composition of the film material, room temperature TEY X-ray absorption spectra of all films were measured. Figure 5.15 shows the nickel and cobalt XA-spectra of the prepared films. The spectra show clear signs of substantial amounts of $\text{Co}_{\text{oct}}^{2+}$ as well as $\text{Ni}_{\text{oct}}^{2+}$ being present, although the pronounced peak at about 779.2 eV indicates that the films also contain Co^{3+} cations [4]. In the Co spectra, a tendency towards a more pronounced CoO-like behaviour at lower epitaxy temperatures is visible, characterised by the double-peak structure at around 778.5 eV as well as the satellite at 776.8 eV. In the Ni spectra, the slight deviations in the satellite between samples follow no clear trend.

In order to obtain information about the phase compositions, CTM calculations were performed and the resulting curves fit to the measured spectra. Due to the multi-phasic nature of the films and a lack of additional information on the phase composition, there are too many free parameters to obtain both the amounts of the rock-salt and spinel phase as well as their cationic compositions without the input of assumptions about either into the fitting model. As a simple model, a mixture of an ideal inverse spinel $T[\text{Co}^{3+}]_O[\text{Co}^{3+}\text{Ni}^{2+}]_4\text{O}_4^{2-}$ as well as a mixed rock-salt $(\text{Co}_{\beta}^{2+}, \text{Ni}_{1-\beta}^{2+})\text{O}^{2-}$ were assumed to be present in the films. The spinel cation distribution was chosen because this is one of the possible NiCo_2O_4 distributions found in literature [148] and because it is close

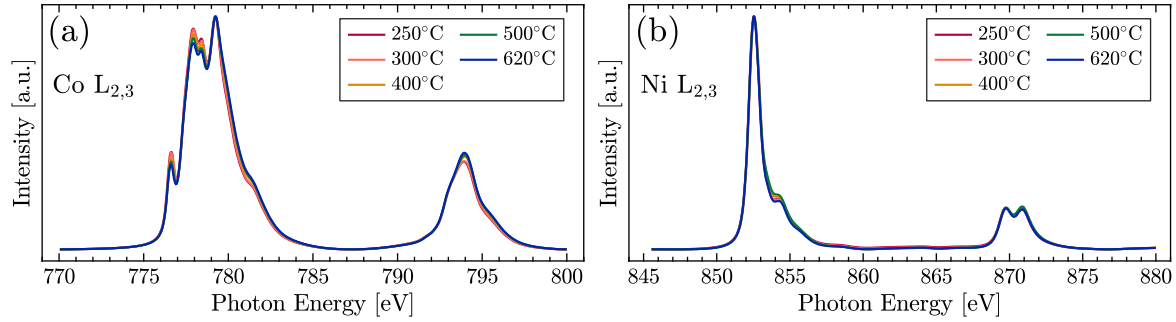


Figure 5.15: XA-spectra of (a) the Co $L_{2,3}$ and (b) Ni $L_{2,3}$ edges of the samples prepared at different epitaxy temperatures. The MCD spectra are omitted due to their low signal-to-noise ratio.

to the distribution found in other inverse transition metal spinels such as magnetite [149].

Inside the spinel, the tetrahedrally coordinated cations are assumed to be in high-spin states, with the cations on octahedral positions existing in a low-spin state [4], while the octahedral Co^{2+} in the rock-salt is in a high-spin state [101]. With this model, fits for all films were produced, one of which is presented in figure 5.16, corresponding to the 620 °C-sample. As fitting parameters, crystal fields of 2.1 eV ($\text{Co}_{\text{oct}}^{3+}$), 0.8 eV ($\text{Co}_{\text{oct}}^{2+}$), -0.6 eV ($\text{Co}_{\text{tet}}^{3+}$) and 0.9 eV ($\text{Ni}_{\text{oct}}^{2+}$) were used, along with charge-transfer parameters of 6 eV ($\text{Co}_{\text{oct}}^{3+}$), 6 eV ($\text{Co}_{\text{oct}}^{2+}$), 5 eV ($\text{Co}_{\text{tet}}^{3+}$) and 5 eV ($\text{Ni}_{\text{oct}}^{2+}$), and $U_{\text{dd}} - U_{\text{pd}} = -1$ eV for all cation types. The transition lines were broadened by Lorentzians with a width of 0.15 eV (L_3) and 0.3 eV (L_2) as well as a Gaussian with a width of 0.25 eV.

The XA-spectra of both cobalt and nickel are reasonably well reproduced. The discrepancy between measurement and fit at energies above the $L_{2,3}$ edges is typical for charge-transfer multiplet calculations [85]. Some discrepancies close to the edge can potentially be explained by the presence of a large amount of rock-salt in the film. The CTM model used in this work is limited to spinel structures and cannot fully reproduce the XA-spectrum of CoO and NiO. Since the ideal cation distribution used to fit the spectra is very simple and the resulting fits are not unique, the additional uncertainty introduced by this inability to adequately represent the rock-salt structure was deemed secondary.

The phase distributions resulting from the fits of all films are presented in figure 5.17 (for the calculation, refer to appendix C). As was already visible qualitatively from figure 5.15, the amount of rock-salt phase appears to shrink slightly at higher epitaxy temperatures, although the phase distributions are equivalent within the margin of error. This is in contrast to literature, where the decomposition of nickel cobaltite into the rock-salt monoxide was observed at epitaxy temperatures above 400 °C [124]. However, this finding is consistent with the slight tendency towards more spinel character in the valence band XP-spectra. The differences in phase compositions are small, especially when accounting for the uncertainties, and so it is plausible that they cannot be

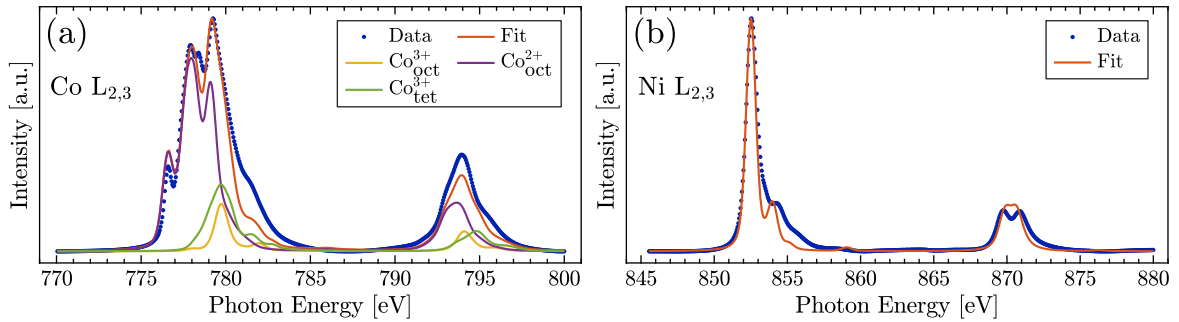


Figure 5.16: XA-spectra of (a) the Co $L_{2,3}$ edges and (b) the Ni $L_{2,3}$ edges of the 620 °C-film, together with the curve fit resulting from CTM calculations. In the cobalt spectrum, the individual cation contributions to the sum curve are shown. The nickel spectrum fit results solely from Ni_{oct}^{2+} .

observed in the LEED and 2p XPS measurements, where all films appear to be nearly identical.

The MCD signals (not shown) constitute less than 1% of the XAS signals and are consequently dominated by noise. As such, the usual method of using the sum rules to determine the elemental magnetic moments fails to produce sensible and usable results. For this reason, the MCD signal was not considered when evaluating the goodness of the fits. The magnetic properties resulting from the fits are instead further investigated in section 5.6, using the known spin moments of the ideal spinel and rock-salt structures in comparison to the measured moments.

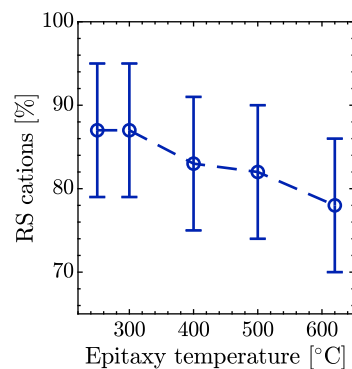


Figure 5.17: Ratio of all cations (Ni + Co) that are present in the rock-salt phase, according to the applied fit model containing an ideal inverse nickel cobaltite spinel. The uncertainties are estimated based on multiple fits using the same model with a similar goodnesses of fit but different resulting phase distributions.

The spectra were not corrected for saturation effects. Saturation compresses the maximum peak height, which would result in curve fits that overestimate the amount of rock-salt phase in the films and that underestimate the orbital moments compared to the spin moments. However, since the spectra were measured using TEY, saturation should not have a substantial effect on the interpretation of the curve fits, especially be-

cause no sum-rule analysis was undertaken. A more substantial limitation of the curve fits is the fact that they are not unique because other cation and phase distribution models are able to reproduce the XAS spectra just as well or better.

5.6 SQUID magnetometry

The temperature dependence as well as the magnetic field dependence of the film magnetisations were investigated via SQUID measurements, split into measurements of ZFC and FC temperature curves and field dependent hysteresis curves.

5.6.1 Temperature dependence

The temperature dependent curves of all samples and a bare MgAl_2O_4 reference substrate are presented in figure 5.18, without any background correction being applied. It is observable that the magnetic moments of all samples are substantially influenced by the background signal of the substrate, which shows a mixture of (super)paramagnetic behaviour approximately following the Curie law and a diamagnetic, negative background that is nearly temperature independent.

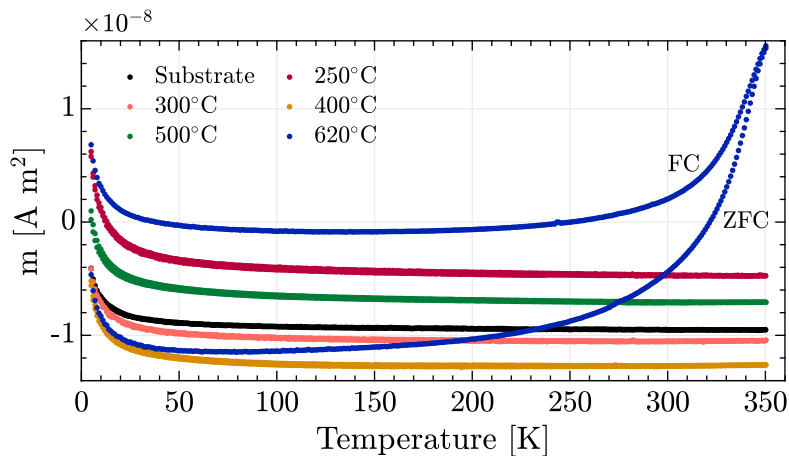


Figure 5.18: Temperature dependent magnetic moments of all films as well as a bare reference substrate with an applied field of 0.1 T. No steps for processing the data have been taken.

Since the substrate signal dominates the magnetisation signal of the films, it was subtracted by the method described in section 4.5.1. The background corrected magnetic moments were additionally transformed into Magnetisations M . Figures 5.19 to 5.23 show the corrected temperature dependent magnetisation curves of all samples in detail.

The ZFC and FC curves of the 250 °C-sample diverge slightly for most of the temperature range. Starting from 350 K where they almost meet, the difference between

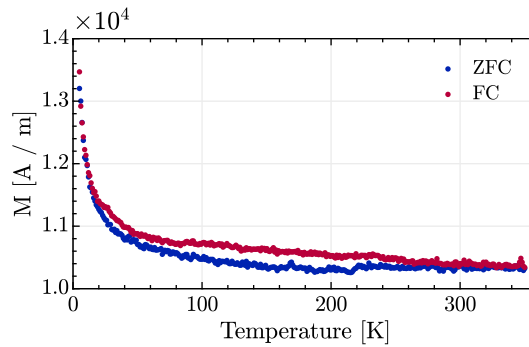


Figure 5.19: Temperature dependent magnetisation of the 250 °C-sample resulting from FC and ZFC measurements.

both curves rises until about 150 K, after which the curves start converging. It is difficult to say whether both curves meet at 5 K because of the large noise. The ZFC values lie below those of the FC curve over the whole range. The magnetisation rises mostly monotonously towards lower temperatures for both curves, except for a dip in the ZFC curve at 218 K and one in the FC curve around 80 K, both of which are artefacts that originate from the subtracted substrate signal, together with a bump in the curves around 25 K. Towards lower temperatures, the magnetisations start to rise at a much higher rate. Additionally, the magnetisation values are positive along the whole temperature range.

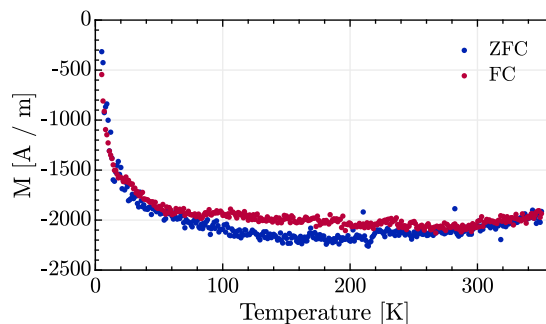


Figure 5.20: Temperature dependent magnetisation of the 300 °C-sample resulting from FC and ZFC measurements.

The ZFC and FC curves of the 300 °C-sample generally behave similarly to those of the 250 °C-sample. The difference between both curves rises starting from high temperatures, reaches a maximum at about 150 K and sinks again at low temperatures. At both extremes of the temperature range the curves potentially intersect, although the noise is too substantial to be certain. Starting from 350 K, the magnetisation in the FC curve sinks to a local minimum at about 280 K, at which point it starts rising in a similar way to the FC curve of the 250 °C-sample. The ZFC curve behaves similarly, with a local minimum around 180 K. At low temperatures, both curves start rising substantially. The magnetisation values are negative over the whole temperature range and the ZFC curve appears to stay below the FC curve, barring noise effects.

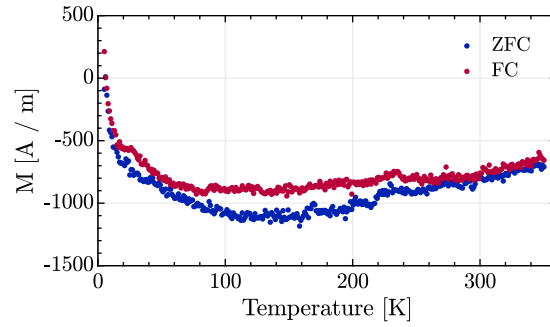


Figure 5.21: Temperature dependent magnetisation of the 400 °C-sample resulting from FC and ZFC measurements.

The difference between the ZFC and FC curves of the 400 °C-sample follows the same behaviour as described before for the 300 °C-sample, with a maximum difference around 150 K. The curves do not appear to intersect in the given temperature range. Starting from 350 K, the FC curve sinks until a temperature of about 140 K. At this point, the magnetisation stays roughly constant until around 80 K, where it starts rising, with the slope increasing toward low temperatures. The ZFC curve shows similar behaviour, with a minimum at about 140 K, after which the magnetisation starts rising again. Except for the values below 6 K, both curves stay at negative values over the whole temperature range, with the ZFC curve below the FC curve.

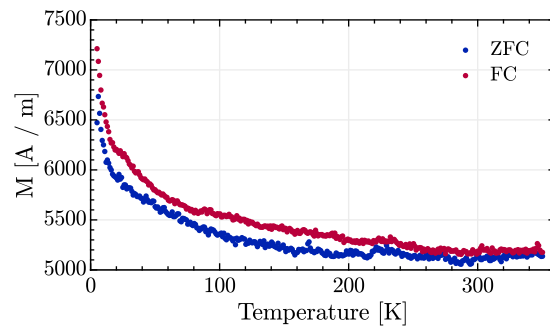


Figure 5.22: Temperature dependent magnetisation of the 500 °C-sample resulting from FC and ZFC measurements.

The difference between the ZFC and FC curves of the 500 °C-sample generally rises starting from 350 K, with dips at around 260 K and 65 K. No intersection of the curves is visible over the whole temperature range and the ZFC curve stays slightly below the FC curve. Starting from 350 K, the FC curve stays at roughly constant values to a temperature of about 280 K. At this point, the magnetisation starts rising similarly to the other curves, with a stronger slope at lower temperatures. The ZFC curve behaves almost identically, except that it sinks until about 280 K instead of being constant. Both curves contain only positive values over the temperature range.

Starting from 350 K where they almost touch, the ZFC and FC curves of the 620 °C-sample monotonously and substantially diverge down to 5 K, first rapidly until about

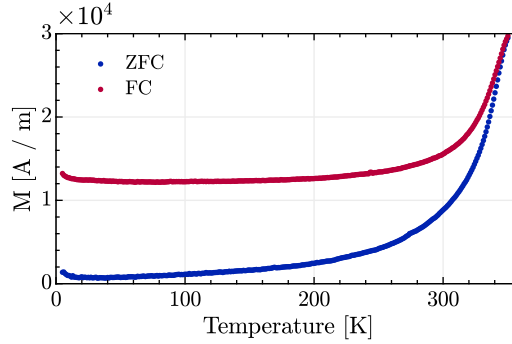


Figure 5.23: Temperature dependent magnetisation of the 620 °C-sample resulting from FC and ZFC measurements.

280 K and then less intensely, in a nearly linear way. The ZFC curve stays clearly below the FC curve over the whole range. At high temperatures, the FC curve sinks with a large slope that gradually decreases until a minimum is reached at about 80 K. From this point to 5 K, the curve is reasonable well described by a curie law dependence. The ZFC curve behaves similarly, with a more intense slope and a minimum at about 40 K.

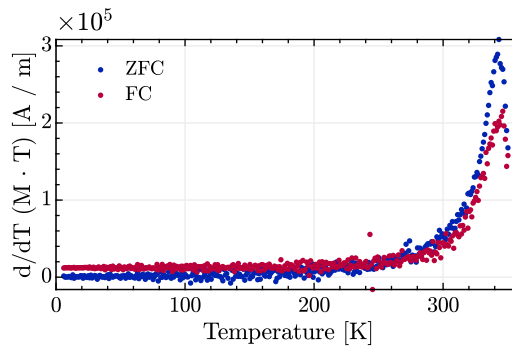


Figure 5.24: Temperature dependence of $\frac{d}{dT}(M \cdot T)$ for the 620 °C-sample. A maximum at about 344 K is visible for both the ZFC and FC curve.

Figure 5.24 shows the temperature dependence of $\frac{d}{dT}(M \cdot T)$ for the 620 °C-sample. This type of plot shows maxima at magnetic transitions, specifically close to antiferromagnetic to paramagnetic transitions, slightly below the Néel temperature [150]. In this plot, both the ZFC and FC curve exhibit maxima at about 344 K. As noted in the description of figure 5.23, the ZFC maximum is larger than that of the FC curve.

5.6.2 Field dependence

An exemplary overview of the field dependent magnetisations at 5 K of all samples, as well as a reference substrate, is presented in figure 5.25. The measured magnetic moments of the films were treated as described in section 4.5.1, that is, the background signals of the MgAl₂O₄ substrates, as well as of the sample holder, were subtracted

from the film magnetisations, along with corrections for a diamagnetic background and thermal drift being applied. An offset correction was applied as well, although the measured offsets were negligible.

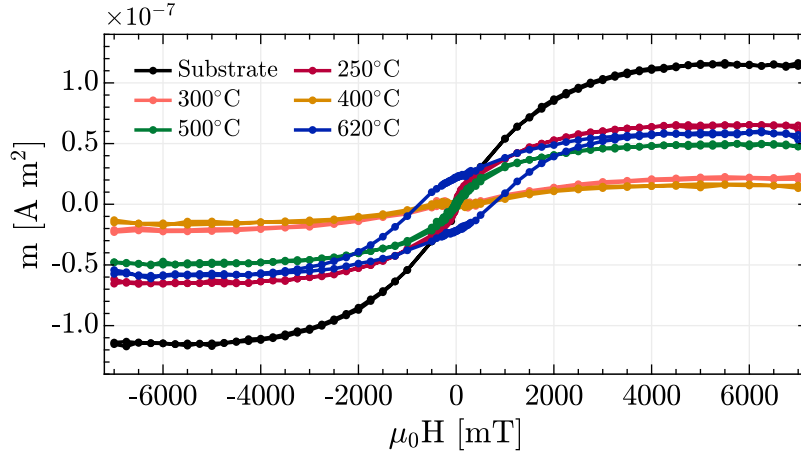


Figure 5.25: Overview of the field dependent magnetic moments of all films as well as a substrate, taken at 5 K. The background originating from the substrate and sample holder was subtracted from the shown sample measurements according to section 4.5.1.

It is apparent that only the 620 °C-sample shows signs of magnetic hysteresis, characterised by non-zero coercivity and remanence. The other samples, as well as the bare substrate, exhibit magnetic saturation at high fields (>5 T) but no significant differences between both loop directions. The films generally exhibit magnetic moments of similar magnitude, although the moments of the 300 °C and 400 °C-samples are notably smaller than those of the other films. These two samples are additionally affected by strong artefacts close to the origin.

The magnetic moments shown in figure 5.25 were subsequently transformed into magnetisations by normalising the measured values to the film volumes. Figures 5.26 to 5.30 show the field dependent magnetisation curves of all samples in more detail, measured at temperatures of 5 K, 80 K and 300 K each.

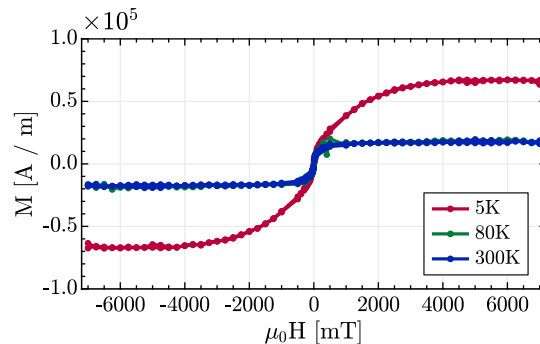


Figure 5.26: Field dependent magnetisation of the sample prepared at 250 °C.

The magnetisation curves of the 250 °C-sample exhibit similar behaviour at all three temperatures, with lower saturation magnetisation at higher measurement temperature. There is no discernible hysteresis in any of the curves. The curves at 80 K and 300 K are nearly identical and appear to be saturated at lower fields (>2 T) than the 5 K curve (>5 T).

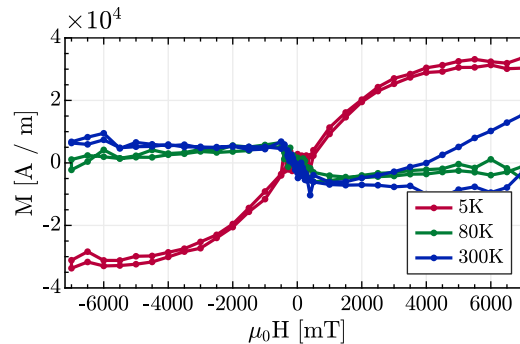


Figure 5.27: Field dependent magnetisation of the sample prepared at 300 °C.

The field dependent magnetisations of the 300 °C and 400 °C-samples are very similar. At 5 K, both films behave like the 250 °C-sample, insofar that saturation at high fields with no hysteresis is visible. Some differences between the measurements in both directions are visible, but these seem to be noise effects and they do not follow hysteretic behaviour. At fields lower than about 400 mT in magnitude, the curves are extremely noisy and the magnetisation appears to remain constant or even exhibit a small negative slope in that region.

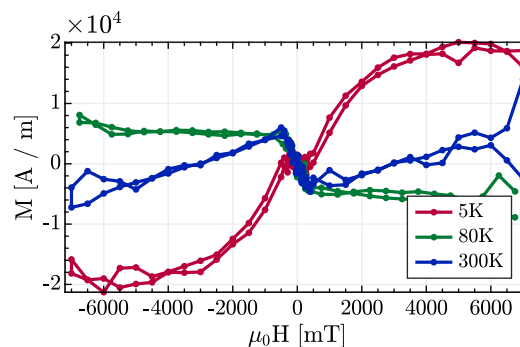


Figure 5.28: Field dependent magnetisation of the sample prepared at 400 °C.

The curves measured at 80 K and 300 K exhibit what appears to be a 'negative saturation magnetisation'. The extent of this negative saturation is roughly the same for both samples and both temperatures. This effect was deemed non-physical and it likely results from inaccuracies in the substrate background correction that become visible due to the small moments originating from the samples.

The magnetisation curves of the 500 °C-sample do not show any hysteresis. The measurement taken at 300 K exhibits higher magnetisations than the measurement taken

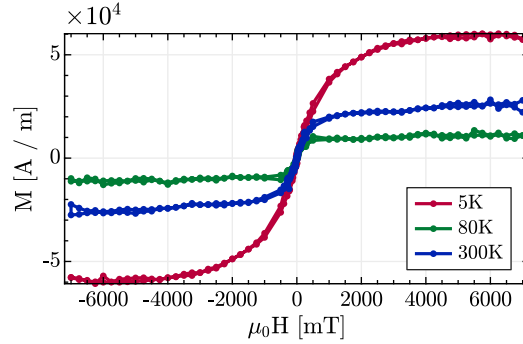


Figure 5.29: Field dependent magnetisation of the sample prepared at 500 °C.

at 80 K, while both are lower than the magnetisations at 5 K. The lower the saturation magnetisation, the sooner the saturation is reached.

Figure 5.30 shows the field dependent magnetisation curves of the 620 °C-sample as well as the corresponding remanence and coercivity values. The uncertainty ranges were estimated by applying multiple types of physically sensible background and slope corrections and noting the maximal difference in the resulting values. At all three temperatures a closed hysteresis loop is visible. The coercivity values at 5 K and 80 K are identical within their range of uncertainty, but there is a trend towards lower coercivities at higher temperatures, with a value close to zero at 300 K. Correspondingly, the areas inside the hysteresis curves shrink with higher measurement temperature. The coercivity values at 5 K and 80 K are larger than exemplary coercivities found in literature [9]. The measurement taken at 300 K exhibits a higher saturation magnetisation than the measurement taken at 80 K, but the remanence values shrink with higher temperature.

Figure 5.31 depicts an overview of the saturation magnetisations M_S of the films at all three measurement temperatures, which were determined from the field-dependent magnetisation plots shown above. It can be seen that, at 5 K, the magnetisations of the 250 °C, 500 °C and 620 °C-samples are close together with values between 59 kA/m and 70 kA/m, whereas their M_S values at higher temperatures diverge significantly. The drop in M_S at higher temperatures is much less pronounced for the 620 °C-sample than for the others, and its M_S values at 80 K and 300 K are identical within the margin of error at about 43 kA/m. The latter holds for the 250 °C-sample as well with values around 19 kA/m. As mentioned before, the M_S value of the 500 °C-sample measured at 300 K (ca. 25 kA/m) significantly exceeds that measured at 80 K (ca. 12 kA/m), which can not be accounted for by the given errors. The M_S values of the 300 °C and 400 °C-samples are less than half as large in magnitude as those of the other samples at 5 K and were taken to be zero at the other measurement temperatures, as the observed negative saturation magnetisation was deemed non-physical. The films have M_S values that are roughly an order of magnitude below those of nickel cobaltite films found in literature [109].

The ideal inverse nickel cobaltite spinel has a spin magnetic moment of $2\mu_B$ /f.u. [4].

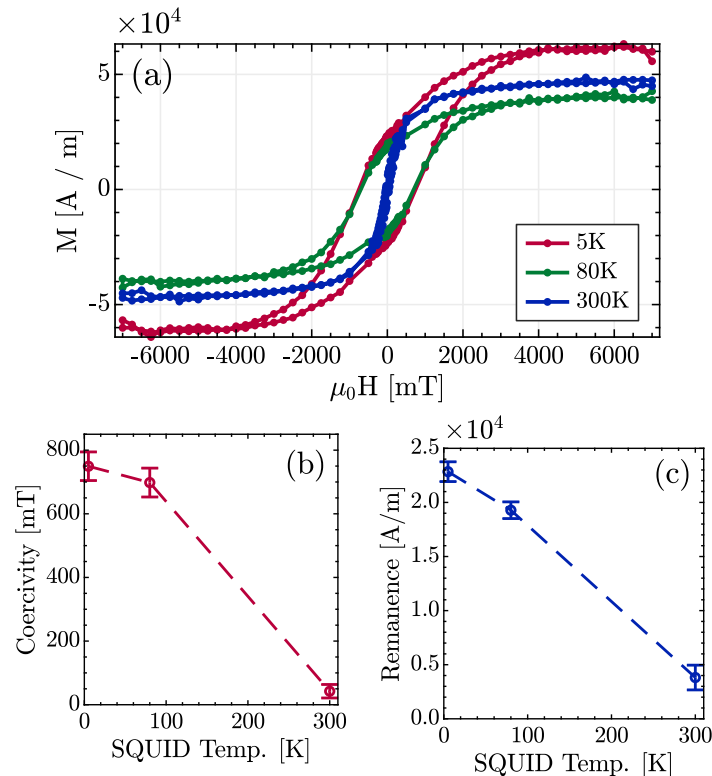


Figure 5.30: (a) Field dependent magnetisation of the sample prepared at 620 °C, measured at 5 K, 80 K and 300 K, as well as the resulting (b) coercivity and (c) remanence values.

In order to determine whether the fit model used in section 5.5 can sensibly describe the films produced in this work, the ideal magnetic moment was used together with the crystal phase cation ratios determined from the XAS fits in order to calculate theoretically expected values for M_S at 0 K. The calculation results are depicted in figure 5.32 along with the measured values at 5 K. The calculation errors were estimated from the uncertainties in the stoichiometries as well as the phase distribution difference between multiple fits of the same quality and with the same model.

It is apparent that the calculated values are in the same order of magnitude as the measured values. Despite the large uncertainties, not all calculations are in agreement with their measured counterparts. The calculated value of the 400 °C-sample is significantly larger than its corresponding measurement, while the calculated value for the 250 °C-sample is slightly smaller, although the values are still identical within the error range. The other calculated values are all within the error range of their measured value, while generally tending towards a slightly larger magnitude. It should be noted that the calculations omit the orbital moment contribution and that they might be influenced by saturation effects, which means they have a tendency to be slightly lower than the 'real' expected values.

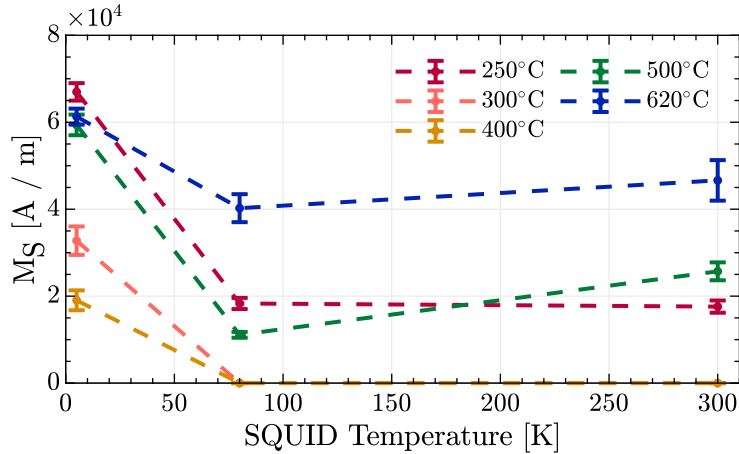


Figure 5.31: Saturation magnetisations of all grown films as determined from the field-dependent magnetisation plots. The errors were estimated by varying the type of background correction and noting the change in the resulting M_S -values.

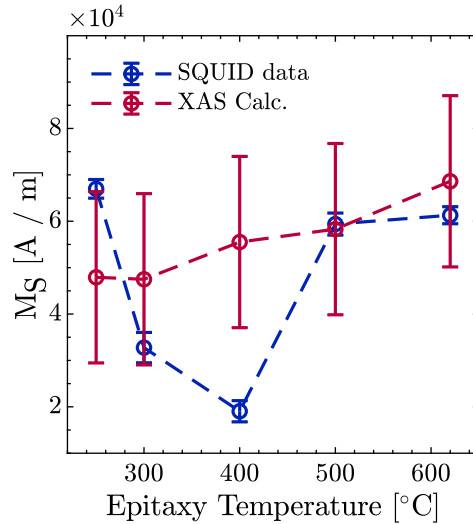


Figure 5.32: Measured M_S -values at 5 K as well as M_S -values calculated from the theoretical spin moment of $2\mu_B$ /f.u. for an ideally inverse nickel cobaltite spinel with the phase distributions resulting from the XAS evaluation in section 5.5.

5.6.3 Discussion

In this section, the results of the magnetisation measurements presented above will be discussed in the context of the previous investigations.

Looking at the whole range of measurements, it becomes apparent that the 620 °C-sample differs from the others in its magnetic behaviour, in that it exhibits magnetic hysteresis as well as a strong splitting of the ZFC/FC curves and a maximum in the temperature measurements. The magnetic hysteresis fits the ferrimagnetic behaviour

of ideal NiCo_2O_4 , which is also found in literature [4, 1]. However, the fact that the temperature dependence of the magnetisation exhibits a strong field cooling splitting as well as a maximum is more typical of antiferromagnets [151], where the maximum in magnetisation is caused by the paramagnetic phase transition at the Néel temperature. The plot of $\frac{d}{dT}(M \cdot T)$ is known to have a maximum slightly below T_N [150], which is observable here as well. At first glance, these observations seem to be in contrast to each other, but a possible explanation can be found in the phase separation into spinel and rock-salt inside the film that is suggested by the results of the XPS, XAS and TEM measurements. The rock-salt phase should behave antiferromagnetically [92, 94], while the magnetism of the spinel phase depends on its cation compositions, with an ideally ferrimagnetic behaviour [4]. In this view, the antiferromagnetic temperature dependence of the magnetisation could be a result of the rock-salt phase and the hysteretic field dependence a result of a ferrimagnetic nickel cobaltite spinel phase. The T_N -value of about 350 K would fit a mixed Ni/Co monoxide with an abundance of cobalt because the transition temperature of the monoxide shifts between that of NiO and CoO depending on the stoichiometry [96]. It is plausible that the ferrimagnetic spinel signal is dominated by the rock-salt in the temperature dependent magnetisation measurement because the spinel transition temperature can be larger than 400 K [1], which is outside of the probed temperature range, and because the ratio of rock-salt to spinel phase in the film appears to be very large, with close to 80 % of the film cations belonging to the rock-salt phase according to the XAS fits. At the same time, the spinel can dominate the field dependent measurement because its ferrimagnetic field response is much stronger than that of the antiferromagnetic rock-salt. The calculated saturation magnetisation in figure 5.32 fits the measured value for the 620 °C-sample reasonably well, which is consistent with the model of an ideal spinel as minority phase in this sample.

The films prepared at lower epitaxy temperatures exhibit markedly different behaviour from the 620 °C-sample, but are very similar to each other. Notably, they share their magnetic characteristics with the bare MgAl_2O_4 substrate, despite the latter being reported as being an antiferromagnet or diamagnet [105, 102]. Their collective field dependent magnetisation plots bear similarity to the behaviour of superparamagnets, mainly due to the lack of hysteresis while simultaneously exhibiting saturation at relatively low external fields. In contrast, a normal paramagnet is expected to experience saturation at fields of multiple hundred T [27]. A possible cause for this behaviour are ferromagnetic impurities in or on top of the substrate and the samples or inside the SQUID sample holder. Similar field- and temperature-dependent magnetisations were also discovered after neutron diffraction of MgO-films [152], where point defects were determined to be the cause. Additionally, a similar temperature dependent behaviour was observed in CoO films [110], in contrast to their expected temperature curves with a maximum magnetisation close to 300 K [153]. In both cases, no (substantial) field cooling splitting, antiferromagnetic transitions or blocking temperatures were visible, as is the case for the low-temperature samples and the substrate measured in this work. No explanation for the lack of ZFC/FC splitting, apparent blocking temperature and antiferromagnetic transition could be found. There are no impurities visible in the XP-

spectra, but this only means that they are not concentrated in substantial amounts at the surface at the time of measurement. Impurities could still be present in the bulk of the films or they could be introduced while loading the samples into the magnetometer.

A possible reason for the lack of a field-dependent hysteresis in the low-temperature films could be a difference in the cation composition of the spinel phase compared to the 620 °C-film. The composition variance could lead to the spinel phase being non-magnetic [3, 107]. This would mean that the samples exhibit antiferromagnetic behaviour in both phases, which is dominated by superparamagnetism induced by ferromagnetic impurities or point defects, as previously observed in CoO and MgO. On the extreme end of the possible antiferromagnetic cation compositions in the spinel phase is Co_3O_4 . However, the Néel temperature of Co_3O_4 is ~ 40 K [36], which means that its magnetic transition should be visible in the temperature-dependent magnetisation curves. No magnetic transition is visible in the low temperature films, although the transition could be suppressed by the superparamagnetic effects similar to that of the rock-salt phase.

The question would remain, why the antiferromagnetic transition in the 620 °C-sample - that is supposedly an effect originating from the rock-salt phase - is not dominated by the superparamagnetic effects seen in the other samples, which in this model are antiferromagnetic as well. The simplest explanation would be that the impurities or defects are not present in the 620 °C-film. Another possible explanation can be found in the fact that the crystallite size in films epitaxially grown at higher temperatures is larger on average [154, 155]. At 620 °C, the crystallites could have an average size that is just large enough to enable long-range ordering in multi-domain states of the impurities, preventing the superparamagnetic effects induced by them and consequently preventing the suppression of the antiferromagnetic transition in the rock-salt by the unknown mechanism. The smaller FWHM in the LEED peaks of the 620 °C-sample compared to the other samples is consistent with this idea. However, this also means that the ferrimagnetic behaviour seen in the 620 °C-sample could result from the impurities instead of the spinel phase, at least in part. The same applies to the M_S -values of all films, which consequently depend on the unknown spinel cation distribution as well as the impurities. In this view, it is impossible to separate the contributions of the film material from those of the impurities/point defects without additional information about their exact compositions. While it would in theory also be possible that the superparamagnetism in the films stems from clusters of (partial) nickel cobaltite instead of impurities or point defects, as it is seen e.g. in some ferrite spinels [156], this would not explain the nearly identical behaviour of the bare substrate. The minuscule MCD signals at the cobalt and nickel edges seem to be consistent with the idea that the ferrimagnetic behaviour might not originate from the nickel cobaltite phase.

In a similar view, the field cooling splitting as well as the maximum in magnetisation could potentially be explained by the film existing in a spin-glass state, with long-range interacting nickel cobaltite clusters being dispersed inside the rock-salt. In this view, the temperature dependent behaviour would be a result of complex spin-glass transitions and/or freezing effects instead of the antiferromagnetic transition of the rock-salt.

If the films can be described as spin-glasses, it is possible that only the 620 °C-sample contains a critical amount of the ferrimagnetic spinel phase necessary to allow the system to transition into a ferromagnet-like state [27]. Below this critical ferrimagnetic spinel amount, the films could potentially behave (super)paramagnetically (as seen e.g. in [157]). However, spin-glass freezing temperatures are typically in the range of < 50 K, which makes this explanation unlikely as no maxima in the temperature curves can be observed in this temperature range. Additionally, this model provides no explanation for the lack of ZFC/FC splitting in the low-temperature films or for the fact that the bare substrate exhibits a near identical temperature-magnetisation curve, which is why it is less plausible than the impurity model described above. Additionally, the phase distribution appears to differ only slightly between the films, judging from the XAS fits as well as the fact that no discernible differences between the films are visible in LEED and in the Co 2p XP-spectra, which makes it unlikely that the amount of spinel phase, rather than its composition or the impurity crystallite size/amount, is the critical parameter related to the magnetic behaviour differences between the films.

Another possible cause for the ferrimagnetic behaviour of the 620 °C-film can be found in nickel vacancies (with preferred spin direction) caused by the low stoichiometry, as this effect is known to appear in under-stoichiometric NiO [158]. In this model, the temperature dependence would again be defined by the rock-salt, which dominates the spinel phase of unknown composition. It is unclear whether this vacancy-effect could also appear in the spinel phase or whether it would be limited to the rock-salt. In either case, the ferrimagnetic behaviour could be an effect of both the rock-salt as well as the spinel phase in this model. The superparamagnetic effects would still have to be ascribed to the impurities, however.

In general, the nature of the phase compositions is the key to understanding the difference between the superparamagnetic films and the ferrimagnetic film produced in this work. Of the above models, the most plausible explanation of the collective film behaviour seems to be that the films are dominated by point defects or ferromagnetic impurities, which result in superparamagnetism at low epitaxy temperatures and ferrimagnetism at 620 °C. The composition of the spinel and rock-salt phases could vary substantially between the films and the magnetic behaviour would be a result of both impurity/defect effects as well as the spinel. However, the above speculations would need to be experimentally confirmed by additional experiments that allow the conclusive determination of the phase compositions inside the films, which go beyond the scope of this work.

6 | Summary & Outlook

In this work, an attempt was made to produce stoichiometric $\text{NiCo}_2\text{O}_4(001)$ films on top of $\text{MgAl}_2\text{O}_4(001)$ substrates by means of reactive molecular beam epitaxy under an atomic oxygen atmosphere at various temperatures from 250°C to 620°C . The films were characterised according to their structure, stoichiometry and magnetic behaviour using XPS, LEED, XRR, TEM, XAS and SQUID.

The films are slightly understoichiometric according to the 3p XP-spectra, with the 620°C -film containing the lowest amount of nickel and the XRR measurements give their thickness as around 37.67 ± 1.94 nm, which was confirmed via TEM. The XP-spectra in conjunction with the TEM images suggest a film structure consisting of separate, randomly distributed rock-salt and spinel phases. The measured LEED patterns possibly point towards a stronger spinel character than that seen in the other measurements, but they are not inconsistent with the separation into the two phases. In the LEED measurements and in the 2p XP-spectra, no significant difference between the samples can be seen, while both the valence band XP-spectra and the XAS curve fits suggest a slight increase in spinel character towards higher epitaxy temperatures. The films differ more fundamentally in the SQUID magnetisation measurements, where the 620°C -film exhibits what appears to be a mixture of ferrimagnetic and antiferromagnetic behaviour, with magnetic hysteresis in the field-dependent measurements and a splitting of the ZFC and FC curves as well as a maximum in magnetisation in the temperature-dependent measurements. In contrast, the other films exhibit superparamagnetic behaviour in the field-dependent measurements, but no ZFC/FC splitting and no extrema in the temperature curve. This behaviour seems to be most in line with that of films dominated by point defects or impurities, which result in superparamagnetic effects. A reasonably plausible explanation for the difference between the 620°C -film and the others can be found in the occurrence of larger crystallites with higher epitaxy temperatures, which prevent the superparamagnetic effects, resulting in ferrimagnetic hysteresis and in the antiferromagnetic transition becoming visible. However, the mechanism by which the superparamagnetism is related to the suppression of the ZFC/FC curve splitting and of the antiferromagnetic transition is unclear, as well as the extent to which the magnetic behaviour of the films is determined by the spinel and rock-salt phases as opposed to the impurities/point defects.

Further investigations into the structure, phase composition and magnetic characteristics of the films are necessary in order to fully understand the behaviour of the films

and especially to understand the effects that result in the distinctive properties of the 620 °C-film. Specific heat capacity measurements could be performed to confirm whether the maximum in the temperature-magnetisation curve corresponds to an antiferromagnetic transition, because the specific heat is known to exhibit a maximum at the transition temperature in conjunction with that of the magnetisation [159]. Conductance measurements could be performed in order to relate the magnetic properties of the films to their conductivity. Nickel cobaltite films are known to have strongly coupled transitions from magnetic metal behaviour to that of insulating non-magnets [4, 3]. If the magnetic properties of the films, especially the ferrimagnetism, are a result of the spinel phase, the conductivity measurements should reflect this. A closely related property is the magnetoresistance, which could also be investigated to further relate the magnetic properties of the films to the phase composition. To gain more insight into the film structure, both the out of plane/in plane lattice constants as well as the geometry dependence of the magnetisation could be investigated, the latter using e.g. high-field MOKE measurements. This could serve to differentiate between the effects induced by the different phases because the magnetisation direction and crystal structure differs between nickel cobaltite and the (mixed) monoxide. Potential effects include a shift of the easy axis depending on the amount and cation composition of the spinel phase. The lattice constants as well as the phase compositions could be determined using X-ray diffraction.

Finally, the array of experiments mentioned above and those performed in this work could be repeated for additional nickel cobaltite films, prepared under different conditions. An increase of the oxygen partial pressure could result in a larger amount of spinel phase inside the films and/or a cation distribution with a larger magnetic moment, as it is the case for many ferrimagnetic nickel cobaltite films in literature [2, 4, 3]. Other preparation parameters could be varied as well. For example, the oxygen plasma source could be kept on for the complete duration of the cooling process after the epitaxy is finished, in order to prevent a possible decomposition or reduction of the film at high temperatures.

Zusammenfassung

Gegenstand dieser Arbeit war die Herstellung und Charakterisierung näherungsweise stöchiometrischer $\text{NiCO}_2\text{O}_4(001)$ -Schichten auf $\text{MgAl}_2\text{O}_4(001)$ -Substraten. Die Filme wurden mithilfe reaktiver Molekularstrahlepitaxie unter atomarer Sauerstoffatmosphäre bei Temperaturen zwischen 250°C und 620°C hergestellt. Struktur, Stöchiometrie und magnetische Eigenschaften der Proben wurden mithilfe von XPS-, LEED-, XRR-, TEM-, XAS- und SQUID-Messungen charakterisiert.

Ausgehend von den 3p XP-Spektren sind die Schichten leicht unterstöchiometrisch, wobei die 620°C -Schicht am wenigsten Nickel enthält. Die Dicken liegen laut XRR bei $37.67 \pm 1.94 \text{ nm}$, was durch TEM-Messungen einer Probe bestätigt wurde. Die XP-Spektren sowie die TEM-Bilder legen eine Struktur bestehend aus separaten Steinsalz- und Spinellphasen nahe. Während die LEED-Bilder tendenziell einen größeren Spinellanteil nahelegen, sind sie vereinbar mit der Separation in beide Phasenanteile. Die Proben zeigen in den LEED-Bildern und den 2p XP-Spektren keine signifikanten Unterschiede auf, während die Messungen der Valenzbänder und die Röntgenabsorptionsspektren auf einen leichten Anstieg des Spinellcharakters der Filme mit höheren Epitaxietemperaturen hindeuten. In den SQUID-Magnetisierungsmessungen zeigen sich größere Unterschiede zwischen den Proben. Die 620°C -Probe zeigt eine Mischung aus ferrimagnetischem und antiferromagnetischem Verhalten, mit magnetischer Hysterese in den feldabhängigen Messungen und einem Maximum in der magnetisierung sowie einem Aufspalten der ZFC und FC-Kurven in der temperaturabhängigen Messung. Die anderen Schichten zeigen dagegen superparamagnetisches Verhalten in der feldabhängigen Messung, aber ohne ein Aufspalten der ZFC und FC Kurven oder ein erkennbares Maximum in der temperaturabhängigen Messung. Dieses Verhalten entspricht qualitativ dem Verhalten von Schichten, in welche Punktdefekte oder Verunreinigungen dominant sind, was in Superparamagnetismus resultiert. Eine mögliche Erklärung für den Unterschied zwischen der 620°C -Probe und den restlichen Proben könnte die Entstehung größerer Kristallite bei höheren Epitaxietemperaturen sein. Diese könnten die Superparamagnetische Effekte verhindern, was darin resultiert, dass eine ferrimagnetische Hysterese sowie ein antiferromagnetischer Übergang in der Temperaturmessung sichtbar werden. Der Mechanismus, über den dieser Superparamagnetismus aufgrund von Punktdefekten und/oder Verunreinigungen mit der Unterdrückung der ZFC/FC-Aufspaltung sowie des antiferromagnetischen Phasenüberganges zusammenhängt, bleibt dabei unklar. Zudem ist ohne weitere Untersuchungen nicht zu klären,

inwieweit das magnetische Verhalten der Schichten von den Steinsalz- und Spinellphasen oder von den Punktdefekten bzw. Verunreinigungen bestimmt wird.

A | NiO reference fit

Figure A.1 shows a composite function fit of the reference NiO 3p-spectrum that is included in figure 5.8. The included peaks are the same as those mentioned for NiO in section 5.3.2. A Shirley-background was subtracted from the spectrum prior to curve fitting.

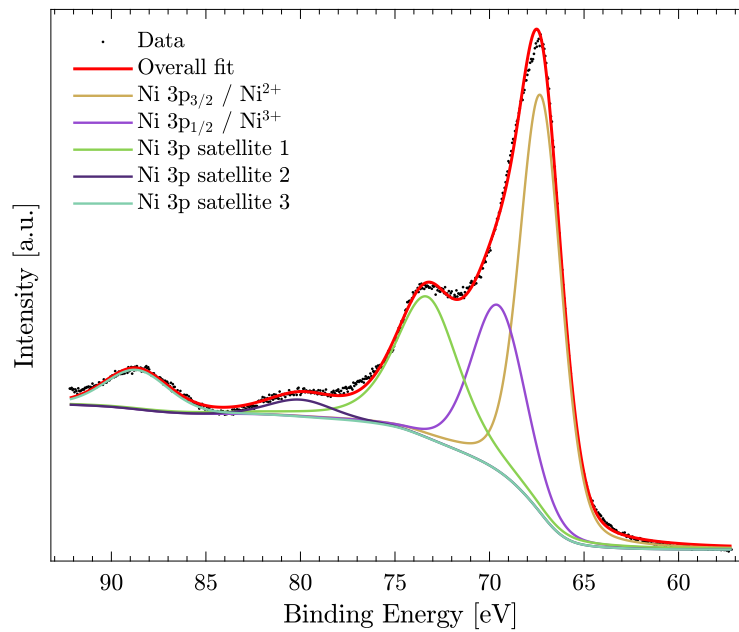


Figure A.1: Composite curve fit of a reference NiO sample. The peaks are labelled according to their origin found in literature. A Shirley-background was included in the composite functions.

B | CoO reference fit

Figure B.1 shows a composite function fit of the reference CoO 3p and O 2s spectrum that is included in figure 5.8. The included peaks are the same as those mentioned for CoO and oxygen in section 5.3.2. A Shirley-background was subtracted from the spectrum prior to curve fitting. The curve fit was evaluated for the relative amounts of cobalt and oxygen, resulting in a yield of $y_{\text{O}} = \frac{N_{\text{O}}}{N_{\text{O}} + N_{\text{Co}}} = 0.51$, which is close to the expected value of 0.5. The individual composite functions were not constrained for the fitting process because only the total area belonging to the cobalt and oxygen peaks is relevant for the yield calculation. The peak labelled 'Co 3p satellite' is not included in the investigation in section 5.3.2 because it could not be distinguished from the neighbouring Ni-peaks due to its low intensity. It is visible in other works [142], but its origin could not be found in literature.

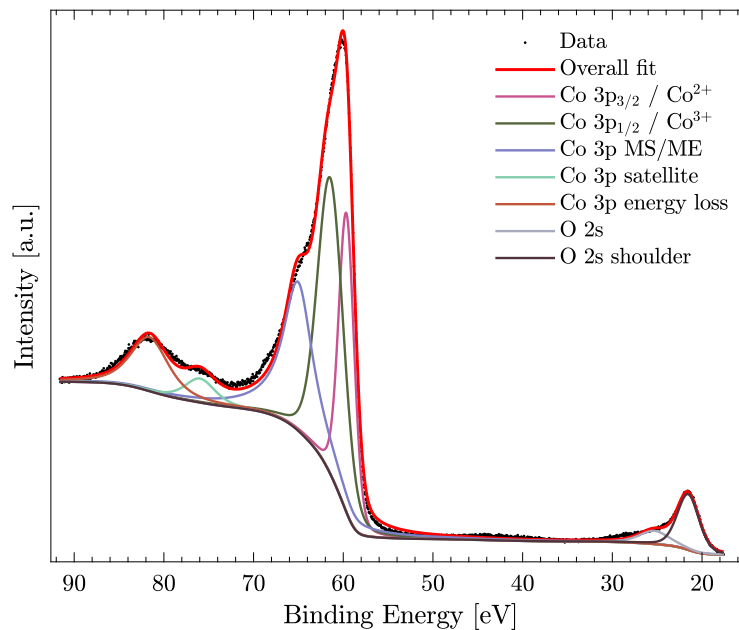


Figure B.1: Composite curve fit of a reference CoO sample. The peaks are labelled according to their approximate origin found in literature. A Shirley-background was included in the composite functions.

C | XAS magnetisation calculations

The magnetisations in figure 5.32 were calculated under the assumption that the total number of cations N_t in the films is given by

$$N_t = N \cdot (\text{NiCo}_2\text{O}_4) + N \cdot a \cdot (\text{Co}_b\text{Ni}_{1-b}\text{O}) \quad (\text{C.1})$$

with the spinel phase NiCo_2O_4 and the rock-salt phase $\text{Co}_b\text{Ni}_{1-b}\text{O}$. From the XAS curve fits, the cation amounts N_{Ni} , N_{Co} , $N_{\text{Co, RS}}$ and $N_{\text{Co, spinel}}$ are known. With them, parameters x and y can be defined as

$$y = \frac{N_{\text{Co, RS}}}{N_{\text{Co, spinel}}} = \frac{Nab}{2N} = \frac{ab}{2} \quad (\text{C.2})$$

and

$$x = \frac{N_{\text{Ni}}}{N_{\text{Co}}} = \frac{N + Na(1 - b)}{2N + Nab} = \frac{1 + a - ab}{2 + ab} = \frac{1 + a - 2y}{2 + 2y}, \quad (\text{C.3})$$

which leads to values for a and b :

$$a = x \cdot (2 + 2y) - 1 + 2y, \quad b = \frac{2y}{a}. \quad (\text{C.4})$$

The magnetisation of the film is given by

$$M = \frac{N \cdot 2\mu_B}{V_{\text{tot}}}, \quad (\text{C.5})$$

with

$$\frac{N}{V_{\text{tot}}} = \frac{1}{8}N \cdot V_{\text{UC, NCO}} + \frac{1}{4}Na \cdot V_{\text{UC, RS}} \quad (\text{C.6})$$

and where $V_{\text{UC, NCO}}$ and $V_{\text{UC, RS}}$ are given by literature values for the lattice parameters of nickel cobaltite and the rock-salts CoO and NiO , with the latter being

$$V_{\text{UC, RS}} \approx V_{\text{UC, CoO}} \cdot b + V_{\text{UC, NiO}} \cdot (1 - b). \quad (\text{C.7})$$

The relative amount of all cations that are present in the rock-salt phase is given as

$$\frac{N_{\text{RS}}}{N_{\text{tot}}} = \frac{Na(\text{Co}_b\text{Ni}_{1-b})}{Na(\text{Co}_b\text{Ni}_{1-b}) + N(\text{Ni} + 2\text{Co})} = \frac{a}{a + 3}, \quad (\text{C.8})$$

which results in the values in figure 5.17.

Literature

- [1] Yufan Shen et al. “Tuning of ferrimagnetism and perpendicular magnetic anisotropy in NiCo₂O₄ epitaxial films by the cation distribution”. In: *Physical Review B* 101 (2020). DOI: 10.1103/PhysRevB.101.094412.
- [2] Asaka Tsujie et al. “NiCo₂O₄ films fabricated by reactive molecular beam epitaxy and annealing in various oxygen atmospheres”. en. In: *Applied Physics Letters* 116.23 (June 2020), p. 232404. ISSN: 0003-6951, 1077-3118. DOI: 10.1063/5.0008677.
- [3] Punam Silwal et al. “Metal insulator transition with ferrimagnetic order in epitaxial thin films of spinel NiCo₂O₄”. en. In: *Applied Physics Letters* 100.3 (Jan. 2012), p. 032102. ISSN: 0003-6951, 1077-3118. DOI: 10.1063/1.3676439.
- [4] Yugandhar Bitla et al. “Origin of metallic behavior in NiCo₂O₄ ferrimagnet”. In: *Scientific Reports* 5 (2015). DOI: 10.1038/srep15201.
- [5] P. Cox and D. Pletcher. “Electrosynthesis at oxide coated electrodes Part 1 the kinetics of ethanol oxidation at spinel electrodes in aqueous base”. In: *Journal of Applied Electrochemistry* 20 (4 July 1990). DOI: 10.1007/BF01008862.
- [6] Ramesh J. Deokate et al. “Simple Synthesis of NiCo₂O₄ thin films using Spray Pyrolysis for electrochemical supercapacitor application: A Novel approach”. en. In: *Electrochimica Acta* 224 (Jan. 2017), pp. 378–385. ISSN: 00134686. DOI: 10.1016/j.electacta.2016.12.034.
- [7] Xuegang Chen et al. “Magnetotransport Anomaly in Room-Temperature Ferrimagnetic NiCo₂O₄ Thin Films”. en. In: *Advanced Materials* 31.4 (Jan. 2019), p. 1805260. ISSN: 09359648. DOI: 10.1002/adma.201805260.
- [8] J.F. Marco et al. “Characterization of the Nickel Cobaltite, NiCo₂O₄, Prepared by Several Methods: An XRD, XANES, EXAFS, and XPS Study”. en. In: *Journal of Solid State Chemistry* 153.1 (Aug. 2000), pp. 74–81. ISSN: 00224596. DOI: 10.1006/jssc.2000.8749.
- [9] Punam Silwal et al. “Thickness dependent structural, magnetic, and electronic properties of the epitaxial films of transparent conducting oxide NiCo₂O₄”. en. In: *Journal of Applied Physics* 114.10 (Sept. 2013), p. 103704. ISSN: 0021-8979, 1089-7550. DOI: 10.1063/1.4820930.
- [10] A.Y. Cho and J.R. Arthur. “Molecular beam epitaxy”. In: *Progress in Solid State Chemistry* 10 (1975), pp. 157–191. ISSN: 0079-6786. DOI: [https://doi.org/10.1016/0079-6786\(75\)90005-9](https://doi.org/10.1016/0079-6786(75)90005-9).

- [11] Charles Kittel. *Introduction to Solid State Physics*. John Wiley & Sons Inc., 2005.
- [12] K. Oura et al. *Surface Science an Introduction*. Springer-Verlag Berlin Heidelberg, 2003.
- [13] Martin Henzler. *Oberflächenphysik des Festkörpers*. B. G. Teubner Stuttgart, 1994.
- [14] N. W. Ashcroft and N. D. Mermin. *Solid State Physics*. Holt-Saunders, 1976.
- [15] Elizabeth A. Wood. “Vocabulary of Surface Crystallography”. In: *Journal of Applied Physics* 35 (1964).
- [16] Sadafumi Yoshida and Akira Kinbara. “Reactive molecular beam epitaxy”. In: *Critical Reviews in Solid State and Materials Sciences* 11.4 (1983), pp. 287–316. DOI: [10.1080/10408438308244621](https://doi.org/10.1080/10408438308244621).
- [17] H. Shinotsuka et al. “Calculations of electron inelastic mean free paths. Data for 41 elemental solids over the 50eV to 200keV range with the relativistic full Penn algorithm”. In: *Surface and interface Analysis* 47 (2015).
- [18] M. P. Seah and W. A. Dench. “Quantitative electron spectroscopy of surfaces: A standard data base for electron inelastic mean free paths in solids”. In: *Surface and Interface Analysis* 1.1 (1979), pp. 2–11. DOI: <https://doi.org/10.1002/sia.740010103>.
- [19] Jari Rodewald. “Advancement of growth and characteristics of ultrathin ferrite films”. PhD thesis. Nov. 2020.
- [20] Jens Als-Nielsen and Des McMorrow. *Elements of Modern X-Ray Physics, Second Edition*. John Wiley & Sons, Ltd, 2011.
- [21] Metin Tolan. *X-Ray Scattering from Soft-Matter Thin Films*. Springer-Verlag Berlin, Heidelberg, 1999. DOI: <https://doi.org/10.1007/BFb0112834>.
- [22] Jean Daillant and Alain Gibaud. *X-ray and neutron reflectivity : principles and applications*. Springer-Verlag Berlin, Heidelberg, 1999.
- [23] Abelès, Florin. “Recherches sur la propagation des ondes électromagnétiques sinusoïdales dans les milieux stratifiés - Application aux couches minces”. In: *Ann. Phys.* 12.5 (1950), pp. 596–640. DOI: [10.1051/anphys/195012050596](https://doi.org/10.1051/anphys/195012050596).
- [24] Guillaume Vignaud and Alain Gibaud. “REFLEX: a program for the analysis of specular X-ray and neutron reflectivity data”. In: *Journal of Applied Crystallography* 52.1 (Feb. 2019), pp. 201–213. DOI: [10.1107/S1600576718018186](https://doi.org/10.1107/S1600576718018186).
- [25] Névot, L. and Croce, P. “Caractérisation des surfaces par réflexion rasante de rayons X. Application à l’étude du polissage de quelques verres silicates”. In: *Rev. Phys. Appl. (Paris)* 15.3 (1980), pp. 761–779. DOI: [10.1051/rphysap:01980001503076100](https://doi.org/10.1051/rphysap:01980001503076100).
- [26] Frank de Groot and Aiko Kotani. *Core Level Spectroscopy of Solids*. CRC Press, 2008. DOI: <https://doi.org/10.1201/9781420008425>.
- [27] J.M.D. Coey. *Magnetism and Magnetic Materials*. Cambridge University Press, 2010. DOI: <https://doi.org/10.1017/CB09780511845000>.
- [28] Nicola A. Spaldin. *Magnetic Materials Fundamentals and Applications*. Cambridge University Press, 2010. DOI: <https://doi.org/10.1017/CB09780511781599>.

-
- [29] J. Stöhr and H.C. Siegmann. *Magnetism From Fundamentals to Nanoscale Dynamics*. Springer-Verlag Berlin, Heidelberg, 2006.
- [30] J. S. Philo and W. M. Fairbank. “Temperature dependence of the diamagnetism of water”. In: *The Journal of Chemical Physics* 72.8 (1980), pp. 4429–4433. DOI: 10.1063/1.439734.
- [31] Werner Heisenberg. “Zur Theorie des Ferromagnetismus”. In: *Zeitschrift für Physik* 49 (1928), pp. 619–636. DOI: <https://doi.org/10.1007/BF01328601>.
- [32] J. B. Goodenough. *Magnetism and the chemical bond*. Interscience Publishers, 1963.
- [33] C. P. Bean and J. D. Livingston. “Superparamagnetism”. In: *Journal of Applied Physics* 30.4 (1959), S120–S129. DOI: 10.1063/1.2185850.
- [34] Vibha H. Ojha and K. Mohan Kant. “Temperature dependent magnetic properties of superparamagnetic CoFe₂O₄ nanoparticles”. In: *Physica B: Condensed Matter* 567 (2019), pp. 87–94. ISSN: 0921-4526. DOI: <https://doi.org/10.1016/j.physb.2019.04.035>.
- [35] J. A. Mydosh. *Spin glasses: an experimental introduction*. Taylor & Francis London, Washington, DC, 1993.
- [36] P Dutta et al. “A comparative study of the magnetic properties of bulk and nanocrystalline Co₃O₄”. en. In: *Journal of Physics: Condensed Matter* 20.1 (Jan. 2008), p. 015218. ISSN: 0953-8984, 1361-648X. DOI: 10.1088/0953-8984/20/01/015218.
- [37] J. Clarke and A. I. Braginski. *The SQUID Handbook Vol. 1 Fundamentals and Technology of SQUIDS and SQUID Systems*. WILEY-VCH Verlag GmbH & Co. KgaA, Weinheim, 2004.
- [38] R. L. Fagaly. “Superconducting quantum interference device instruments and applications”. In: *Review of Scientific Instruments* 77.10 (2006), p. 101101. DOI: 10.1063/1.2354545.
- [39] H. Weinstock, ed. *SQUID Sensors: Fundamentals, Fabrication and Applications*. Springer-Science+Business Media, B.V., 1996.
- [40] Leon N. Cooper. “Bound Electron Pairs in a Degenerate Fermi Gas”. In: *Phys. Rev.* 104 (4 Nov. 1956), pp. 1189–1190. DOI: 10.1103/PhysRev.104.1189.
- [41] J. Bardeen, L. N. Cooper, and J. R. Schrieffer. “Theory of Superconductivity”. In: *Phys. Rev.* 108 (5 Dec. 1957), pp. 1175–1204. DOI: 10.1103/PhysRev.108.1175.
- [42] Y. Aharonov and D. Bohm. “Significance of Electromagnetic Potentials in the Quantum Theory”. In: *Phys. Rev.* 115 (3 Aug. 1959), pp. 485–491. DOI: 10.1103/PhysRev.115.485.
- [43] F. London. *Superfluids*. Vol. 1. Wiley, New York.
- [44] Bascom S. Deaver and William M. Fairbank. “Experimental Evidence for Quantized Flux in Superconducting Cylinders”. In: *Phys. Rev. Lett.* 7 (2 July 1961), pp. 43–46. DOI: 10.1103/PhysRevLett.7.43.
- [45] B.D. Josephson. “Possible new effects in superconductive tunnelling”. In: *Physics Letters* 1.7 (1962), pp. 251–253. ISSN: 0031-9163. DOI: [https://doi.org/10.1016/0031-9163\(62\)91369-0](https://doi.org/10.1016/0031-9163(62)91369-0).

- [46] Frank de Groot. “High-Resolution X-ray Emission and X-ray Absorption Spectroscopy”. In: *Chemical Reviews* 101.6 (2001), pp. 1779–1808. DOI: 10.1021/cr9900681.
- [47] D. Briggs and M. P. Seah. *Practical Surface Analysis by Auger and X-ray Photoelectron Spectroscopy*. John Wiley & Sons, Ltd., 1983.
- [48] Stefan Hüfner. *Photoelectron Spectroscopy Principles and Applications*. Springer-Verlag Berlin Heidelberg GmbH, 1995.
- [49] C.S. Fadley, C.R. Brundle, and A.D. Baker. *Basic Concepts of X-ray Photoelectron Spectroscopy*, in: *Electron Spectroscopy: Theory, Techniques and Applications*. Academic Press, 1978.
- [50] Michael Hoppe. “Magnetic, structural, and electronic properties of NiFe₂O₄ ultrathin films”. PhD thesis. 2016.
- [51] T Koopmans. “Über die Zuordnung von Wellenfunktionen und Eigenwerten zu den Einzelnen Elektronen Eines Atoms”. In: *Physica* 1.1 (1934), pp. 104–113. ISSN: 0031-8914. DOI: [https://doi.org/10.1016/S0031-8914\(34\)90011-2](https://doi.org/10.1016/S0031-8914(34)90011-2).
- [52] J. Cooper and R. N. Zare. “Angular Distribution of Photoelectrons”. In: *The Journal of Chemical Physics* 48.2 (1968), pp. 942–943. DOI: 10.1063/1.1668742.
- [53] M. B. Trzhaskovskaya, V. I. Nefedov, and V. G. Yarzhemsky. “Photoelectron Angular Distribution Parameters For Elements Z = 1 To Z = 54 In The Photoelectron Energy Range 100-5000 eV”. In: *Atomic Data and Nuclear Data Tables* 77 (2001).
- [54] J. W. Cooper. “Photoelectron-angular-distribution parameters for rare-gas subshells”. In: *Phys. Rev. A* 47 (3 Mar. 1993), pp. 1841–1851. DOI: 10.1103/PhysRevA.47.1841.
- [55] M. Repoux. “Comparison of Background Removal Methods for XPS”. In: *Surface and Interface Analysis* 18 (1992).
- [56] J. H. Scofield. “Hartree-Slater Subshell Photoionization Cross-Sections at 1254 and 1487 eV”. In: *Journal of Electron Spectroscopy and Related Phenomena* 8 (1976).
- [57] Cedric J. Powell and Paul E. Larson. “Quantitative surface analysis by X-ray photoelectron spectroscopy”. In: *Applications of Surface Science* 1 (1978), pp. 186–201.
- [58] D. A. Shirley. “High-Resolution X-Ray Photoemission Spectrum of the Valence Bands of Gold”. In: *Physical Review B* 5.12 (1972).
- [59] J.F. Moulder and J. Chastain. *Handbook of X-ray Photoelectron Spectroscopy: A Reference Book of Standard Spectra for Identification and Interpretation of XPS Data*. Physical Electronics Division, Perkin-Elmer Corporation, 1992. ISBN: 9780962702624.
- [60] Donald R. Baer et al. “XPS guide: Charge neutralization and binding energy referencing for insulating samples”. en. In: *Journal of Vacuum Science & Technology A* 38.3 (May 2020), p. 031204. ISSN: 0734-2101, 1520-8559. DOI: 10.1116/6.0000057. (Visited on 11/30/2020).

- [61] Evelyn Sokolowski, Carl Nordling, and Kai Siegbahn. “Chemical Shift Effect in Inner Electronic Levels of Cu Due to Oxidation”. In: *Phys. Rev.* 110 (3 May 1958), pp. 776–776. DOI: 10.1103/PhysRev.110.776.
- [62] Tobias Funk et al. “X-ray magnetic circular dichroism—a high energy probe of magnetic properties”. en. In: *Coordination Chemistry Reviews* (2005), p. 28.
- [63] M. Abbate et al. “Probing depth of soft x-ray absorption spectroscopy measured in total-electron-yield mode”. en. In: *Surface and Interface Analysis* 18.1 (Jan. 1992), pp. 65–69. ISSN: 0142-2421, 1096-9918. DOI: 10.1002/sia.740180111.
- [64] Goulon, J. et al. “On experimental attenuation factors of the amplitude of the EXAFS oscillations in absorption, reflectivity and luminescence measurements”. In: *J. Phys. France* 43.3 (1982), pp. 539–548. DOI: 10.1051/jphys:01982004303053900.
- [65] T. J. Regan et al. “Chemical effects at metal/oxide interfaces studied by x-ray-absorption spectroscopy”. In: *Phys. Rev. B* 64 (21 Nov. 2001), p. 214422. DOI: 10.1103/PhysRevB.64.214422.
- [66] Reiko Nakajima, J. Stöhr, and Y. U. Idzerda. “Electron-yield saturation effects in L -edge x-ray magnetic circular dichroism spectra of Fe, Co, and Ni”. en. In: *Physical Review B* 59.9 (Mar. 1999), pp. 6421–6429. ISSN: 0163-1829, 1095-3795. DOI: 10.1103/PhysRevB.59.6421.
- [67] K. Fauth. “How well does total electron yield measure x-ray absorption in nanoparticles?” en. In: *Applied Physics Letters* 85.15 (Oct. 2004), pp. 3271–3273. ISSN: 0003-6951, 1077-3118. DOI: 10.1063/1.1804600. (Visited on 02/14/2021).
- [68] F.M.F. de Groot et al. “Distortions of X-ray absorption spectra measured with fluorescence yield”. In: *Physica B: Condensed Matter* 208-209 (1995). Proceedings of the 8th International Conference on X-ray Absorption Fine Structure, pp. 84–86. ISSN: 0921-4526. DOI: [https://doi.org/10.1016/0921-4526\(94\)00638-C](https://doi.org/10.1016/0921-4526(94)00638-C).
- [69] E. Zschech et al. “A study of the self-absorption effect in the fluorescence yield of NiO at the oxygen K-edge”. In: *Solid State Communications* 82.1 (1992), pp. 1–5. ISSN: 0038-1098. DOI: [https://doi.org/10.1016/0038-1098\(92\)90395-P](https://doi.org/10.1016/0038-1098(92)90395-P).
- [70] Ryan M. Trevorah, Christopher T. Chantler, and Martin J. Schalken. “Solving self-absorption in fluorescence”. In: *IUCrJ* 6.4 (July 2019), pp. 586–602. DOI: 10.1107/S2052252519005128.
- [71] Bruce Ravel. “Quantitative EXAFS Analysis”. In: *X-Ray Absorption and X-Ray Emission Spectroscopy*. John Wiley & Sons, Ltd, 2016. Chap. 11, pp. 281–302. ISBN: 9781118844243. DOI: <https://doi.org/10.1002/9781118844243.ch11>.
- [72] J. Stöhr. “X-ray magnetic circular dichroism spectroscopy of transition metal thin films”. en. In: *Journal of Electron Spectroscopy and Related Phenomena* 75 (Dec. 1995), pp. 253–272. ISSN: 03682048. DOI: 10.1016/0368-2048(95)02537-5. URL: <https://linkinghub.elsevier.com/retrieve/pii/0368204895025375>.
- [73] U. Fano. “Spin Orientation of Photoelectrons Ejected by Circularly Polarized Light”. In: *Phys. Rev.* 178 (1 Feb. 1969), pp. 131–136. DOI: 10.1103/PhysRev.178.131.

- [74] Jannis Thien. “From Magnetite to Cobalt Ferrite Thin Films: New Perspectives for the Growth of Thin Ferrite Films for their Applications in Spintronics”. PhD thesis. Mar. 2022.
- [75] Paolo Carra et al. “X-ray circular dichroism and local magnetic fields”. en. In: *PHYSICAL REVIEW LETTERS* 70.5 (1993), p. 4.
- [76] B. T. Thole et al. “X-ray circular dichroism as a probe of orbital magnetization”. en. In: *Physical Review Letters* 68.12 (Mar. 1992), pp. 1943–1946. ISSN: 0031-9007. DOI: [10.1103/PhysRevLett.68.1943](https://doi.org/10.1103/PhysRevLett.68.1943). (Visited on 02/23/2021).
- [77] J. Stöhr. *NEXAFS Spectroscopy*. Ed. by G. Ertl, R. Gomer, and D. Mills. Springer-Verlag Berlin Heidelberg, 1992.
- [78] Frank de Groot. “Multiplet effects in X-ray spectroscopy”. In: *Coordination Chemistry Reviews* 249.1 (2005). Synchrotron Radiation in Inorganic and Bioinorganic Chemistry, pp. 31–63. ISSN: 0010-8545. DOI: <https://doi.org/10.1016/j.ccr.2004.03.018>.
- [79] Gerrit van der Laan. “Hitchhiker’s Guide to Multiplet Calculations”. In: *Magnetism: A Synchrotron Radiation Approach*. Ed. by Eric Beaurepaire et al. Berlin, Heidelberg: Springer Berlin Heidelberg, 2006, pp. 143–199. ISBN: 978-3-540-33242-8. DOI: [10.1007/3-540-33242-1_7](https://doi.org/10.1007/3-540-33242-1_7).
- [80] E. Wigner. “Einige Folgerungen aus der Schrödingerschen Theorie für die Termstrukturen”. In: *Zeitschrift für Physik* 43 (9 Sept. 1927). DOI: [10.1007/BF01397327](https://doi.org/10.1007/BF01397327).
- [81] Tobias Pohlmann. “Structural and magnetic properties of ultrathin Fe₃O₄ films: cation- and lattice-site-selective studies by synchrotron radiation-based techniques”. PhD thesis. Feb. 2021.
- [82] Piter S. Miedema and Frank M.F. de Groot. “The iron L edges: Fe 2p X-ray absorption and electron energy loss spectroscopy”. In: *Journal of Electron Spectroscopy and Related Phenomena* 187 (2013), pp. 32–48. ISSN: 0368-2048. DOI: <https://doi.org/10.1016/j.elspec.2013.03.005>.
- [83] K. Kuepper et al. “Electronic and magnetic structure of epitaxial Fe₃O₄(001)/NiO heterostructures grown on MgO(001) and Nb-doped SrTiO₃(001)”. In: *Phys. Rev. B* 94 (2 July 2016), p. 024401. DOI: [10.1103/PhysRevB.94.024401](https://doi.org/10.1103/PhysRevB.94.024401).
- [84] F.M.F. de Groot. “X-ray absorption and dichroism of transition metals and their compounds”. In: *Journal of Electron Spectroscopy and Related Phenomena* 67.4 (1994), pp. 529–622. ISSN: 0368-2048. DOI: [https://doi.org/10.1016/0368-2048\(93\)02041-J](https://doi.org/10.1016/0368-2048(93)02041-J).
- [85] A. I. Nesvizhskii et al. “Interpretation of x-ray magnetic circular dichroism and x-ray absorption near-edge structure in Ni”. en. In: *Physical Review B* 62.23 (Dec. 2000), pp. 15295–15298. ISSN: 0163-1829, 1095-3795. DOI: [10.1103/PhysRevB.62.15295](https://doi.org/10.1103/PhysRevB.62.15295).
- [86] M. Knoll and E. Ruska. “Das Elektronenmikroskop”. In: *Zeitschrift für Physik* 78 (5 May 1932). DOI: [10.1007/BF01342199](https://doi.org/10.1007/BF01342199).
- [87] D. B. Williams and C. B. Carter. *Transmission Electron Microscopy-A Textbook for Materials Science*. Springer New York, NY, 2009. DOI: <https://doi.org/10.1007/978-0-387-76501-3>.

- [88] S. Amelinckx et al., eds. *Electron Microscopy Principles and Fundamentals*. VCH Verlagsgesellschaft mbH, 1997.
- [89] Daisuke Shindo and Tetsuo Oikawa. “Energy Dispersive X-ray Spectroscopy”. In: *Analytical Electron Microscopy for Materials Science*. Tokyo: Springer Japan, 2002, pp. 81–102. ISBN: 978-4-431-66988-3. DOI: 10.1007/978-4-431-66988-3_4.
- [90] H. G. J. Moseley. “XCIII. The high-frequency spectra of the elements”. In: *Philosophical Magazine Series 1* 26 (1913), pp. 1024–1034.
- [91] H.G.J. Moseley M.A. “LXXX. The high-frequency spectra of the elements. Part II”. In: *The London, Edinburgh, and Dublin Philosophical Magazine and Journal of Science* 27.160 (1914), pp. 703–713. DOI: 10.1080/14786440408635141.
- [92] Marin Tadic et al. “Magnetic properties of NiO (nickel oxide) nanoparticles: Blocking temperature and Neel temperature”. In: *Journal of Alloys and Compounds* 647 (Oct. 2015), pp. 1061–1068. ISSN: 09258388. DOI: 10.1016/j.jallcom.2015.06.027.
- [93] P.A. Cox. *Transition Metal Oxides An Introduction to their Electronic Structure and Properties*. Clarendon Press, 1995.
- [94] W. Jauch et al. “Crystallographic symmetry and magnetic structure of CoO”. In: *Physical Review B* 64.5 (July 2001), p. 052102. ISSN: 0163-1829, 1095-3795. DOI: 10.1103/PhysRevB.64.052102.
- [95] W. L. Roth. “Magnetic Structures of MnO, FeO, CoO, and NiO”. In: *Phys. Rev.* 110 (6 June 1958), pp. 1333–1341. DOI: 10.1103/PhysRev.110.1333.
- [96] Anna Mandziak et al. “Tuning the Néel temperature in an antiferromagnet: the case of Ni_xCo_{1-x}O microstructures”. In: *Scientific Reports* 9.1 (Dec. 2019), p. 13584. ISSN: 2045-2322. DOI: 10.1038/s41598-019-49642-8.
- [97] H. Ohldag, G. van der Laan, and E. Arenholz. “Correlation of crystallographic and magnetic domains at Co/NiO(001) interfaces”. In: *Physical Review B* 79.5 (Feb. 2009), p. 052403. ISSN: 1098-0121, 1550-235X. DOI: 10.1103/PhysRevB.79.052403.
- [98] R. H. Kodama, Salah A. Makhlof, and A. E. Berkowitz. “Finite Size Effects in Antiferromagnetic NiO Nanoparticles”. In: *Phys. Rev. Lett.* 79 (7 Aug. 1997), pp. 1393–1396. DOI: 10.1103/PhysRevLett.79.1393.
- [99] I. P. Krug et al. “Impact of interface orientation on magnetic coupling in highly ordered systems: A case study of the low-indexed Fe₃O₄/NiO interfaces”. In: *Phys. Rev. B* 78 (6 Aug. 2008), p. 064427. DOI: 10.1103/PhysRevB.78.064427.
- [100] K. Tomiyasu, T. Inami, and N. Ikeda. “Magnetic structure of CoO studied by neutron and synchrotron x-ray diffraction”. In: *Physical Review B* 70.18 (Nov. 2004), p. 184411. ISSN: 1098-0121, 1550-235X. DOI: 10.1103/PhysRevB.70.184411.
- [101] S. C. Petitto and M. A. Langell. “Surface composition and structure of Co₃O₄(110) and the effect of impurity segregation”. In: *Journal of Vacuum Science & Technology A: Vacuum, Surfaces, and Films* 22.4 (July 2004), pp. 1690–1696. ISSN: 0734-2101, 1520-8559. DOI: 10.1116/1.1763899.

- [102] I. Ganesh. “A review on magnesium aluminate (MgAl_2O_4) spinel: synthesis, processing and applications”. In: *International Materials Reviews* 58.2 (Feb. 2013), pp. 63–112. ISSN: 0950-6608, 1743-2804. DOI: 10.1179/1743280412Y.0000000001.
- [103] M Akaogi et al. “High pressure transitions in the system MgAl_2O_4 – CaAl_2O_4 : a new hexagonal aluminous phase with implication for the lower mantle”. In: *Physics of the Earth and Planetary Interiors* 115.1 (1999), pp. 67–77. ISSN: 0031-9201. DOI: [https://doi.org/10.1016/S0031-9201\(99\)00076-X](https://doi.org/10.1016/S0031-9201(99)00076-X).
- [104] S.M. Hosseini. “Structural, electronic and optical properties of spinel MgAl_2O_4 oxide”. In: *physica status solidi (b)* 245 (2008). DOI: 10.1002/pssb.200844142.
- [105] H V Keer et al. “Electrical and magnetic properties of the MgMn_2O_4 – MgAl_2O_4 system”. In: *Journal of Physics D: Applied Physics* 7.15 (Oct. 1974), pp. 2058–2062. ISSN: 00223727. DOI: 10.1088/0022-3727/7/15/310.
- [106] M Uhl and B Siberchicot. “A first-principles study of exchange integrals in magnetite”. In: *Journal of Physics: Condensed Matter* 7.22 (May 1995), pp. 4227–4237. DOI: 10.1088/0953-8984/7/22/006.
- [107] José F. Marco et al. “Cation distribution and magnetic structure of the ferromagnetic spinel NiCo_2O_4 ”. In: *Journal of Materials Chemistry* 11.12 (Nov. 2001), pp. 3087–3093. ISSN: 09599428, 13645501. DOI: 10.1039/b103135j.
- [108] Daisuke Kan et al. “Spin and orbital magnetic moments in perpendicularly magnetized $\text{Ni}_{1-x}\text{Co}_{2+y}\text{O}_{4-z}$ epitaxial thin films: Effects of site-dependent cation valence states”. en. In: *Physical Review B* 101.22 (June 2020), p. 224434. ISSN: 2469-9950, 2469-9969. DOI: 10.1103/PhysRevB.101.224434.
- [109] Kaiqi Zhang et al. “Insight into metallic behavior in epitaxial half-metallic NiCo_2O_4 films”. en. In: *RSC Advances* 7.57 (2017), pp. 36026–36033. ISSN: 2046-2069. DOI: 10.1039/C7RA03136J.
- [110] Kevin Ruwisch. “Charakterisierung des Exchange Bias-Systems $\text{Fe}_3\text{O}_4/\text{CoO}$ mit SQUID und VSM”. MA thesis. Oct. 2018.
- [111] A. Piel. *Plasma Physics An Introduction to Laboratory, Space, and Fusion Plasmas*. Springer-Verlag Berlin Heidelberg, 2010. DOI: <https://doi.org/10.1007/978-3-642-10491-6>.
- [112] M. A. Lieberman. *Principles of Plasma Discharges and Materials Processing*. John Wiley & Sons, Inc., 2005. DOI: 10.1002/0471724254.
- [113] H. Postma. “Multiply charged heavy ions produced by energetic plasmas”. In: *Physics Letters A* 31.4 (1970), pp. 196–197. ISSN: 0375-9601. DOI: [https://doi.org/10.1016/0375-9601\(70\)90921-7](https://doi.org/10.1016/0375-9601(70)90921-7).
- [114] B.L. Henke, E.M. Gullikson, and J.C. Davis. “X-Ray Interactions: Photoabsorption, Scattering, Transmission, and Reflection at $E = 50$ – $30,000$ eV, $Z = 1$ – 92 ”. In: *Atomic Data and Nuclear Data Tables* 54.2 (1993), pp. 181–342. ISSN: 0092-640X. DOI: <https://doi.org/10.1006/adnd.1993.1013>.
- [115] M. Buchner et al. “Tutorial: Basic principles, limits of detection, and pitfalls of highly sensitive SQUID magnetometry for nanomagnetism and spintronics”. In: *Journal of Applied Physics* 124.16 (2018), p. 161101. DOI: 10.1063/1.5045299.
- [116] *S700X SQUID Magnetometer User Manual Version 0.9*. Cryogenic Ltd.

- [117] F. J. Richards. “A Flexible Growth Function for Empirical Use”. In: *Journal of Experimental Botany* 10.2 (June 1959), pp. 290–301. ISSN: 0022-0957. DOI: 10.1093/jxb/10.2.290.
- [118] Greig A. Paterson et al. “Measuring, Processing, and Analyzing Hysteresis Data”. In: *Geochemistry, Geophysics, Geosystems* 19.7 (2018). DOI: <https://doi.org/10.1029/2018GC007620>.
- [119] Mike Jackson and Peter Solheid. “On the quantitative analysis and evaluation of magnetic hysteresis data: HYSTERESIS LOOP EVALUATION AND ANALYSIS”. In: *Geochemistry, Geophysics, Geosystems* 11.4 (Apr. 2010). ISSN: 15252027. DOI: 10.1029/2009GC002932.
- [120] Eli Stavitski and Frank M.F. de Groot. “The CTM4XAS program for EELS and XAS spectral shape analysis of transition metal L edges”. In: *Micron* 41.7 (2010), pp. 687–694. ISSN: 0968-4328. DOI: <https://doi.org/10.1016/j.micron.2010.06.005>.
- [121] G. van der Laan. “Theory of simple spectra”. In: *Journal of Electron Spectroscopy and Related Phenomena* 86.1 (1997), pp. 41–47. ISSN: 0368-2048. DOI: [https://doi.org/10.1016/S0368-2048\(97\)00047-9](https://doi.org/10.1016/S0368-2048(97)00047-9).
- [122] Adolf Strecker et al. “Progress in the Preparation of Cross-Sectional TEM Specimens by Ion-Beam Thinning: Dedicated to Prof. Dr. Dr. h. c. Manfred Rühle on the Occasion of his 65th Birthday”. en. In: *Zeitschrift für Metallkunde* 94.3 (Mar. 2003), pp. 290–297. ISSN: 0044-3093. DOI: 10.3139/146.030290.
- [123] Thomas Haunold and Günther Rupprechter. “LiOx-modification of Ni and Co₃O₄ surfaces: An XPS, LEIS and LEED study”. en. In: *Surface Science* 713 (Nov. 2021), p. 121915. ISSN: 00396028. DOI: 10.1016/j.susc.2021.121915.
- [124] J.G. Kim et al. “Analysis of the NiCo₂O₄ spinel surface with Auger and X-ray photoelectron spectroscopy”. In: *Applied Surface Science* 165.1 (Sept. 2000), pp. 70–84. ISSN: 01694332. DOI: 10.1016/S0169-4332(00)00378-0.
- [125] K. S. Kim. “X-ray-photoelectron spectroscopic studies of the electronic structure of CoO”. In: *Physical Review B* 11.6 (Mar. 1975), pp. 2177–2185. ISSN: 0556-2805. DOI: 10.1103/PhysRevB.11.2177.
- [126] Adam Sarnecki et al. “XPS study of cobalt-ceria catalysts for ammonia synthesis – The reduction process”. en. In: *Vacuum* 155 (Sept. 2018), pp. 434–438. ISSN: 0042207X. DOI: 10.1016/j.vacuum.2018.06.034.
- [127] M. A. Langell et al. “Valence-band electronic structure of Co₃O₄ epitaxy on CoO(100)”. In: *Physical Review B* 59.7 (Feb. 1999), pp. 4791–4798. ISSN: 0163-1829, 1095-3795. DOI: 10.1103/PhysRevB.59.4791.
- [128] N. S. McIntyre and M. G. Cook. “X-ray photoelectron studies on some oxides and hydroxides of cobalt, nickel, and copper”. In: *Analytical Chemistry* 47.13 (Nov. 1975), pp. 2208–2213. ISSN: 0003-2700, 1520-6882. DOI: 10.1021/ac60363a034.
- [129] Mark C. Biesinger et al. “Resolving surface chemical states in XPS analysis of first row transition metals, oxides and hydroxides: Cr, Mn, Fe, Co and Ni”. In: *Applied Surface Science* 257.7 (Jan. 2011), pp. 2717–2730. ISSN: 01694332. DOI: 10.1016/j.apsusc.2010.10.051.

- [130] Jingfa Li et al. “High Electrochemical Performance of Monodisperse NiCo₂O₄ Mesoporous Microspheres as an Anode Material for Li-Ion Batteries”. en. In: *ACS Applied Materials & Interfaces* 5.3 (Feb. 2013), pp. 981–988. ISSN: 1944-8244, 1944-8252. DOI: 10.1021/am3026294.
- [131] K. Ruwisch. personal communication.
- [132] A. N. Mansour. “Characterization of NiO by XPS”. In: *Surface Science Spectra* 3.3 (July 1994), pp. 231–238. ISSN: 1055-5269, 1520-8575. DOI: 10.1116/1.1247751.
- [133] Andrew P. Grosvenor et al. “New interpretations of XPS spectra of nickel metal and oxides”. en. In: *Surface Science* 600.9 (May 2006), pp. 1771–1779. ISSN: 00396028. DOI: 10.1016/j.susc.2006.01.041.
- [134] J. Rodewald et al. “Real-time monitoring the growth of strained off-stoichiometric Ni_xFe_{3-x}O₄ ultrathin films on MgO(001)”. In: *Applied Physics Letters* 117.1 (2020), p. 011601. DOI: 10.1063/5.0013925.
- [135] Zeshu Zhang et al. “Surface density of synthetically tuned spinel oxides of Co³⁺ and Ni³⁺ with enhanced catalytic activity for methane oxidation”. en. In: *Chinese Journal of Catalysis* 39.7 (July 2018), pp. 1228–1239. ISSN: 18722067. DOI: 10.1016/S1872-2067(18)63055-4.
- [136] Getachew Solomon et al. “NiMoO₄@Co₃O₄ Core-Shell Nanorods: In Situ Catalyst Reconstruction toward High Efficiency Oxygen Evolution Reaction”. en. In: *Advanced Energy Materials* 11.32 (Aug. 2021), p. 2101324. ISSN: 1614-6832, 1614-6840. DOI: 10.1002/aenm.202101324.
- [137] Artur Born et al. “Separation of surface oxide from bulk Ni by selective Ni 3p photoelectron spectroscopy for chemical analysis in coincidence with Ni M-edge Auger electrons”. en. In: *Scientific Reports* 11.1 (Dec. 2021), p. 16596. ISSN: 2045-2322. DOI: 10.1038/s41598-021-96108-x.
- [138] Dang-Hoang Hop et al. “Oxygen nonstoichiometry and electrical properties of La_{2-x}Sr_xNiO_{4+δ} (0 ≤ x ≤ 0.5)”. en. In: *Journal of the Korean Ceramic Society* 57.4 (July 2020), pp. 416–422. ISSN: 1229-7801, 2234-0491. DOI: 10.1007/s43207-020-00049-6.
- [139] Jun-Hyuk Kim et al. “Enhanced Activity Promoted by CeO_x on a CoO_x Electrocatalyst for the Oxygen Evolution Reaction”. en. In: *ACS Catalysis* 8.5 (May 2018), pp. 4257–4265. ISSN: 2155-5435, 2155-5435. DOI: 10.1021/acscatal.8b00820.
- [140] Mohammad Nasir et al. “Exploring the role of Fe substitution on electronic, structural, and magnetic properties of La₂NiMnO₆ double perovskites”. In: *Applied Physics A* 127 (3 Feb. 2021). DOI: 10.1007/s00339-021-04361-8.
- [141] J. Rodewald et al. “Enhanced magnetization of ultrathin NiFe₂O₄ films on SrTiO₃(001) related to cation disorder and anomalous strain”. In: *Phys. Rev. Materials* 4 (6 June 2020), p. 064404. DOI: 10.1103/PhysRevMaterials.4.064404.
- [142] Jannis Thien. “Bildung und Charakterisierung von Cobaltferritschichten durch Interdiffusion von Cobaltoxid- und Magnetitschichten”. MA thesis. Sept. 2017.

- [143] Atsushi Fujimori, Fujio Minami, and Satoru Sugano. “Multielectron satellites and spin polarization in photoemission from Ni compounds”. In: *Physical Review B* 29.9 (May 1984), pp. 5225–5227. ISSN: 0163-1829. DOI: 10.1103/PhysRevB.29.5225.
- [144] T.J. Chuang, C.R. Brundle, and D.W. Rice. “Interpretation of the x-ray photoemission spectra of cobalt oxides and cobalt oxide surfaces”. In: *Surface Science* 59.2 (Oct. 1976), pp. 413–429. ISSN: 00396028. DOI: 10.1016/0039-6028(76)90026-1.
- [145] J. van Elp et al. “Electronic structure of CoO, Li-doped CoO, and LiCoO₂”. en. In: *Physical Review B* 44.12 (Sept. 1991), pp. 6090–6103. ISSN: 0163-1829, 1095-3795. DOI: 10.1103/PhysRevB.44.6090.
- [146] G. Bergenhoff and I.D. Brown. In: *Crystallographic Databases*. Ed. by F.H. Allen. Abbey Square, Chester: International Union of Crystallography, 1987.
- [147] H. Sharona et al. “Coexisting nanoscale inverse spinel and rock salt crystallographic phases in NiCo₂O₄ epitaxial thin films grown by pulsed laser deposition”. en. In: *Journal of Applied Physics* 122.22 (Dec. 2017), p. 225301. ISSN: 0021-8979, 1089-7550. DOI: 10.1063/1.4998776.
- [148] M Lenglet et al. “ELECTRONIC STRUCTURE OF NiCo₂O₄ BY XANES, EXAFS AND ⁶¹Ni MÖSSBAUER STUDIES”. en. In: *Solid State Communications* 74 (1990), p. 5.
- [149] R. M. Cornell and U. Schwertmann. *The Iron Oxides: Structure, Properties, Reactions, Occurrences and Uses, Second Edition*. Wiley-VCH Verlag GmbH & Co. KGaA, July 2003. DOI: 10.1002/3527602097.
- [150] T. Ambrose and C. L. Chien. “Finite-Size Effects and Uncompensated Magnetization in Thin Antiferromagnetic CoO Layers”. en. In: *Physical Review Letters* 76.10 (Mar. 1996), pp. 1743–1746. ISSN: 0031-9007, 1079-7114. DOI: 10.1103/PhysRevLett.76.1743.
- [151] Sanjay Singh et al. “Inverse magnetocaloric effect in Mn₂ NiGa and Mn_{1.75} Ni_{1.25} Ga magnetic shape memory alloys”. en. In: *Applied Physics Letters* 104.5 (Feb. 2014), p. 051905. ISSN: 0003-6951, 1077-3118. DOI: 10.1063/1.4863742.
- [152] Mengxiong Cao et al. “Point defects and magnetic properties of neutron irradiated MgO single crystal”. en. In: *AIP Advances* 7.5 (May 2017), p. 056413. ISSN: 2158-3226. DOI: 10.1063/1.4973942.
- [153] M. S. Seehra and P. Silinsky. “Non-Stoichiometry and Temperature-Dependent Magnetic Susceptibility of CoO”. In: *Solid State Communications* 31 (Mar. 1979).
- [154] J. Wollschläger. personal communication.
- [155] Yasuo Nakayama et al. “Temperature Dependent Epitaxial Growth of C60 Overlayers on Single Crystal Pentacene”. In: *Advanced Materials Interfaces* 5.12 (2018), p. 1800084. DOI: <https://doi.org/10.1002/admi.201800084>.
- [156] V. A. M. Brabers. In: *Handbook of Magnetic Materials*. Ed. by K. H. J. Buschow. Vol. 8. Elsevier Science B.V., 1995. Chap. 3.

- [157] T. D. Shen, R. B. Schwarz, and J. D. Thompson. “Paramagnetism, superparamagnetism, and spin-glass behavior in bulk amorphous Pd–Ni–Fe–P alloys”. In: *Journal of Applied Physics* 85.8 (1999), pp. 4110–4119. DOI: 10.1063/1.370319.
- [158] Issei Sugiyama et al. “Ferromagnetic dislocations in antiferromagnetic NiO”. en. In: *Nature Nanotechnology* 8.4 (Apr. 2013), pp. 266–270. ISSN: 1748-3387, 1748-3395. DOI: 10.1038/nnano.2013.45.
- [159] Chunsheng Zhou et al. “Magnetic and thermodynamic properties of α , β , γ and δ -MnO₂”. en. In: *New Journal of Chemistry* 42.11 (2018), pp. 8400–8407. ISSN: 1144-0546, 1369-9261. DOI: 10.1039/C8NJ00896E.

Erklärung zur selbstständigen Abfassung der Masterarbeit

Name: Florian Donder
Geburtsdatum: 05.10.1995
Matrikelnummer: 965733
Titel der Masterarbeit: Electronic and Magnetic Structure of Epitaxial Nickel Cobaltite Ultrathin Films on $\text{MgAl}_2\text{O}_4(001)$

Ich versichere, dass ich die eingereichte Masterarbeit selbstständig und ohne unerlaubte Hilfe verfasst habe. Anderer als der von mir angegebenen Hilfsmittel und Schriften habe ich mich nicht bedient. Alle wörtlich oder sinngemäß den Schriften anderer Autoren entnommenen Stellen habe ich kenntlich gemacht.

Ort, Datum

Unterschrift